SEDIMENT LADEN ICE DETECTION USING BROADBAND ACOUSTIC BACKSCATTERING MEASUREMENTS FROM CALIBRATION TARGETS IN ICE

by

Nicholas Dourado

Submitted in partial fulfillment of the requirements
for the degree of Master of Science

at

Dalhousie University
Halifax, Nova Scotia
March 2015

How narrow is the vision that exalts the busyness of the ant above the singing of the grasshopper.

-K.G.

TABLE OF CONTENTS

LIST OF TABLES

LIST OF FIGURES

ABSTRACT

In the winter, the tidal flats in the Bay of Fundy are littered with large muddy icebergs that are dense enough to sink. This sediment-laden ice to poses a risk to tidal power infrastructure. I attempted to identify echoes from the interior of the ice using a broadband echosounder system. Acoustic backscattering measurements from calibration targets encased in bubble-free ice were used to potentially locate strong targets in ice. Scattering from a planar surface of bubble-free ice overwhelmed echoes from encased targets, hence I was unable to conclusively detect solid and hollow spheres in ice. The total echoes from ice with inclusions could not be differentiated from ice without inclusions. My results imply that echoes from sediment laden ice blocks cannot be interpreted by modelling separate scattering mechanisms within the ice, and that future modelling should focus on echoes from sediment-laden ice surfaces.

List of Abbreviations and Symbols Used

Symbol	Description	Units
λ	First Lamé Parameter	Pa
μ	Second Lamé Parameter	Pa
$\mathbf{u}$	Particle Displacement	m
ρ	Density	kg/m^3
c_l	Compressional Soundspeed	m/s
c_s	Shear Soundspeed	m/s
ω	Frequency	Hz
t	Time	s
k_{l1}	Compressional Wavenumber in Media	m^{-1}
k_{l2}	Compressional Wavenumber in Target	m^{-1}
k_{s1}	Shear Wavenumber in Media	m^{-1}
k_{s2}	Shear Wavenumber in Target	m^{-1}
ϕ	Scalar Scattering Potential	m^2
ϕ_0	Incident Longitudinal Wave Magnitude	m^2
$\phi^{(i)}$	Incident Longitudinal Wave	m^2
$\phi_1^{(s)}$	Scattered Longitudinal Wave	m^2
$\phi_2^{(r)}$	Refracted Longitudinal Wave	m^2
$\vec{\psi}$	Vector Scattering Potential	m^2
$\vec{\psi}_0$	Incident Shear Wave Magnitude	m^2
$\vec{\psi}^{(i)}$	Incident Shear Wave	m^2
$\vec{\psi}_1^{(s)}$	Scattered Shear Wave	m^2
$\vec{\psi}_2^{(r)}$	Refracted Shear Wave	m^2

Symbol	Description	Units
A_n	Amplitude of Scattered Compressional Wave	-
$\mathbf{B_n}$	Amplitude of Scattered Shear Wave	-
C_n	Amplitude of Refracted Compressional Wave	-
$\mathbf{D_n}$	Amplitude of Refracted Shear Wave	-
r	Range	m
r_{I1}	Range to Ice Surface	m
r_{I2}	Range to Bottom Ice Surface	m
θ	Angle	rad
φ	Azimuth	rad
j_n	Spherical Bessel Function	-
h_n	Spherical Hankel Function	-
P_n	Legendre Polynomial	-
u_r	Radial Particle Displacement	m
u_θ	Tangential Particle Displacement	m
τ_{rr}	Normal Stress	Pa
$\tau_{r\theta}$	Tangential Stress	Pa
a	Sphere Radius	m
a_1	Inner Shell Radius	m
a_2	Outer Shell Radius	m
Fs	Solid Sphere in a Fluid Medium	-
Ss	Solid Sphere in a Solid Medium	-
Sf	Fluid Sphere in a Solid Medium	-
Ff	Fluid Sphere in a Fluid Medium	-
sf	Fluid Sphere in a Solid Shell	-
d_n	Scattering Coefficients from *Gaunard and Uberall* (1983)	-
b_n	Scattering Coefficients from *Flax and Uberall* (1980)	-

Symbol	Description	Units
c_n	Scattering Coefficients from *Gaunard and Uberall* (1978)	-
R_{12}	Reflection Coefficient	-
T_{12}	Transmission Coefficient	-
Z_2	Acoustic Impedance of Target	N s /m^3
Z_1	Acoustic Impedance of Medium	N s /m^3
ϑ_i	Incidence Angle	rad
ϑ_t	Transmission Angle	rad
ϑ_c	Critical Angle	rad
f_∞	Scattering Form Function	m
σ_{bs}	Backscattering Cross Section	m^2
TS_o	Target Strength of Sphere in Water	dB re 1m^2
TS_i	Target Strength of Sphere in Ice	dB re 1m^2
TS_I	Target Strength of Ice Block	dB re 1m^2
V_{sam}	Sample Volume	m^3
θ_b	Half-Angle Beam Width	rad
A_b	Beam Area	m^2
D	Transducer Diameter	m
R_b	Range to Beam Footprint	m
r_b	Beam Radius	m
r_{b1}	Beam Radius at the Top of the Sample Volume	m
r_{b1}	Beam Radius at the Bottom of the Sample Volume	m
δR	Height of the Sample Volume	m
V_b	Beam Sample Volume	m^3
R_{ff}	Transducer Far Field	m
c	Soundspeed in Aquatron Tank	m/s
WC	Tungsten Carbide	-

Symbol	Description	Units
PP	Polypropylene	-
N_{ping}	Number of Pings	-
A_i	Area of Ensonified Ice Surface	m^2
κ_c	Proportionality Constant	-
S_{bs}	Backscatter Time Series	-
S_{tr}	Transmit Pulse Time Series	-
$\hat{S}_{bs}$	Backscatter Spectrum	-
TS_{obs}	Observed Target Strength	dB re $1m^2$
TS_{mod}	Modelled Target Strength	dB re $1m^2$
t_{pulse}	Pulse Length	s
t_{cp}	Compressed Pulse Length	s
β	Echosounder Bandwidth	Hz
CP	Compressed Pulse	-
$\tilde{R}$	Range to Peak in Compressed Pulse	m
N_{fft}	Number of Points in the FFT window	-
N	Sample Number	-
$N_{\tilde{R}}$	Sample Number corresponding to CP Peak	-

ACKNOWLEDGEMENTS

This document was not produced in isolation, and frankly, this page cannot do justice to my gratitude.

First and foremost, I am indebted to my supervisor Tetjana Ross for the opportunity and commitment; whose patience and acceptance in dealing with my eccentricities allowed this work to be both ambitious and realistic. Also note, dear reader, that her talents as a physicist and editor kept this manuscript reasonable and legible. To my committee, Alex Hay and Paul Hill for the personal and professional guidance. Their steadfast accuracy inspired me almost as much as their effortless humour. Thanks to Sean Pecknold for taking part in my defence.

Thanks to Richard Chiassion (http://icecreation.ca/) and Brett Fletcher for producing and transporting my ice block sculptures. Very special thanks to Richard Cheel and Kirk Herman for the hands-on assistance designing and facilitating my experiments, I never could have got those ice blocks in the water without you. Thanks to Jim Eddington and John Batt for access to the Aquatron. Much thanks to Paul Hill, CarolAnne Black and Laura DeGelleke for the trips to the country to play with muddy ice. Richard Cheel, Mark Merrimen and Walter Judge were invaluable resources in the lab, field and hallway. This manuscript is dedicated to my officemates Jenna Hare and Dylan DeGrace for inspiring me to make something pretty worth remembering.

To the Faculty, Staff and Students in the Physical Oceanography Department, I am honoured that your unrelenting brilliance rubbed off on me. Thank You for brining me into this tradition. Thanks for the buoyancy, momentum and stability through turbulent times. I would fill a book with names and stories. The people make this place.

Most significantly, to my Mom, Dad and Brother for believing that I would amount to more than a garbage man, especially when I did not. The ambition and intelligence is theirs. Infinite blessings to my Halifax family; Jeremy, Jess, Kira, Dave and Rachel for the bitching and beautiful life.

My funding was provided by Nova Scotia Power Incorporated and the Nova Scotia Department of Energy through the Pengrowth Energy Innovation Grant. Thanks for the opportunity. Whatever brought you here, dear reader, Thanks for picking up this document.

CHAPTER 1

INTRODUCTION

Figure 1.1: A large ($>$ 6 meters diameter) composite sediment-laden ice block rests on the tidal flats near Debert, NS on February 19, 2013. Dense ice remains submerged throughout the tidal cycle, evidenced by tracks along the seafloor.

1.1 Motivation

The tides in the Bay of Fundy remain among the most coveted untapped energy sources on Earth. They may provide up to 2000 MW of electricity (*Karsten et al.*, 2012) without requiring fossil fuel combustion. In addition, the tides produce regular and relatively predictable currents that are reliable and practical for long-term energy extraction. There is significant economic incentive for communities in Atlantic Canada to develop tidal power; both as an opportunity to generate affordable, renewable energy and to supply technology and expertise to the offshore renewable energy industry. However, the potential

Figure 1.2: Sediment-laden ice cliffs, that are approximately 5 meters tall, form along the Kennetcook River on February 23, 2012. As these cliffs collapse, large sediment-laden ice blocks are introduced to the tidal river.

rewards are tempered by the challenge of maintaining underwater infrastructure in the Bay of Fundy's powerful tidal currents. In particular, submerged debris transported by the tidal currents may collide with tidal turbines. The added cost associated with subsurface collisions threatens the viability of tidal energy projects. *Sanders and Baddour* (2008) identify collisions with water-logged woody debris and with sediment-laden ice blocks (see Figure 1.1) as realistic threats to underwater turbines.

1.1.1 Sediment-Laden Ice

Black (2013) described the processes that cause large ice cliffs to form on the banks of tidal rivers near the Bay of Fundy (Figure 1.2). Mud from the river banks is frozen in the ice (*Black*, 2013). As the ice walls collapse, large sediment-laden ice blocks (Figure 1.1) are released and transported through the watershed to ultimately reach tidal estuaries in the Bay of Fundy (*Black*, 2013), shown in Figure 1.3. Sediment-laden ice is abundant in the Bay of Fundy in the winter (*Hind*, 1875; *Desplanque and Mossman*, 1998; *Sanders and Baddour*, 2006; *Black*, 2013). As these blocks melt, they can preferentially lose water and retain sediment, therein increasing the bulk density of the ice (*Black*, 2013). These blocks may contain enough sediment to become negatively buoyant (*Sanders and Baddour*, 2006;

Figure 1.3: Sediment-laden ice blocks are common on tidal flats in the winter, pictured February 19, 2013. While only a small proportion of the blocks sink, their abundance suggests that sunken ice moves in the water column.

Black, 2013).

Sanderson and Redden (2015) remark that there is no evidence of sediment-laden ice striking a tidal turbine, although no efforts to observe sediment-laden ice in the water column have been attempted. Samples from sediment-laden ice blocks in Minas Passage show that the majority of blocks are buoyant and unlikely to collide with an underwater turbine (*Sanderson and Redden*, 2015); however, the lack of evidence does not guarantee that a collision will not occur. Although only $\sim$10% of observed sediment-laden ice blocks are denser than water (*Black*, 2013), they are abundant in the late-winter (Figure 1.3), implying that a number of blocks will sink. In the case that submerged ice remains mobile, there is a risk of collision with a tidal turbine (*Sanders and Baddour*, 2006).

Sanders (2011) believes there is enough circumstantial evidence that sediment-laden ice can be transported by the tidal currents. In addition, the number of blocks that move through an area is proportional to the current speed and the damage caused by an impact scales as the cube of the current speed. Therefore, the potential for power production is proportional to the potential damage of by a collision (*Sanderson et al.*, 2012). Since sediment-laden ice floating at the sea surface is not of interest, *Sanders and Baddour* (2008), *Sanderson and Redden* (2015) and *Trowse* (2013) recommend monitoring sediment-laden underwater using an echosounder to range and identify submerged hazards.

1.1.2 Acoustic Detection of Submerged Ice

Evidence of sediment-laden ice blocks in the water column is sparse and the depth of sediment-laden ice floes is not documented (*Sanderson and Redden*, 2015). In addition, estimates of sediment-laden ice strength, a metric required to quantify the risk posed by submerged ice, are not available. *Sanderson et al.* (2012) provide porosity measurements from sediment-laden ice blocks in Minas Passage that they suggest may be used as a proxy for block strength.

An echosounder system, which transmits and receives acoustic pulses, can be used to locate and possibly identify submerged ice blocks (*Sanders and Baddour*, 2008); where the distance of the scattering source is proportional to time it takes for the transmitted energy to return to the echosounder. Echosounders have been used to identify ice at sea since the sinking of the *RMS Titanic* (*Frost*, 2001), and have subsequently been used to study the existence of elastic waves in ice (*Ewing et al.*, 1934; *Press and Ewing*, 1951; *Rothlisberger*, 1972; *Williams and Robinson*, 1981; *Chamuel*, 1990), the acoustic reflectivity of the Arctic ice canopy (*Press et al.*, 1950; *Langleben*, 1970; *Winebrenner*, 1991), reverberation and noise underneath sea ice (*Brown and Brown*, 1966; *Mellen and Marsh*, 1965; *Milne*, 1972), ice keels and underwater protuberances (*Stanton et al.*, 1986; *Fricke*, 1993; *Mourad and Williams*, 1993; *Abeele et al.*, 1996), the elastic and mechanical properties of ice (*Anderson*, 1963; *Williams and Francois*, 1992; *Stein et al.*, 1998), absorption and attenuation of sound in ice (*Wen et al.*, 1991) and the propagation of acoustic signals in the Arctic ocean (*Etter*, 2013).

Less focus has been placed on modelling echoes from inside ice, since echoes from sea ice surfaces are likely stronger than echoes from inclusions (*Winebrenner*, 1991). The abundance of encased sediment and air bubbles imply that this may not be the case for sediment-laden ice in the Bay of Fundy. For example, strong reflections from gaseous inclusions in fish and zooplankton are used to identify and enumerate organisms underwater (*Stanton et al.*, 2000; *Lavery et al.*, 2007; *Simmonds and MacLennan*, 2005; *Ross et al.*, 2013). The frequency dependence of echoes are interpreted using acoustic scattering models that infer the properties of the scattering source. *Love* (1978) and *Foote* (1980) shows that the echoes from fish depend on the size and shape of the swim bladder, as a result of the strong reflection from air in water. In addition, bubble clouds strongly scatter and attenuate acoustic signals in the ocean (*Farmer et al.*, 2001), suggesting that air

cavities in ice could contribute significantly to the scattering from submerged ice blocks.

In the case of sediment-laden ice, scattering is expected occur at the ice-water interface and from discontinuities or inclusions within the ice, assumed to be sediment or air bubbles, shown in Figure 1.4. The amplitude of the wave scattered from each interface depends on the change in elastic properties about an interface and the size and shape of the scatterer with respect to the acoustic frequency. Since air bubbles are much less dense and more compressible than ice, strong echoes may be produced from air encased in ice. Remote estimates of sediment and air content may lead to estimates of block strength. Furthermore, acoustic detection of ice inclusions is valuable in the Arctic, where the internal structure of ice is important in understanding sediment transport (*Nurnberg et al.*, 1994; *Eicken et al.*, 2005), structural integrity (*Winebrenner*, 1991), melt rate (*Trowse*, 2013) and the feasibility of resource exploitation (*Maksimov*, 2011; *Bassett et al.*, 2015).

There are currently no models that estimate the backscattering cross section from sediment-laden ice, or from sediment and air inclusions in underwater ice. If an acoustic pulse can penetrate the surface of a sediment-laden ice block, and the block contains enough sediment or air (see Figure 1.4), scattering from inclusions within the ice could be stronger than scattering from the ice surfaces. Scattering observed from inclusions in ice may enable remote estimation of the sediment content or strength of a sediment-laden ice block.

1.2 Objectives

The objective of this thesis is to determine if scattering models from solid and hollow inclusions can be used to identify spherical targets in ice. I will:

(I) Select models for different scattering mechanisms of sediment-laden ice, focusing on sediment and air inclusions.

(II) Measure acoustic backscattering from solid and air-filled spheres in water and in ice.

(III) Consider the feasibility of remotely detecting sediment and air content from scattering measurements.

My hypothesis is that echoes from solid and hollow spheres encased in ice can be located and identified by comparing frequency dependent scattering strength with acoustic

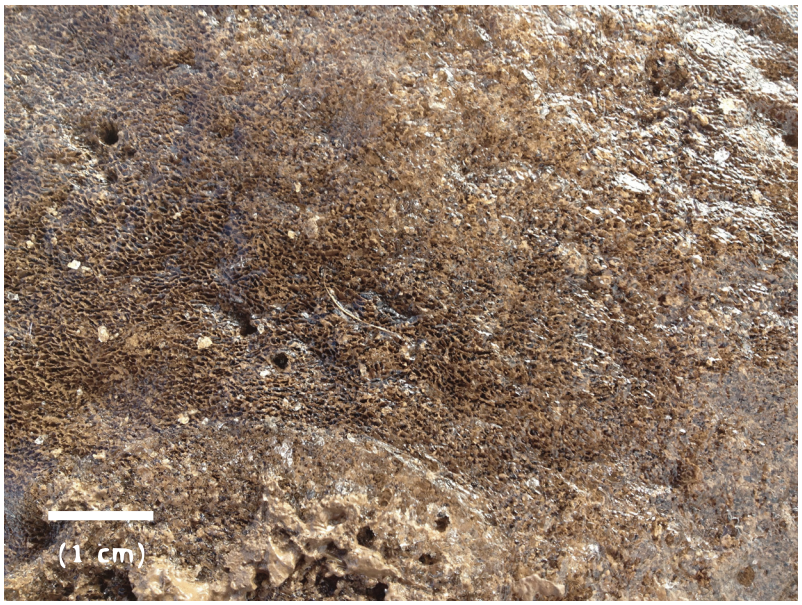

Figure 1.4: A photograph of the surface of a sediment-laden ice block, taken on February 23, 2012, shows that they are primarily comprised of ice, sediment and air. Small scale surface roughness is also apparent.

backscattering models. Backscattering was observed from an assortment of solid and hollow spheres in water and ice. Solid and hollow spheres represent the two different types of scattering expected to occur within sediment-laden ice blocks; solid spheres represent idealized sediment particles and hollow spheres represent air bubbles encased in ice. The validation of scattering models will allow for parameterization for sediment and air inclusions in ice, informed by sediment and air content estimates, the models can provide a framework for detecting the contents of sediment-laden ice underwater.

I describe acoustic scattering models for solid and fluid spheres in solid and fluid media in Chapter 2. I compare broadband acoustic pulses scattered from target spheres in water and encased in bubble-free ice blocks, following the procedure outlined in Chapter 3. The frequency dependent scattering strength is used to evaluate the acoustic scattering models. Observations from submerged target spheres, ice surfaces and target spheres encased in ice are provided in Chapter 4. Modelling sediment-laden ice is presented in Chapter 5.

CHAPTER 2

SCATTERING MODELS

Mathematical models are used to interpret acoustic echoes from scatterers embedded in an elastic or fluid medium. An acoustic wave travels in a straight line until it encounters a change in the medium, where a fraction of the wave energy changes direction and radiates as scattered or refracted waves (*Morse and Ingard*, 1968). The strength of the scattered wave is not constant in all directions and depends on the frequency of the transmitted wave; as well as the size, shape and change in elasticity of the medium (*Morse and Ingard*, 1968). The properties of a medium change abruptly at encased targets, producing a distinct scattered wave (*Medwin and Clay*, 1998). Consequently, if the properties of the transmitted wave are known, the properties of the target can be inferred from the scattered wave (*Medwin and Clay*, 1998).

Acoustic waves, which are a subclass of elastic waves, arise as particle motion is restored by a medium's elastic forces, causing a deformation to propagate (*Graff*, 1975). This gives rise to two types of elastic wave; compressional waves that travel parallel to particle motion and shear waves that travel perpendicular to particle motion (*Graff*, 1975). These waves travel at different rates and are modelled as distinct waves (*Graff*, 1975). Mathematical models compute the particle motion and the stresses that result from wave energy using a combination of harmonic functions to represent incident, scattered and refracted waves. By conserving energy at the target interface, the strength of the waves are computed (*Graff*, 1975). This chapter outlines the formalism of this approach for scattering from solid and fluid spheres encased in solid and fluid media.

2.1 Governing Equations

Acoustic and elastic waves must satisfy the equation of motion (Equation 2.1) for a homogeneous, isotropic, non-dispersive elastic medium (*Morse*, 1948).

$$(\lambda + 2\mu)\nabla(\nabla \cdot \mathbf{u}) - \mu\nabla \times (\nabla \times \mathbf{u}) = \frac{\rho\partial^2\mathbf{u}}{\partial^2 t} \tag{2.1}$$

where $\mathbf{u}$ is the instantaneous particle displacement vector, ρ is the density, λ is the first Lamé parameter and μ is the shear modulus of the medium that contains the wave.

The divergence of Equation 2.1 produces a scalar wave equation, while the curl of Equation 2.1 produces a vector wave equation,

$$\nabla^2(\nabla \cdot \mathbf{u}) = \frac{\rho}{\lambda + 2\mu}\frac{\partial^2(\nabla \cdot \mathbf{u})}{\partial^2 t} \tag{2.2}$$

and

$$\nabla^2(\nabla \times \mathbf{u}) = \frac{\rho}{\mu}\frac{\partial^2(\nabla \times \mathbf{u})}{\partial^2 t} \tag{2.3}$$

where $\nabla \cdot \mathbf{u}$ represents localized pressure and $\nabla \times \mathbf{u}$ represents local shear. Consequently, Equation 2.2 represents compressional (longitudinal) waves and Equation 2.3 represents shear (transverse) waves. The speeds of the longitudinal, c_l, and transverse, c_s, waves are thus

$$c_l = \sqrt{\frac{\lambda + 2\mu}{\rho}} \quad \text{and} \quad c_s = \sqrt{\frac{\mu}{\rho}} \tag{2.4}$$

with corresponding wavenumbers,

$$k_l = \frac{\omega}{c_l} \quad \text{and} \quad k_s = \frac{\omega}{c_s} \tag{2.5}$$

where ω is the angular frequency ($\omega = 2\pi f$, where f is the frequency).

According to Helmholtz theorem, the particle displacement vector field that results from propagating waves can be decomposed into a scalar potential, ϕ, and vector potential, $\vec{\psi}$ (*Mow and Pao*, 1971).

$$\mathbf{u} = \nabla\phi + \nabla \times \vec{\psi}. \tag{2.6}$$

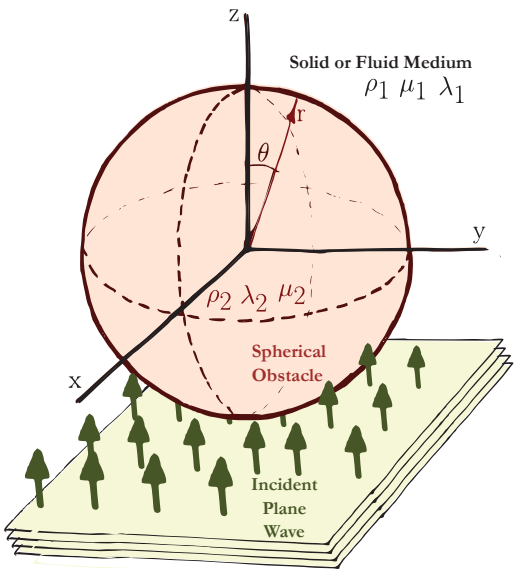

Figure 2.1: The spherical coordinate system (Equation 2.8) from *Mow and Pao* (1971) is used in the following scattering models.

The potentials will satisfy the following equations

$$\nabla^2\phi = \frac{1}{c_l^2}\frac{\partial^2\phi}{\partial^2 t} \tag{2.7a}$$

$$\nabla^2\vec{\psi} = \frac{1}{c_s^2}\frac{\partial^2\vec{\psi}}{\partial^2 t} \tag{2.7b}$$

where, $\nabla \cdot \mathbf{u} = \nabla \cdot \nabla\phi$ satisfies Equation 2.2 and $\nabla \times \mathbf{u} = \nabla \times \nabla \times \vec{\psi}$ satisfies Equation 2.3 (*Mow and Pao*, 1971).

Solutions to these potentials can then be expressed as a combination of spherical harmonic functions (*Mow and Pao*, 1971).

2.2 Modelling Scattering from Spheres

For the case of scattering from spherical obstacles, a spherical coordinate system will be adopted (see Figure 2.1) with the target sphere centred at the origin. The transformation from Cartesian to spherical coordinates is given by

$$r = \sqrt{x^2 + y^2 + z^2}, \quad \theta = \tan^{-1}(y/x), \quad \varphi = \cos^{-1}(z/r). \tag{2.8}$$

where r is the radial distance and θ represents the polar angle and φ is the azimuthal angle. Azimuthal dependence is ignored due to the symmetry of the problem.

A transmitted acoustic pulse is expressed as a plane harmonic wave that is a solution to Equations 2.7a and 2.7b (*Abramowitz and Stegun*, 1964).

$$\phi^{(i)} = \phi_0 e^{-i(k_{l1} r \cos\theta\ \omega t)}, \tag{2.9a}$$

and

$$\vec{\psi}^{(i)} = \vec{\psi}_0 e^{-i(k_{s1} r \cos\theta\ \omega t)} \tag{2.9b}$$

where $\phi^{(i)}$ represents the transmitted compressional wave and $\psi^{(i)}$ represents a transmitted shear wave, k_{l1} and k_{s1} are the wave numbers for compressional and shear waves in the medium that contains the transmitted wave, respectively; and ϕ_0 and ψ_0 represent the amplitude of the incident compressional and shear waves. Our model assumes that the incident wave is purely compressional, so $\psi_0 = 0$. Equation 2.9a is then expanded as a sum of spherical harmonics (see Appendix A) (*Boas*, 1966).

$$\phi^{(i)} = \phi_0 e^{-i\omega t} \sum_{n=0}^{\infty} i^n (2n+1) j_n(k_{l1} r) P_n(\cos\theta) \tag{2.10}$$

The expressions for scattered and refracted waves, in terms of spherical harmonic functions (see Appendix A and *Mow and Pao* (1971)) are

$$\phi_1^{(s)} = \phi_0 e^{-i\omega t} \sum_{n=0}^{\infty} i^n (2n+1)\ A_n\ h_n(k_{l1} r)\ P_n(\cos\theta) \tag{2.11}$$

$$\vec{\psi}_1^{(s)} = \phi_0 e^{-i\omega t} \sum_{n=0}^{\infty} i^n (2n+1)\ \mathbf{B_n}\ h_n(k_{s1} r)\ P_n(\cos\theta) \tag{2.12}$$

$$\phi_2^{(r)} = \phi_0 e^{-i\omega t} \sum_{n=0}^{\infty} i^n (2n+1)\ C_n\ j_n(k_{l2} r)\ P_n(\cos\theta) \tag{2.13}$$

$$\vec{\psi}_2^{(r)} = \phi_0 e^{-i\omega t} \sum_{n=0}^{\infty} i^n (2n+1)\ \mathbf{D_n}\ j_n(k_{s2} r)\ P_n(\cos\theta) \tag{2.14}$$

The potentials corresponding to the scattered longitudinal wave, $\phi_1^{(s)}$, and scattered transverse wave, $\vec{\psi}_2^{(r)}$, are determined by the A_n and $\mathbf{B_n}$ amplitude coefficients, respectively. The potentials corresponding to the refracted longitudinal wave, $\phi_1^{(s)}$, and refracted

transverse wave, $\vec{\psi_2^{(r)}}$, are determined by the C_n and $\mathbf{D_n}$ amplitude coefficients, respectively. Note that, even though there is no transmitted shear wave, shearing occurs as the wave changes speed in the target. The subscript of the potentials denote the medium that contains the wave and specifies the elastic properties that constrain elastic motion, where 1 refers to the medium that contains the transmitted and scattered wave, and 2 refers to the sphere.

The spherical Bessel functions of the first kind, j_n, (see Figure A.1) and spherical Hankel functions of the first kind, h_n, (see Figure A.2) of order n, are harmonic functions that are common solutions for problems with spherical or cylindrical symmetry. The Legendre polynomials, $P_n(\cos\theta)$, (see Figure A.3) of order n are used to describe the angular dependence of scattering.

The coefficient matrices, $A_n, \mathbf{B_n}, C_n$ and $\mathbf{D_n}$, are dimensionless and are determined by solving the appropriate boundary conditions (Section 2.2.2). Solution for discrete values of n refer to the decomposed modal solutions.

2.2.1 Particle Displacement and Stress

The boundary conditions are expressed using particle displacement and stress. Since infinite pressure gradients are not allowed and the medium remains in contact with the target at all times, particle displacement and stress must be continuous at all interfaces. Expressions for particle displacement can be found in terms of spherical harmonic functions (Equation 2.10 to Equation 2.14) by applying Equation 2.6, which defines the normal particle displacement as the gradient of the scalar potential ($\nabla\phi$) and the tangential particle displacement as the curl of the vector potential ($\nabla\times\psi$) (*Mow and Pao*, 1971; *Graff*, 1975). Expressions for the gradient and curl operator, specified by the coordinate system of the problem, are used to describe normal particle displacement, u_r, and tangential particle displacement (*Graff*, 1975), u_θ, as

$$u_r = \frac{\partial\phi}{\partial r} + \frac{1}{r\sin\theta}\frac{\partial}{\partial\theta}\left(\sin\theta\frac{\partial\psi}{\partial\theta}\right) \tag{2.15}$$

$$u_\theta = \frac{1}{r}\left(\frac{\partial\phi}{\partial\theta} - \frac{\partial}{\partial\theta}\frac{\partial(r\psi)}{\partial r}\right) \tag{2.16}$$

Expressions for normal stress, τ_{rr}, and tangential stress, $\tau_{r\theta}$, are given in *Graff* (1975)

in terms of the elastic properties of the material and particle displacement due to compressional and shear waves.

$$\tau_{rr} = \lambda \left\{ \frac{\partial u_r}{\partial r} + \frac{2u_r}{r} + \frac{1}{r}\frac{\partial u_\theta}{\partial \theta} + \frac{u_\theta \cot\theta}{r} \right\} + 2\mu \left\{ \frac{\partial u_r}{\partial r} \right\} \tag{2.17}$$

$$\tau_{r\theta} = \mu \left\{ \frac{1}{r}\frac{\partial u_r}{\partial \theta} + \frac{\partial u_\theta}{\partial r} + \frac{u_\theta}{r} \right\} \tag{2.18}$$

Using Equations 2.15 and 2.16, the stress-displacement relations can be expressed in terms of scalar and vector potentials (*Graff*, 1975)

$$\begin{aligned} \tau_{rr} = 2\mu \Big\{ & \frac{k_s^2}{2}\phi - \frac{2}{r}\frac{\partial \phi}{\partial r} - \frac{1}{r^2 \sin\theta}\frac{\partial}{\partial \theta}(\sin\theta \frac{\partial \phi}{\partial \theta}) \\ & + \frac{1}{r\sin\theta}\frac{\partial}{\partial \theta}\Big(\sin\theta \big(\frac{\partial^2 \psi}{\partial \theta \partial r} - \frac{1}{r}\frac{\partial \psi}{\partial r} \big) \Big) \Big\} \end{aligned} \tag{2.19}$$

$$\tau_{r\theta} = \mu \frac{\partial}{\partial \theta} \left(\frac{2}{r}\frac{\partial \phi}{\partial r} - \frac{2}{r^2}\phi + k_s^2 \psi + \frac{2}{r}\frac{\partial \psi}{\partial r} + \frac{2}{r^2}\psi + \frac{2}{r^2 \sin\theta}\frac{\partial}{\partial \theta}(\sin\theta \frac{\partial \psi}{\partial \theta}) \right). \tag{2.20}$$

Normal and tangential particle displacements and stresses are required for the three distinct waves (incident, scattered and refracted) in the problem.

2.2.2 Boundary Conditions for Scattering Models

Boundary condition equations describing the continuity of normal particle displacement (Equation 2.21a), continuity of tangential particle displacement (Equation 2.21b), continuity of normal stress (Equation 2.21c) and continuity of tangential stress (Equation 2.21d) are given by

$$[u_r^{(i)}]_{r=a} + [u_r^{(s)}]_{r=a} = [u_r^{(r)}]_{r=a} \tag{2.21a}$$

$$[u_\theta^{(i)}]_{r=a} + [u_\theta^{(s)}]_{r=a} = [u_\theta^{(r)}]_{r=a} \tag{2.21b}$$

$$[\tau_{rr}^{(i)}]_{r=a} + [\tau_{rr}^{(s)}]_{r=a} = [\tau_{rr}^{(r)}]_{r=a} \tag{2.21c}$$

$$[\tau_{r\theta}^{(i)}]_{r=a} + [\tau_{r\theta}^{(s)}]_{r=a} = [\tau_{r\theta}^{(r)}]_{r=a}. \tag{2.21d}$$

These boundary condition equations can be expressed by inserting the appropriate potential functions, from Equations 2.10 to 2.14, into Equations 2.15 to 2.20. The expressions for particle displacement and stress are evaluated at $r = a$, where a is the radius of the sphere. The superscript of the particle displacement and stress terms specify which potential is used (incident, scattered or refracted). The amplitude coefficients, $A_n, \mathbf{B_n}, C_n$ and $\mathbf{D_n}$, can be solved for discrete modes (for $n \geq 0$) using Cramer's rule (*Gaunard and Uberall*, 1978). This requires that there are at least as many boundary condition equations as distinct amplitude coefficients.

Examples of these models have been selected from literature (*Gaunard and Uberall*, 1978; *Flax and Uberall*, 1980; *Gaunard and Uberall*, 1983) and reproduced by solving for the appropriate boundary conditions for a range of material properties, found in Table 2.1 . The boundary condition equations differ for the cases of a solid scatterer in a fluid, a solid scatterer in a solid and a fluid scatterer in solid.

2.2.3 Case I: Solid Sphere in a Fluid Medium

The case of a solid sphere in a fluid medium was modelled by *Faran* (1951) using phase-shift formalism, and has since been verified by numerous experiments (*Faran*, 1951; *Hampton and McKinney*, 1961; *Hickling*, 1962; *Chivers and Anson*, 1982; *Gaunard and Uberall*, 1983). *Gaunard and Uberall* (1983) confirm this result using Cramer's rule to solve for the amplitude coefficients. The shear modulus of the fluid medium is zero ($\mu_1 = 0$). As a result, the fluid cannot support shear waves and the potential $\psi_1^{(s)}$ must be zero; thus, one less boundary condition equation is required. The boundary condition equations simplify to:

$$[u_r^{(i)}]_{r=a}^{Fs} + [u_r^{(s)}]_{r=a}^{Fs} = [u_r^{(r)}]_{r=a}^{Fs} \tag{2.22a}$$

$$[\tau_{rr}^{(i)}]_{r=a}^{Fs} + [\tau_{rr}^{(s)}]_{r=a}^{Fs} = [\tau_{rr}^{(r)}]_{r=a}^{Fs} \tag{2.22b}$$

$$0 = [\tau_{r\theta}^{(r)}]_{r=a}^{Fs} \tag{2.22c}$$

where the superscript $[\,]^{Fs}$ denotes the appropriate elastic parameterization for the case of scatter from a solid sphere in a fluid. *Gaunard and Uberall* (1983) provide a solution for the amplitudes of the scattered longitudinal wave and refracted longitudinal and transverse waves in terms of $d_n(\omega)$ (in Appendix B.1), which express the boundary conditions in terms of material properties and the transmit pulse frequency.

Table 2.1: Material Properties of Target Spheres and Elastic Media

Media	Density [ρ (kg/m^3)]	First Lame Parameter [λ (Gpa)]	Shear Modulus [μ (GPa)]	Compressional Soundspeed [c_l (m/s)]	Shear Soundspeed [c_s (m/s)]	Acoustic Impedance [Z (N s/m^3), $\times 10^6$]
Water [a]	1022 - 1023.5	2.30 - 2.34	0	1500 - 1513	0	1.53 - 1.55
Ice [b]	916.2 - 918.9	4.45-6.87	2.89 - 3.3	3342-3834	1776-1901	3.06 - 3.52
Tungsten Carbide (WC) [c]	14850-14950	185-275	251-258	6802 - 7294	4111 - 4154	101 - 109
Polypropylene (PP) [d]	910 - 946	3.14 - 3.67	0.51 - 1.36	2097 - 2599	748 - 1199	1.94 - 2.46
Air [e]	1.29 - 1.20	0.0014	0	331-343	0	0.0003 - 0.0004

[a] *Mackenzie* (1981)
[b] *Timco and Weeks* (2010)
[c] *Gerlich and Kennedy* (1979)
[d] *Chan et al.* (1978)
[e] *Wong and Embleton* (1985)

$$\begin{bmatrix} d_n^{(11)}(\omega) & d_n^{(12)}(\omega) & d_n^{(13)}(\omega) \\ d_n^{(21)}(\omega) & d_n^{(22)}(\omega) & d_n^{(23)}(\omega) \\ d_n^{(31)}(\omega) & d_n^{(32)}(\omega) & d_n^{(33)}(\omega) \end{bmatrix} \begin{bmatrix} A_n^{Fs}(\omega) \\ C_n^{Fs}(\omega) \\ \mathbf{D_n}^{Fs}(\omega) \end{bmatrix} = \begin{bmatrix} d_n^{(10)}(\omega) \\ d_n^{(20)}(\omega) \\ d_n^{(30)}(\omega) \end{bmatrix} \tag{2.23}$$

Frequency dependent solutions for the amplitudes of discrete vibrational modes (n) of the scattered compressional wave are calculated using Cramer's Rule (*Gaunard and Uberall*, 1983), where

$${A_n}^{Fs}(\omega) = \begin{vmatrix} d_n^{(10)}(\omega) & d_n^{(12)}(\omega) & d_n^{(13)}(\omega) \\ d_n^{(20)}(\omega) & d_n^{(22)}(\omega) & d_n^{(23)}(\omega) \\ d_n^{(30)}(\omega) & d_n^{(32)}(\omega) & d_n^{(33)}(\omega) \end{vmatrix} \begin{vmatrix} d_n^{(11)}(\omega) & d_n^{(12)}(\omega) & d_n^{(13)}(\omega) \\ d_n^{(21)}(\omega) & d_n^{(22)}(\omega) & d_n^{(23)}(\omega) \\ d_n^{(31)}(\omega) & d_n^{(32)}(\omega) & d_n^{(33)}(\omega) \end{vmatrix}^{-1} \tag{2.24}$$

and $|\ |$ is the determinant of the inset matrix.

The first five vibrational modes for a range of material properties with respect to transmit frequency and the size of the sphere are provided in Figure 2.2 which shows that the locations of resonances are independent of changes in water properties and slightly dependent on the properties of the tungsten carbide sphere.

2.2.4 Case II: Solid Sphere in a Solid Medium

The full set of boundary conditions are required to solve the scattering amplitudes from a solid sphere encased in a solid elastic medium, since both the medium and target can support both compressional and shear waves. The full set of boundary condition equations are required, where:

$$[u_r^{(i)}]_{r=a}^{Ss} + [u_r^{(s)}]_{r=a}^{Ss} = [u_r^{(r)}]_{r=a}^{Ss} \tag{2.25a}$$

$$[u_\theta^{(i)}]_{r=a}^{Ss} + [u_\theta^{(s)}]_{r=a}^{Ss} = [u_\theta^{(r)}]_{r=a}^{Ss} \tag{2.25b}$$

$$[\tau_{rr}^{(i)}]_{r=a}^{Ss} + [\tau_{rr}^{(s)}]_{r=a}^{Ss} = [\tau_{rr}^{(r)}]_{r=a}^{Ss} \tag{2.25c}$$

$$[\tau_{r\theta}^{(i)}]_{r=a}^{Ss} + [\tau_{r\theta}^{(s)}]_{r=a}^{Ss} = [\tau_{r\theta}^{(r)}]_{r=a}^{Ss} \tag{2.25d}$$

where the superscript $[\,]^{Ss}$ denotes the appropriate elastic parameterization for the case of scatter from a solid sphere in a solid. *Flax and Uberall* (1980) provide a solution for

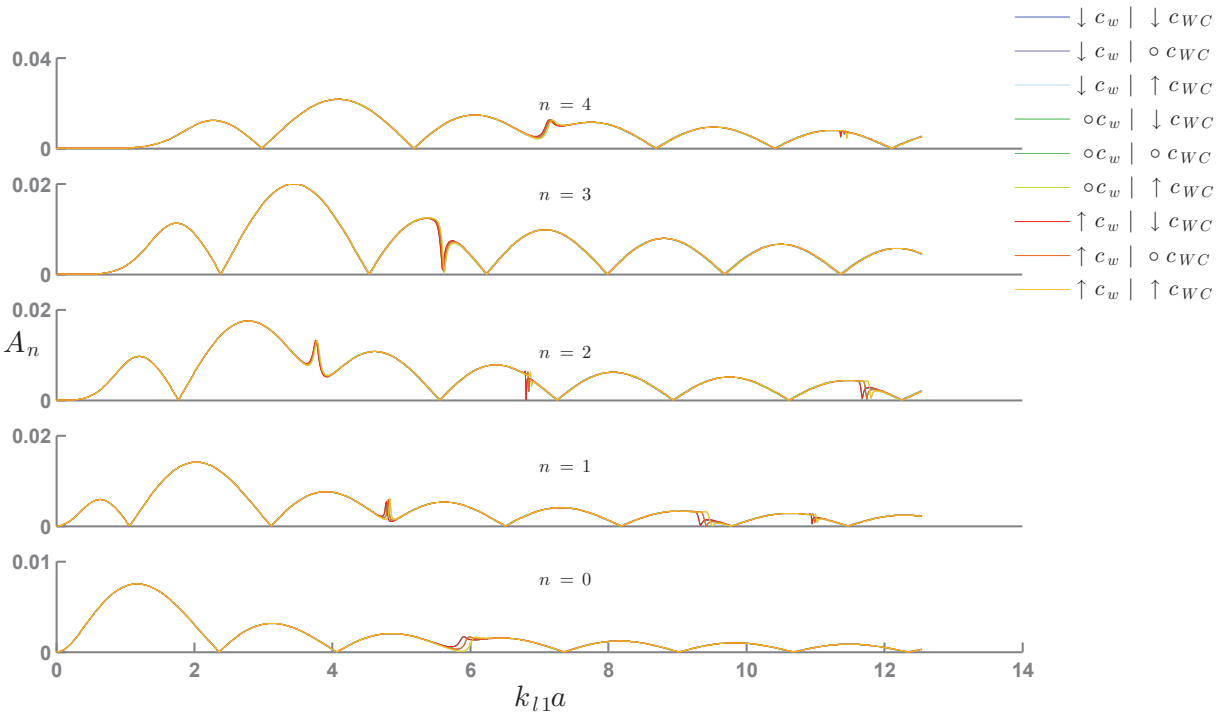

Figure 2.2: The first five vibrational modes for the amplitude coefficient for a compressional wave scattered from a solid sphere in a fluid medium using *Gaunard and Uberall* (1983); calculated for a tungsten carbide sphere in water using a range of material properties, where $\circ c$ is the median soundspeed, $\uparrow c$ is the highest expected soundspeed, $\downarrow c$ the lowest expected soundspeed (see Table 2.1).

the amplitude of the scattered longitudinal wave in terms of $a_n(\omega)$ (Appendix B.2), which express the boundary conditions in terms of material properties and the transmit pulse frequency.

$$\begin{bmatrix} b_n^{(11)}(\omega) & b_n^{(12)}(\omega) & b_n^{(13)}(\omega) & b_n^{(14)}(\omega) \\ b_n^{(21)}(\omega) & b_n^{(22)}(\omega) & b_n^{(23)}(\omega) & b_n^{(24)}(\omega) \\ b_n^{(31)}(\omega) & b_n^{(32)}(\omega) & b_n^{(33)}(\omega) & b_n^{(34)}(\omega) \\ b_n^{(41)}(\omega) & b_n^{(42)}(\omega) & b_n^{(43)}(\omega) & b_n^{(44)}(\omega) \end{bmatrix} \begin{bmatrix} A_n^{Ss} \\ \mathbf{B_n}^{Ss} \\ C_n^{Ss} \\ \mathbf{D_n}^{Ss} \end{bmatrix} = \begin{bmatrix} b_n^{(10)}(\omega) \\ b_n^{(20)}(\omega) \\ b_n^{(30)}(\omega) \\ b_n^{(40)}(\omega) \end{bmatrix} \tag{2.26}$$

Frequency dependent solutions for the amplitudes of discrete vibrational modes of the scattered compressional wave are calculated using Cramer's Rule (*Flax and Uberall*, 1980), where

$$A_n^{Ss}(\omega) = \begin{vmatrix} b_n^{(10)}(\omega) & b_n^{(12)}(\omega) & b_n^{(13)}(\omega) & b_n^{(14)}(\omega) \\ b_n^{(20)}(\omega) & b_n^{(22)}(\omega) & b_n^{(23)}(\omega) & b_n^{(24)}(\omega) \\ b_n^{(30)}(\omega) & b_n^{(32)}(\omega) & b_n^{(33)}(\omega) & b_n^{(34)}(\omega) \\ b_n^{(40)}(\omega) & b_n^{(42)}(\omega) & b_n^{(43)}(\omega) & b_n^{(44)}(\omega) \end{vmatrix} \begin{vmatrix} b_n^{(11)}(\omega) & b_n^{(12)}(\omega) & b_n^{(13)}(\omega) & b_n^{(14)}(\omega) \\ b_n^{(21)}(\omega) & b_n^{(22)}(\omega) & b_n^{(23)}(\omega) & b_n^{(24)}(\omega) \\ b_n^{(31)}(\omega) & b_n^{(32)}(\omega) & b_n^{(33)}(\omega) & b_n^{(34)}(\omega) \\ b_n^{(41)}(\omega) & b_n^{(42)}(\omega) & b_n^{(43)}(\omega) & b_n^{(44)}(\omega) \end{vmatrix}^{-1} \tag{2.27}$$

The first five vibrational modes for a range of material properties with respect to transmit frequency and the size of the sphere are provided in Figure 2.3 which shows that the locations of resonances depend upon the properties of the ice and the tungsten carbide sphere.

2.2.5 Case III: Fluid-Filled Sphere in a Solid Medium

When a sphere encased in a solid medium is filled with fluid, the sphere will not be able to support shear waves and the potential $[\psi_2^{(r)}]^{Sf}$ must be zero and one less boundary

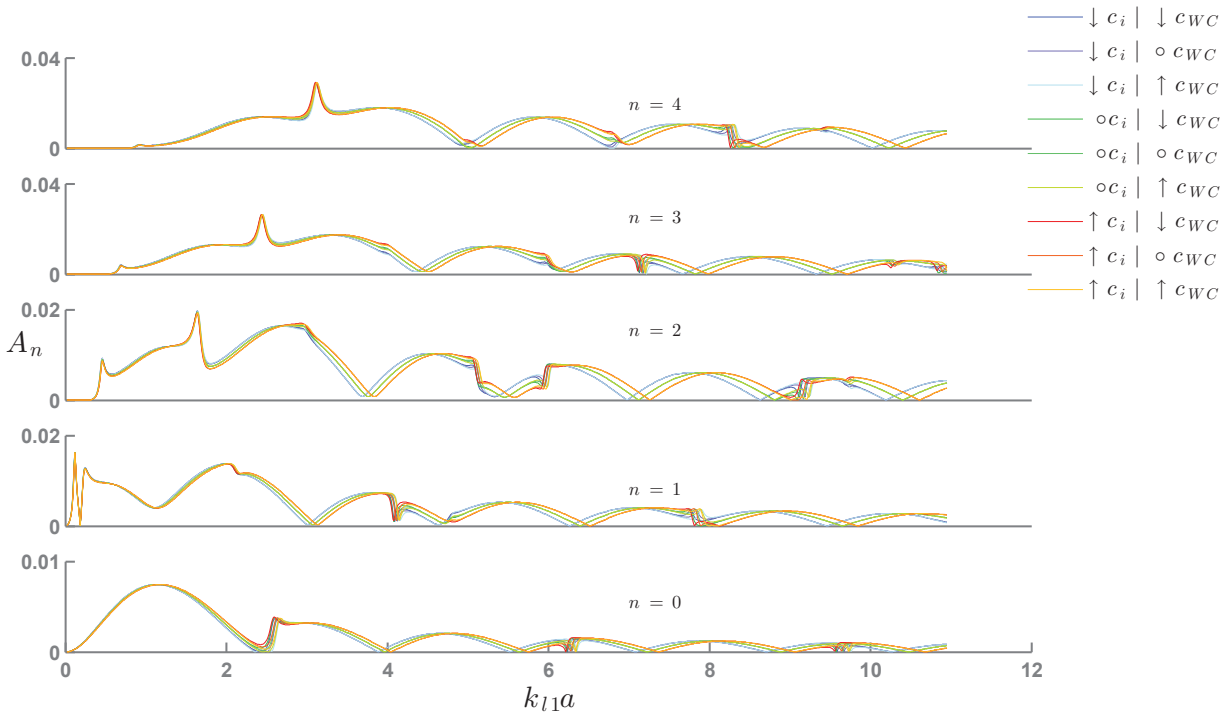

Figure 2.3: The first five vibrational modes for the amplitude coefficient for a compressional wave scattered from a solid sphere in a solid medium using *Flax and Uberall* (1980); calculated for a tungsten carbide sphere in ice using a range of material properties, where $\circ c$ is the median soundspeed, $\uparrow c$ is the highest expected soundspeed, $\downarrow c$ the lowest expected soundspeed (see Table 2.1).

condition equation is required. In this case, the boundary condition equations simplify to:

$$[u_r^{(i)}]_{r=a}^{Sf} + [u_r^{(s)}]_{r=a}^{Sf} = [u_r^{(r)}]_{r=a}^{Sf} \tag{2.28a}$$

$$[\tau_{rr}^{(i)}]_{r=a}^{Sf} + [\tau_{rr}^{(s)}]_{r=a}^{Sf} = [\tau_{rr}^{(r)}]_{r=a}^{Sf} \tag{2.28b}$$

$$[\tau_{r\theta}^{(i)}]_{r=a}^{Sf} + [\tau_{r\theta}^{(s)}]_{r=a}^{Sf} = 0 \tag{2.28c}$$

where the superscript $[\,]^{Sf}$ denotes the appropriate elastic parameterization for the case of scatter from a fluid sphere in a solid. *Gaunard and Uberall* (1978) provide a solution for the amplitude of the scattered longitudinal wave in terms of $c_n(\omega)$ (Appendix B.3), which express the boundary conditions in terms of material properties and the transmit pulse frequency.

$$\begin{bmatrix} c_n^{(11)}(\omega) & c_n^{(12)}(\omega) & c_n^{(13)}(\omega) \\ c_n^{(21)}(\omega) & c_n^{(22)}(\omega) & c_n^{(23)}(\omega) \\ c_n^{(31)}(\omega) & c_n^{(32)}(\omega) & c_n^{(33)}(\omega) \end{bmatrix} \begin{bmatrix} A_n^{Sf}(\omega) \\ \mathbf{B_n}^{Sf}(\omega) \\ C_n^{Sf}(\omega) \end{bmatrix} = \begin{bmatrix} c_n^{(10)}(\omega) \\ c_n^{(20)}(\omega) \\ c_n^{(30)}(\omega) \end{bmatrix} \tag{2.29}$$

Frequency dependent solutions for the amplitudes of discrete vibrational modes of the scattered compressional wave are calculated using Cramer's Rule (*Gaunard and Uberall*, 1978), where

$$A_n{}^{Sf}(\omega) = \begin{vmatrix} c_n^{(10)}(\omega) & c_n^{(12)}(\omega) & c_n^{(13)}(\omega) \\ c_n^{(20)}(\omega) & c_n^{(22)}(\omega) & c_n^{(23)}(\omega) \\ c_n^{(30)}(\omega) & c_n^{(32)}(\omega) & c_n^{(33)}(\omega) \end{vmatrix} \begin{vmatrix} c_n^{(11)}(\omega) & c_n^{(12)}(\omega) & c_n^{(13)}(\omega) \\ c_n^{(21)}(\omega) & c_n^{(22)}(\omega) & c_n^{(23)}(\omega) \\ c_n^{(31)}(\omega) & c_n^{(32)}(\omega) & c_n^{(33)}(\omega) \end{vmatrix}^{-1} \tag{2.30}$$

The first five vibrational modes for a range of material properties with respect to transmit frequency and the size of the sphere are provided in Figure 2.4 which shows that the locations of resonances depend upon the properties of the ice and are independent of the elastic properties of the air inclusion.

2.2.6 Case IV: Fluid-Filled, Spherical Elastic Shell in Water

The case of acoustic scattering from a fluid sphere in water has been modelled by *Anderson* (1950) (see Figure 2.5), using the same method of enforcing continuity of stress and

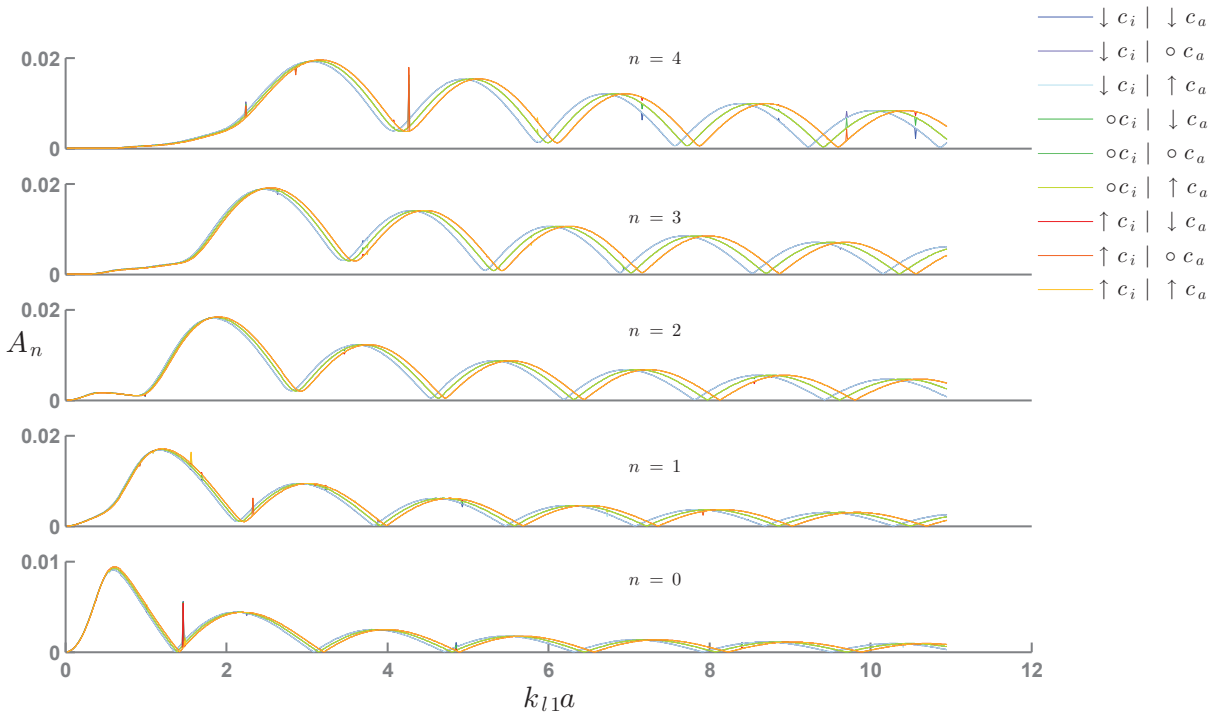

Figure 2.4: The first five vibrational modes for the amplitude coefficient for a compressional wave scattered from a fluid sphere in a solid medium using *Gaunard and Uberall* (1978); calculated for an air cavity in ice using a range of material properties, where $\circ c$ is the median soundspeed, $\uparrow c$ is the highest expected soundspeed, $\downarrow c$ the lowest expected soundspeed (see Table 2.1).

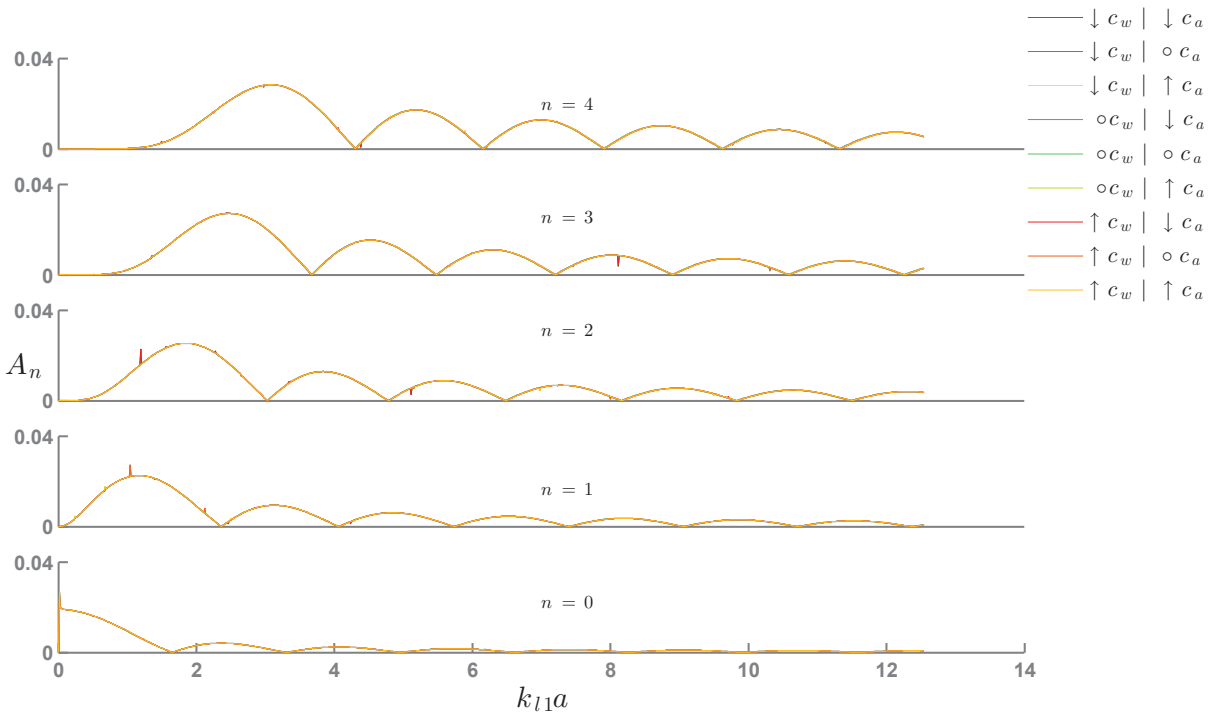

Figure 2.5: The first five vibrational modes for the amplitude coefficient for a compressional wave scattered from a fluid sphere in a fluid medium using *Anderson* (1950); calculated for an air bubble in water using a range of material properties, where $\circ c$ is the median soundspeed, $\uparrow c$ is the highest expected soundspeed, $\downarrow c$ the lowest expected soundspeed (see Table 2.1).

particle displacement across the interface of the sphere, where both the medium and sphere cannot support shear waves. Thus, only two boundary condition equations are required; continuity of pressure and continuity of normal particle displacement.

$$[u_r^{(i)}]_{r=a}^{Ff} + [u_r^{(s)}]_{r=a}^{Ff} = [u_r^{(r)}]_{r=a}^{Ff} \tag{2.31a}$$

$$[\tau_{rr}^{(i)}]_{r=a}^{Ff} + [\tau_{rr}^{(s)}]_{r=a}^{Ff} = [\tau_{rr}^{(r)}]_{r=a}^{Ff} \tag{2.31b}$$

An expressions for the amplitude of the scattered compressional wave A_n^{Ff} is given in *Anderson* (1950). The first five vibrational modes for a range of material properties with respect to transmit frequency and the size of the sphere are provided in Figure 2.5 which shows that the scattered compressional wave does not vary with the elastic properties of the water or air bubble.

A solid shell is used to maintain a fluid sphere in water with a consistent size. This case

has been modelled for shells of different sizes (*Gaunard and Werby*, 1985, 1987, 1991). In this case, the elastic shell can support shear waves; although neither the water or the fluid enclosed in the elastic shell will support shear waves. Six boundary conditions are required to describe the incident and scattered compressional waves, the compressional and shear waves refracted into the elastic shell and scattered from the encased fluid, and the wave refracted into the encased fluid.

$$[u_r^{(i)}]_{r=a_2}^{Fs} + [u_r^{(s)}]_{r=a_2}^{Fs} = [u_r^{(r)}]_{r=a_2}^{Fs} \tag{2.32a}$$

$$[\tau_{rr}^{(i)}]_{r=a_2}^{Fs} + [\tau_{rr}^{(s)}]_{r=a_2}^{Fs} = [\tau_{rr}^{(r)}]_{r=a_2}^{Fs} \tag{2.32b}$$

$$0 = [\tau_{r\theta}^{(r)}]_{r=a_2}^{Fs} \tag{2.32c}$$

$$[u_r^{(i)}]_{r=a_1}^{sf} + [u_r^{(s)}]_{r=a_1}^{sf} = [u_r^{(r)}]_{r=a_1}^{sf} \tag{2.32d}$$

$$[\tau_{rr}^{(i)}]_{r=a_1}^{sf} + [\tau_{rr}^{(s)}]_{r=a_1}^{sf} = [\tau_{rr}^{(r)}]_{r=a_1}^{sf} \tag{2.32e}$$

$$[\tau_{r\theta}^{(i)}]_{r=a_1}^{sf} + [\tau_{r\theta}^{(s)}]_{r=a_1}^{sf} = 0 \tag{2.32f}$$

where, $[\,]^{Fs}$ denotes waves in the water incident on the elastic shell and $[\,]^{sf}$ denotes waves in the shell incident on the enclosed fluid, a_1 is the radius of the fluid sphere enclosed by the shell and a_2 is the radius of the shell; thus, the shell thickness is $a_2 - a_1$. The wave refracted into the shell is the wave scattered from the fluid inclusion (for example, $[\tau_{rr}^{(r)}]_{r=a_2}^{Fs} \approx [\tau_{rr}^{(i)}]_{r=a_1}^{sf}$).

The amplitude coefficient of a scattered wave is found using the same methodology in Sections 2.2.3 to 2.2.5, where the dimensionless coefficients used to solve the boundary condition equations are given in *Gaunard and Werby* (1987). The magnitude of the scattered longitudinal wave is a function of the material properties of the water, elastic shell and enclosed fluid; as well as the thickness of the shell (*Gaunard and Werby*, 1987). The first five vibrational modes for a range of material properties are given in Figure 2.6, which shows that the location of the resonances depends on the elastic properties of the shell.

2.2.7 Planar Fluid-Solid Interface

If the target is encased in a solid medium and ensonified with a sound source that is outside this medium, as for a target inside a submerged block of ice with an echosounder in the

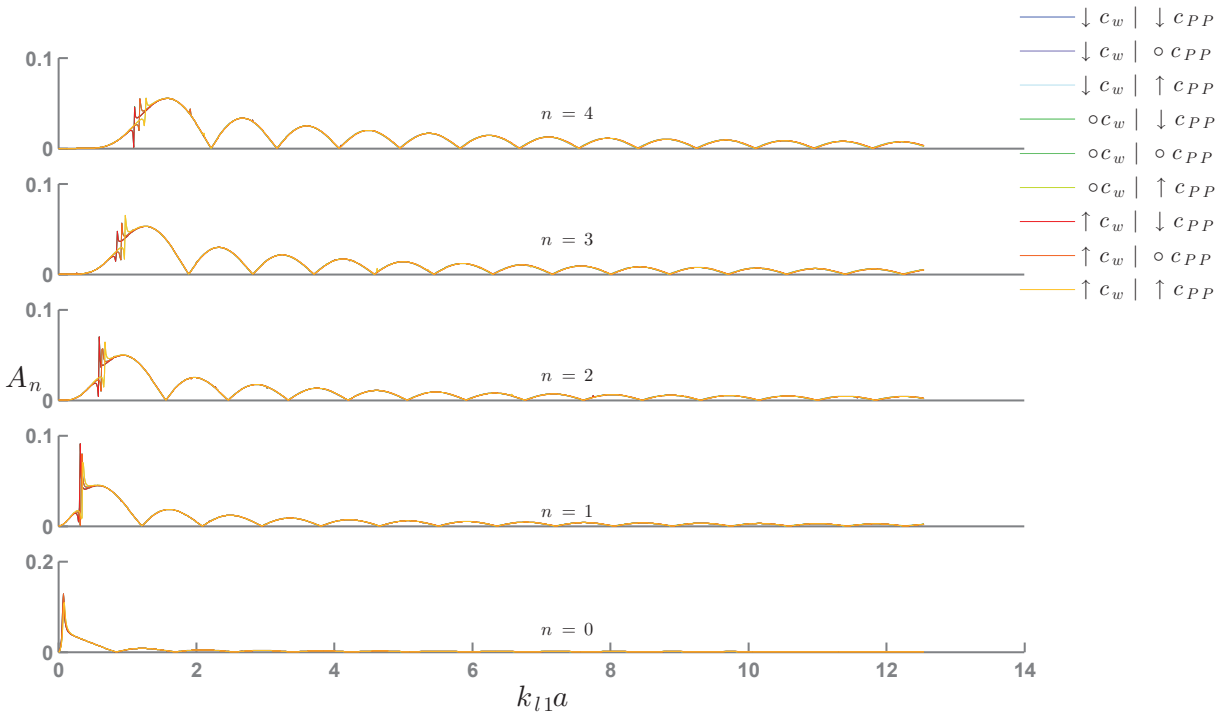

Figure 2.6: The first five vibrational modes for the amplitude coefficient for a compressional wave scattered from a fluid-filled shell in a fluid medium using *Gaunard and Werby* (1987); calculated for an air-filled polypropylene shell in water using a range of material properties, where $\circ c$ is the median soundspeed, $\uparrow c$ is the highest expected soundspeed, $\downarrow c$ the lowest expected soundspeed (see Table 2.1).

water, both the incident and transmitted wave will have to pass through the surface of the solid. This will affect the amplitude of the acoustic wave that is incident on the sphere, and thus the amplitude of the wave scattered from the sphere.

The reflection of sound from a planar water/ice interface was modelled by *Langleben* (1970), *Mayer et al.* (1975) and *Jezek* (1985). Both *Langleben* (1970) and *Mayer et al.* (1975) model the reflection by ignoring shear waves transmitted into the ice, and it is assumed that the incident pulse is appropriately short so that multiple reflections can be ignored, that lateral waves (ie. surface and flexural waves) can be ignored and that bulk material properties are consistent throughout the ice. Observations from *Crary* (1954) and *Rothlisberger* (1972) show that this model can reproduce observed reflections from ice surfaces.

The energy scattered at a planar solid interface will be a function of the change in elastic properties between the solid medium and surrounding fluid and also the shape, size, orientation and roughness of the interface with respect to the incident acoustic beam (*Kinsler et al.*, 1972). Assuming a planar interface with negligible surface roughness, surface reflection and transmission is given by *Langleben* (1970) as,

$$R_{12} = \frac{(Z_2/Z_1 - \cos\vartheta_t/\cos\vartheta_i)^2}{(Z_2/Z_1 + \cos\vartheta_t/\cos\vartheta_i)^2} \tag{2.33}$$

$$T_{12} = \frac{((4\ Z_2\cos\vartheta_t)/(Z_1\cos\vartheta_i))^2}{(Z_2/Z_1 + \cos\vartheta_t/\cos\vartheta_i)^2} \tag{2.34}$$

where R_{12} is the reflection coefficient and T_{12} is the transmission coefficient. The subscript denotes the medium, where 1 refers to the surrounding medium and 2 refers to the solid medium of interest. The specific acoustic impedance, Z, defined as $Z = \rho c$, expresses the ability of the medium to redistribute acoustic energy, ignoring possible shear wave generation. The angle of incidence, ϑ_i, and the transmission angle, ϑ_t, are related by Snell's Law as $\vartheta_t = \cos^{-1}\left(\sqrt{1 - (\frac{c_2\sin\vartheta_i}{c_1})^2}\right)$. The critical angle, ϑ_c, is the largest angle where transmission occurs, defined by Snell's Law as $\vartheta_c = \sin^{-1}(\frac{c_1}{c_2})$. If $\vartheta_i > \vartheta_c$, then R_{12} = 1 and T_{12} = 0.

Jezek (1985) updates this model to incorporate shear, surface and flexural waves in ice; however, since the models for spheres encased in solid media (Sections 2.2.4 and 2.2.5) assume that only a longitudinal wave is incident on the sphere, I did not model shear wave

transmission.

2.3 Expressions for Backscattering

2.3.1 Backscattering Cross Section

An acoustic far-field energy flux can be calculated using the amplitude coefficients for the scattered compressional wave (A_n) for a sufficient number of modes.

The scattered pressure is expressed in terms of a form function, $f_\infty(r, \theta, \omega)$, calculated in terms of range, scattering angle and acoustic frequency. The form function is the scattered compressional wave ($\phi_1^{(s)}$), normalized by the incident wave (*Gaunard and Uberall*, 1978) and has dimensions of meters.

$$\begin{aligned} f_\infty(r, \theta, \omega) &= \frac{\phi_1^{(s)}}{\frac{\phi_0}{r} e^{i(k_{l1} r - \omega t)}} \\ &= \frac{r \sum_{n=0}^{\infty} i^n (2n+1)\ A_n\ h_n(k_{l1} r) P_n(\cos\theta)}{e^{i(k_{l1} r)}} \end{aligned} \tag{2.35}$$

The asymptotic approximation ($kr \gg 1$) of the spherical Hankel function is applied when the observation is separated from the object by many wavelengths (*Gaunard and Uberall*, 1978),

$$h_n(kr) \overrightarrow{_{kr>>1}} (-i)^{n+1} \frac{e^{ikr}}{kr}. \tag{2.36}$$

In the case of a monostatic system, the receiver and transmitter are the same and only backscattering is observed, thus $\theta = \pi$, where $P_n(cos(\pi)) = (-1)^n$ (*Sessarego et al.*, 1998) and the far-field backscattering form function simplifies to

$$f_\infty(\pi, \omega) = \frac{1}{ik_{l1}} \sum_{n=0}^{\infty} (-1)^n (2n+1)\ A_n(\omega). \tag{2.37}$$

The acoustic backscattering cross section, σ_{bs}, can be calculated from this form function,

$$\sigma_{bs}(\omega) = \left(|f_\infty(\pi, \omega)|\right)^2. \tag{2.38}$$

The sum of amplitude coefficients converges when $n > k_{l2}a + 5$ (*Gaunard and Uberall*, 1978). The higher order modes model partial wave returns that extend the envelope of a scattered wave and are responsible for certain resonances (*Gaunard and Uberall*, 1983). In the case that a measured wave envelope is truncated to better isolate a target, models summed over fewer modes provide an accurate representation of the front of the return (*Reeder*, 2002).

2.3.2 Target Strength

2.3.2.1 Ice Surfaces

The expected target strength (TS) of the ice surface reflection (*Brekhovskikh and Lysanov*, 1982) is

$$TS_{Rt} = 10\ log_{10}\left(\frac{R_{12}}{2r_{I1}}\right) \tag{2.39}$$

where r_{I1} is the range to the top ice surface. In the case of a finite solid encasing medium, a reflection from the bottom surface may also be identified. The wave incident on the bottom surface and the scattered wave will pass through the top ice surface. The expected TS from the bottom surface reflection is

$$TS_{Rb} = 10\ log_{10}\left(\frac{T_{12}T_{21}R_{21}}{2r_{I2}}\right) \tag{2.40}$$

where r_{I2} is the range to the bottom ice surface. The range dependence in this model is due to the assumption that the surface of the ice is semi-infinite, compared to the size of the beam. This assumption holds if the footprint of the beam is fully contained on the solid surface.

This model does not include the effect of diffraction at the edges of the solid matrix, shear wave reflection and transmission or mode conversion. The reflection from the surface is modelled as though the beam width is narrower than the lateral extent of the ice surface. In this case that footprint of the beam is not fully contained on the solid surface, the intensity of the reflected wave should scale according to diffraction from a rectangular aperture (*Goodman*, 1996), where the intensity as a function of angle is $R_{12}(\theta_r) = \text{sinc}(\frac{\pi W \sin(\theta)}{\lambda})$, where W is the width of the ice block, θ_r is the angle of the receiver from the edge of the block that intersects the beam and λ is the acoustic wavelength (*Goodman*, 1996). In this case, Equation 2.39 is not expected to accurately predict the magnitude of the wave

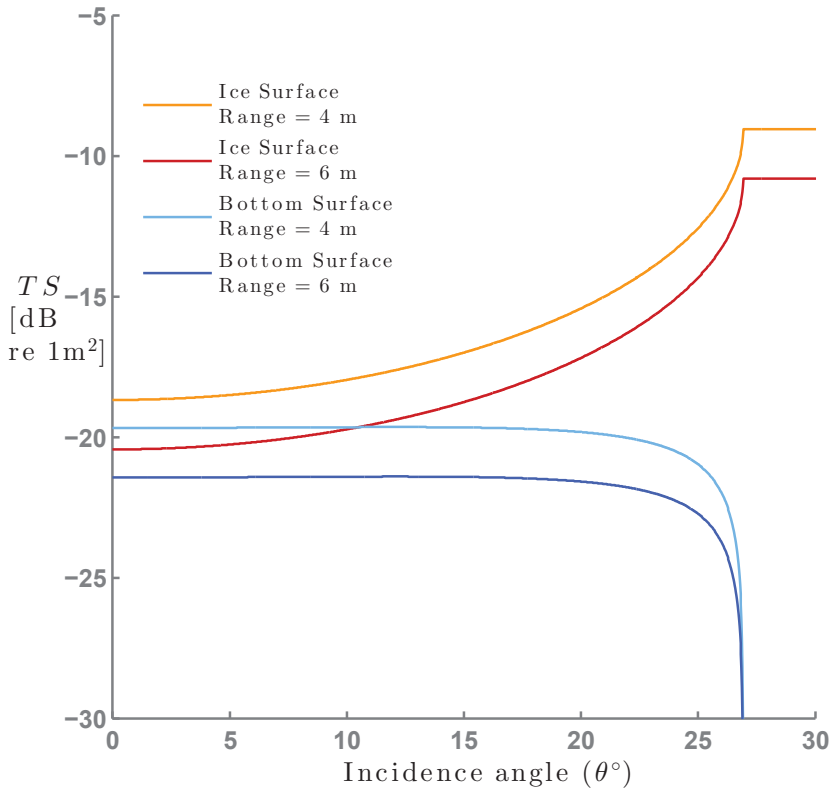

Figure 2.7: Modelled Target Strength from a planar ice-water interface using *Langleben* (1970) as a function of incidence angle. The reflection from the top surface (using Equation 2.39; red and orange) and bottom surface (using Equation 2.40; dark and light blue) are given for multiple ranges of the surface from the transducer.

scattered at the surface of the solid; however, Equations 2.33 and 2.34 will provide a useful estimate of the energy that is removed from the wave incident on the sphere and the wave scattered from the sphere at the interface of the solid. Figure 2.7 shows that the strength of the reflection increases at non-normal incidence and decreases with the range of the surface from the transducer. A critical angle occurs at 27° where the wave no longer penetrates the ice surface and is totally reflected.

2.3.2.2 Target Spheres

If I assume that scattering from the ice surfaces and multiple inclusions are incoherent, the backscattering cross sections of each scatterer within the beam are combined to calculate the far-field energy flux through $1m^2$, reported as TS in decibels.

$$TS_o(\omega) = 10\log_{10}\left(\sum^{V_{sam}} \frac{\sigma_{bs}(\omega)}{1\text{m}^2}\right) \tag{2.41a}$$

$$TS_i(\omega) = 10\log_{10}\left(T_{12}T_{21}\sum^{V_{sam}} \frac{\sigma_{bs}(\omega)}{1\text{m}^2}\right) \tag{2.41b}$$

$$TS_I(\omega) = 10\log_{10}\left(T_{12}T_{21}\sum^{V_{sam}} \sigma_{bs}(\omega) + \frac{R_{12}}{2r} + \frac{T_{12}T_{21}R_{21}}{2r}\Big/1\text{m}^2\right) \tag{2.41c}$$

where TS_o is the expected target strength of target spheres in water, TS_i of targets in ice and TS_I of the entire return from the ice. The echoes that pass through the ice surface are compensated using the transmission coefficients, T_{12} and T_{21}. $\sum^{V_{sam}} \sigma_{bs}(\omega)$ represents a linear combination of backscattering cross sections for all target spheres in a given sample volume, V_{sam} (see Section 3.2.2). While the assumption that scattering from multiple spheres in ice is incoherent is over-simplistic, since the spherical targets are fixed in the ice block and not randomly distributed, it provides a first-order estimate of the scattering amplitude from multiple spheres. For ice with no inclusions, I assume $\sum^{V_{sam}} \sigma_{bs}(\omega) = 0$.

Figure 2.8 provides TS from spheres in ice and water over a range of frequencies and sphere sizes.

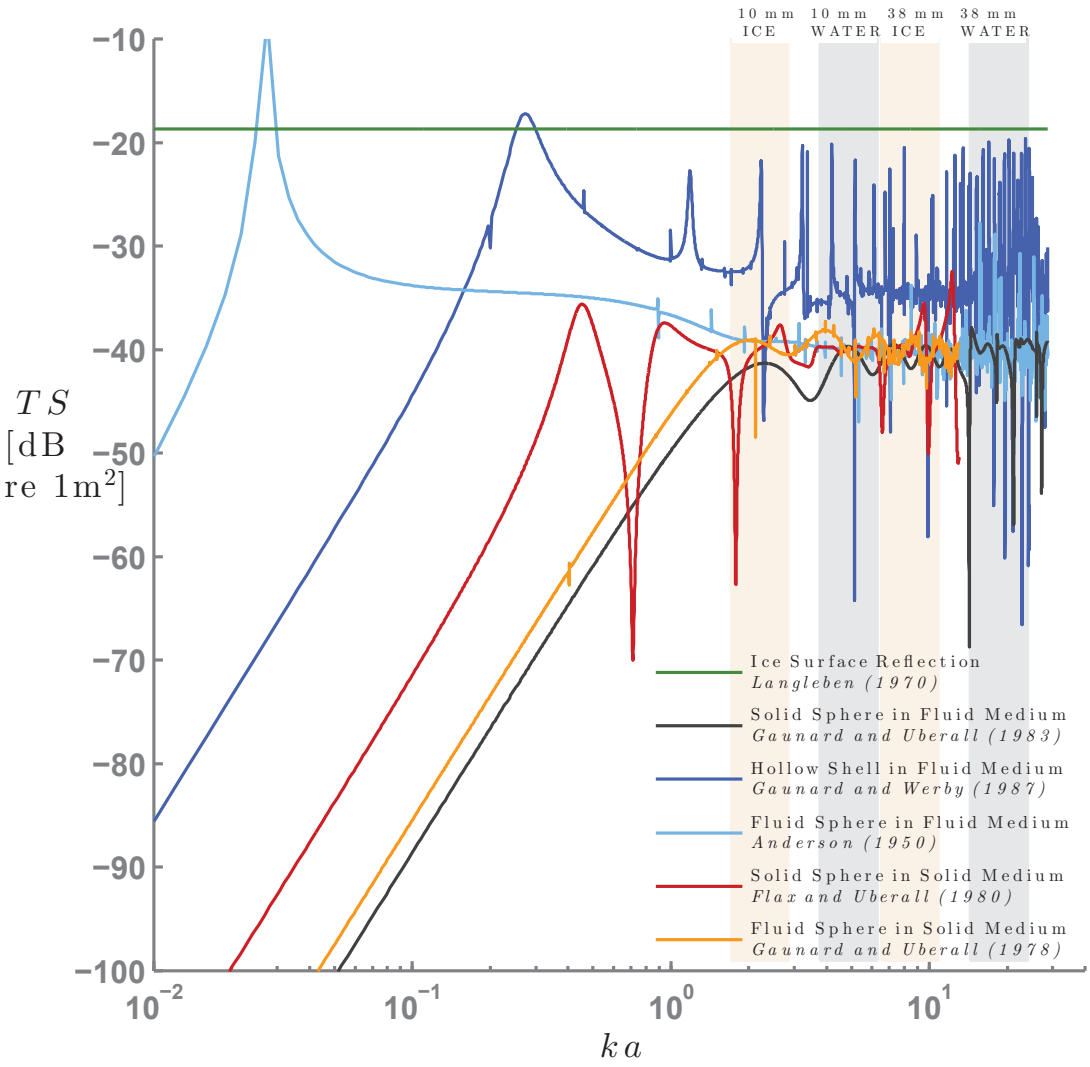

Figure 2.8: Target Strengths for spheres in water (blue and black solid lines) and ice (red and orange solid lines) as a function of frequency and medium properties (where $k = \omega/c$) and sphere radius (a). The models are parameterized for a tungsten-carbide sphere in water (black) and ice (red), an air bubble in water (light blue) and ice (orange) and an air-filled polypropylene shell in water (dark blue). The TS from an ice surface reflection at normal incidence and 4 meters depth, is provided as a solid green line. Patches represent the frequency dependent TS expected from 10 mm and 38 mm spheres in water (grey patches) and ice (tan patches).

CHAPTER 3

METHODS

Acoustic scattering data are interpreted by comparing observations with mathematical models for the cases of a solid (*Faran*, 1951; *Gaunard and Uberall*, 1983) and fluid (*Anderson*, 1950) spherical scatterer in a fluid medium and a solid (*Flax and Uberall*, 1980) or fluid-filled inclusion in a solid medium (*Gaunard and Uberall*, 1978). Acoustic backscattering observations from solid and air-filled spheres in water and ice were collected with a monostatic, 85kHz-155kHz broadband echosounder system.

3.1 Backscattering Measurements

Acoustic backscattering measurements of solid and air-filled spheres in water and ice were collected in the Aquatron Tower Tank at Dalhousie University in Halifax, Nova Scotia in September and October 2012 and August 2014.

3.1.1 The Echosounder

A monostatic echosounder system (Scifish 2100-B) (see Figure 3.1) contained a 17-cm diameter single-beam piston-type broadband transducer with a centre frequency of 120 kHz and a 70kHz bandwidth. The transducer is assumed to produce an approximately conical beam with side lobes, whose strength varied with angle, as seen in Figure 3.2. The main lobe was the most energetic region of the beam, aligned with the centre of the transducer, and had a full beam-width, $\theta_b(\omega)$, between 16° at 90 kHz and 8° at 150 kHz. The effects of the side lobes were not observed in backscattering in the tank. The footprint of the main lobe of the beam, $A_b(\omega)$, is a function of the transducer diameter, D, the range of the leading edge of the acoustic beam, $R_b(\omega)$, and the transducer beam angle,

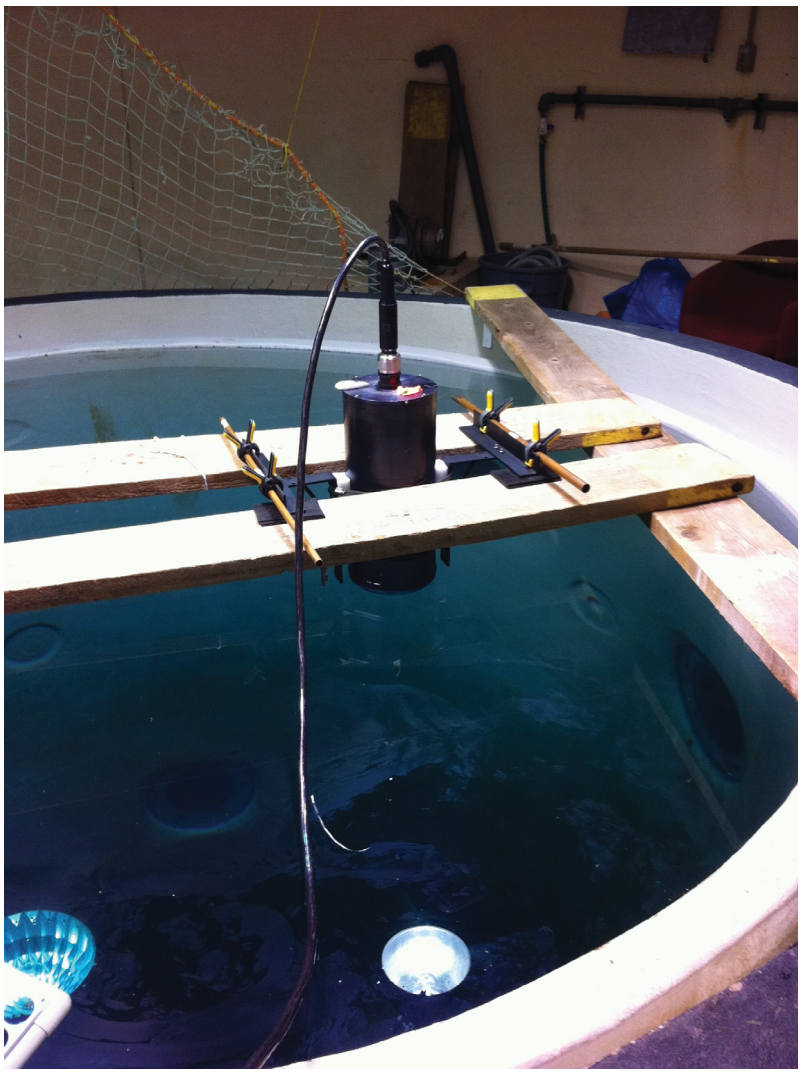

Figure 3.1: The Scifish 2100-B Broadband Sonar setup in the 10-meter deep Aquatron Tower Tank. Targets were centred underneath the echosounder that both transmitted and received acoustic pulses.

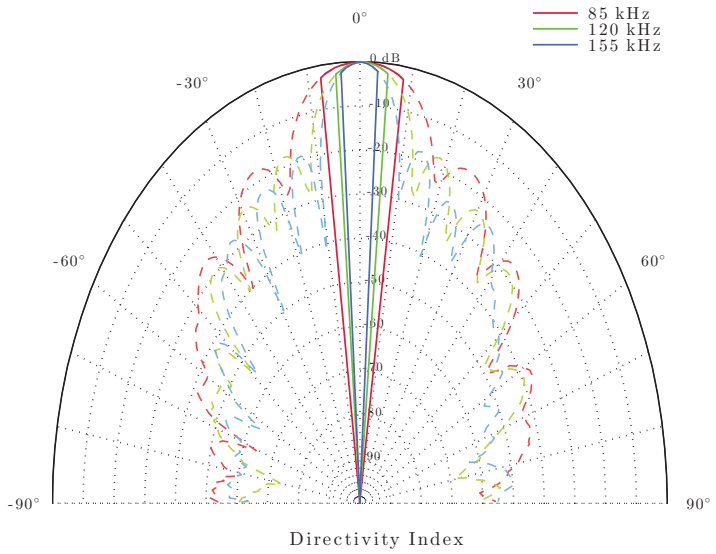

Figure 3.2: The Directivity Index of the SciFish 2100-B, measured on December 14th, 2007, shows the frequency dependent main lobes (solid line) and side lobes (dashed line) of the transmitted beam. The conical main lobe is the region of the beam that is at least -3 dB below the centre of the beam, where the transmit pulse is strongest.

$\theta_b(\omega)$; where $A_b = \pi r_b(\omega)^2$, and $r_b(\omega)$ is the beam radius (see Table 3.1) (*Simmonds and MacLennan*, 2005). The range of the beam is $R = ct/2$ where c is the soundspeed in the tank.

The sampling volume, $V_b(\omega)$ (see Figure 3.3) is

$$V_b(\omega) = \frac{\pi}{3}\Delta R\left(r_t^2(\omega) + r_t(\omega)r_b(\omega) + r_b^2(\omega)\right) \tag{3.1a}$$

$$r_t(\omega) = (R_b - \Delta R)\tan\left(\frac{\theta_b(\omega)}{2}\right) + \frac{D}{2} \tag{3.1b}$$

$$r_b(\omega) = R_b\tan\left(\frac{\theta_b(\omega)}{2}\right) + \frac{D}{2} \tag{3.1c}$$

where, ΔR is the depth of the sampling volume, r_t is the radius of the beam at the top of the sampling volume and r_b is the radius of the beam at the bottom of the sampling volume and $\theta_b(\omega)$ is the frequency dependent beam angle. The height of the sampling volume is discussed in Section 3.2.2.

The intensity of the beam is affected by diffraction near the transducer. The effect of diffraction is negligible past the far-field distance of the transducer, R_{ff}, given by

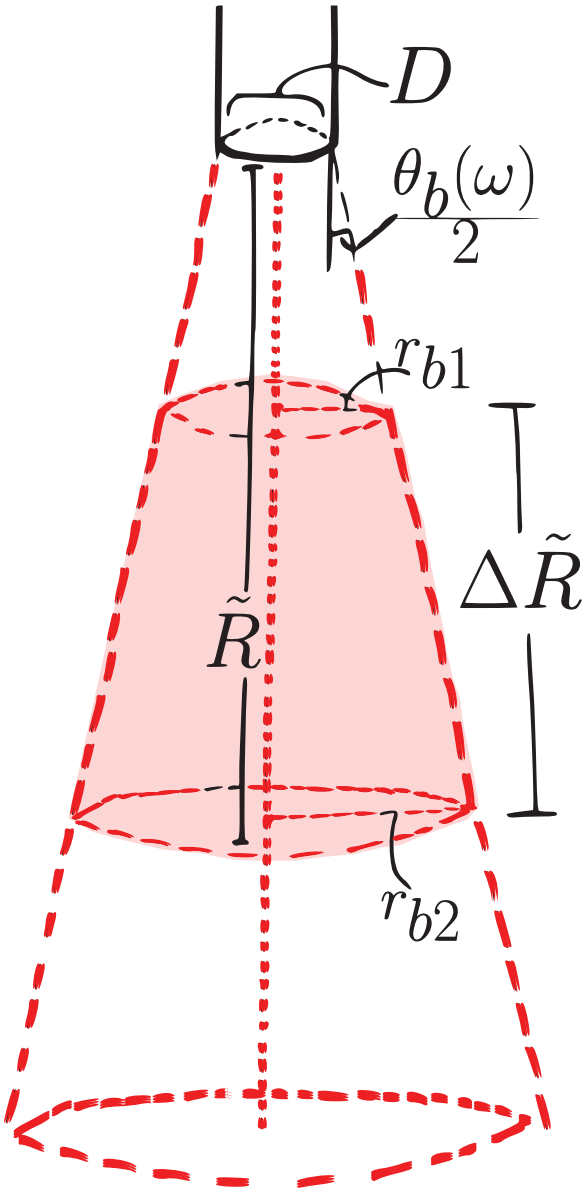

Figure 3.3: The sampling volume is calculated using Equation 3.1a as a function of the frequency-dependent beam width, θ_b, and transducer diameter, D, as well as the depth,$\tilde{R}$, and the size of the sample volume, $\Delta\tilde{R}$.

Table 3.1: The beam footprint with depth shows that the beam radius is frequency dependent and varies due to the broadband pulse. The beam radius is smallest at 150 kHz and largest at 90 kHz. The yellow entries show depths where the ice surface is partially contained within the beam, and the red entries show depths where the ice is fully contained in the beam.

Rb	r_b	
Tank Depth (m)	Beam Radius (m)	
	90 kHz	150 kHz
4	0.65	0.37
4.5	0.72	0.40
5	0.79	0.44
5.5	0.86	0.47
6	0.93	0.51
6.5	1.00	0.54

$$R_{ff} = \frac{\omega D^2}{8c} \tag{3.2}$$

where D is the diameter of the transducer face, ω is the angular frequency of the transmit pulse and c is the speed of sound in the tank (*Medwin and Clay*, 1998). The operational far-field distance of this system was 2.9 meters.

The echosounder was set to generate one millisecond acoustic pulses, 5 times per second (0.5 % duty cycle) with a peak-to-peak voltage of 290 V. Each pulse was linear frequency-modulated from 85 to 155 kHz. Acoustic backscattering was recorded by the echosounder as peak-to-peak voltage (S_{bs}) for 16.4 ms with a 500 kHz sampling frequency (f_S) and the receiver gain was set to 17 dB, 20.1 dB, 22dB or 30 dB. Each recorded ping contains 8,192 samples spanning a maximum distance of 12.9 meters.

3.1.2 Target Spheres

Backscattering was observed from an assortment of solid and hollow spheres in water and ice (see Table 3.2). Solid and hollow spheres represent the two different types of scattering expected to occur within sediment-laden ice blocks; solid spheres representing idealized sediment particles and hollow spheres representing air bubbles encased in ice.

The solid spheres were made of Tungsten Carbide (WC) (94% Tungsten Carbide, 6% Cobalt) and had a diameter of either 38.1 mm or 10 mm. The hollow spheres had a

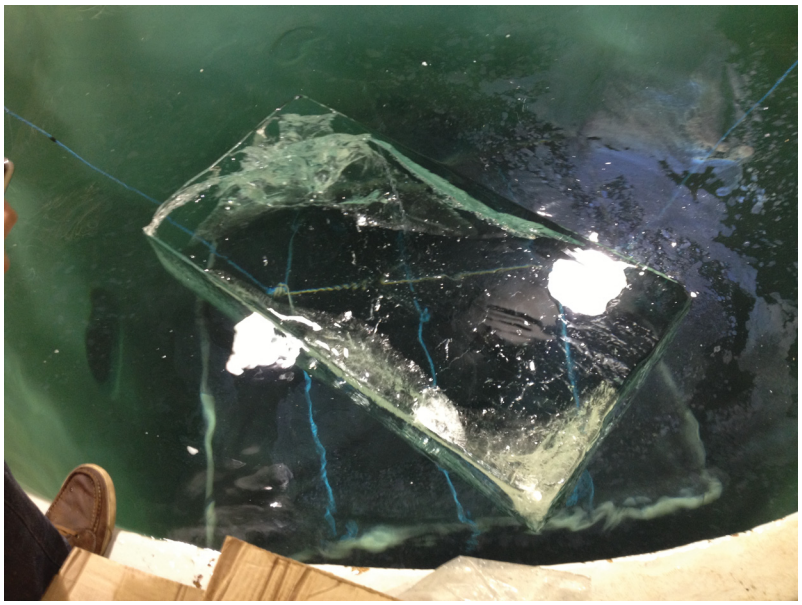

Figure 3.4: Clear (control) ice block at the surface of the tower tank. This is block BLK1 (see Table 3.2) The ice was free of air and impurities. The clear ice blocks (BLK1 and BLK5) fractured in the control runs, due to rapid expansion when introduced to the water.

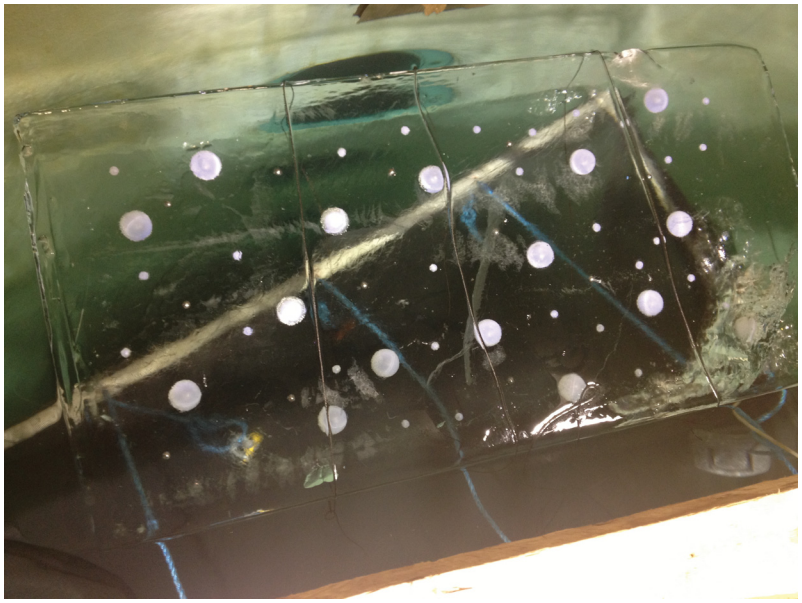

Figure 3.5: BLK3 (see Table 3.2) contains a mixture of different scattering obstacles encased in ice. Small tungsten-carbide spheres have been used to simulate sediment inclusions and polypropylene shells of different sizes have been used to simulate air cavities.

polypropylene (PP) shell filled with air. Again, two sizes were used, a 38 mm diameter sphere with a 1.2 mm thick shell and a 10 mm diameter sphere with a 1 mm thick shell. The material properties for these spherical targets are given with their uncertainty in Table 2.1. Backscattering from WC spheres are accurately described by the *Faran* (1951) or *Gaunard and Uberall* (1983) model (see Section 2.2.3), such that discrepancies between backscattering measurements and the model are attributed to problems with the calibration of the transducer (*Stanton and Chu*, 2008).

These solid and hollow spheres were encased in bubble-free ice blocks (see Figures 3.4, 3.5 and 3.6 for examples). The ice blocks were produced by Richard Chiasson of Ice Creations in Caraquet, New Brunswick by slowly freezing water in sheets and removing air and impurities with a vacuum, using a Clinebell Carving Block Ice Maker (Model: CB300X2). Air bubbles and impurities produce unwanted scattering if not removed. Each block was rectangular with dimensions of 1.00 m by 0.25 m by 0.50 m. The spheres were frozen in a plane that is roughly 12.5 cm from the largest surface of the ice block. Two inclusions free (ie. clear) ice blocks, intended as controls, and six ice blocks with various inclusions were produced (see Table 3.2).

3.1.3 Experimental Setup

The echosounder was mounted, facing downwards, at the centre of the Aquatron Tower Tank (see Figures 3.1 and 3.7), a cylindrical tank that is 10.6 m deep and 3.6 m in diameter. The tank is made from steel-reinforced concrete and is lined with Polyester sand glass-fiber with an epoxy sealant.

Using the setup sketched in Figure 3.7, backscattering was observed from individual spheres or ice blocks with spherical inclusions, that were held in the beam of the echosounder. The echosounder was pinged and multiple pings were recorded ($N_{\text{ping}} > 100$) using the echosounder setup described in Section 3.1.1, with the targets at a range of depths and with a range of receiver gain settings. Care was taken to ensure the targets were in the far-field of the beam (Equation 3.2). The smaller targets were positioned so that they were directly in the centre of the beam. The target spheres were held in a monofilament cradle and with a three point harness made of monofilament lines. These experiments are summarized in Table 3.3. Additional scattering from the nylon monofilament is assumed to be negligible (*Roberts and Jaffe*, 2008). These lines were adjusted so that the sphere moved laterally until the strongest return was located, assuming that the strongest return

Figure 3.6: A net with weights was used to oppose the buoyancy of the ice block and a camera was deployed to monitor the orientation and changes in size and shape of the ice block. BLK6 (see Table 3.2) contained a 38.1 mm tungsten carbide sphere.

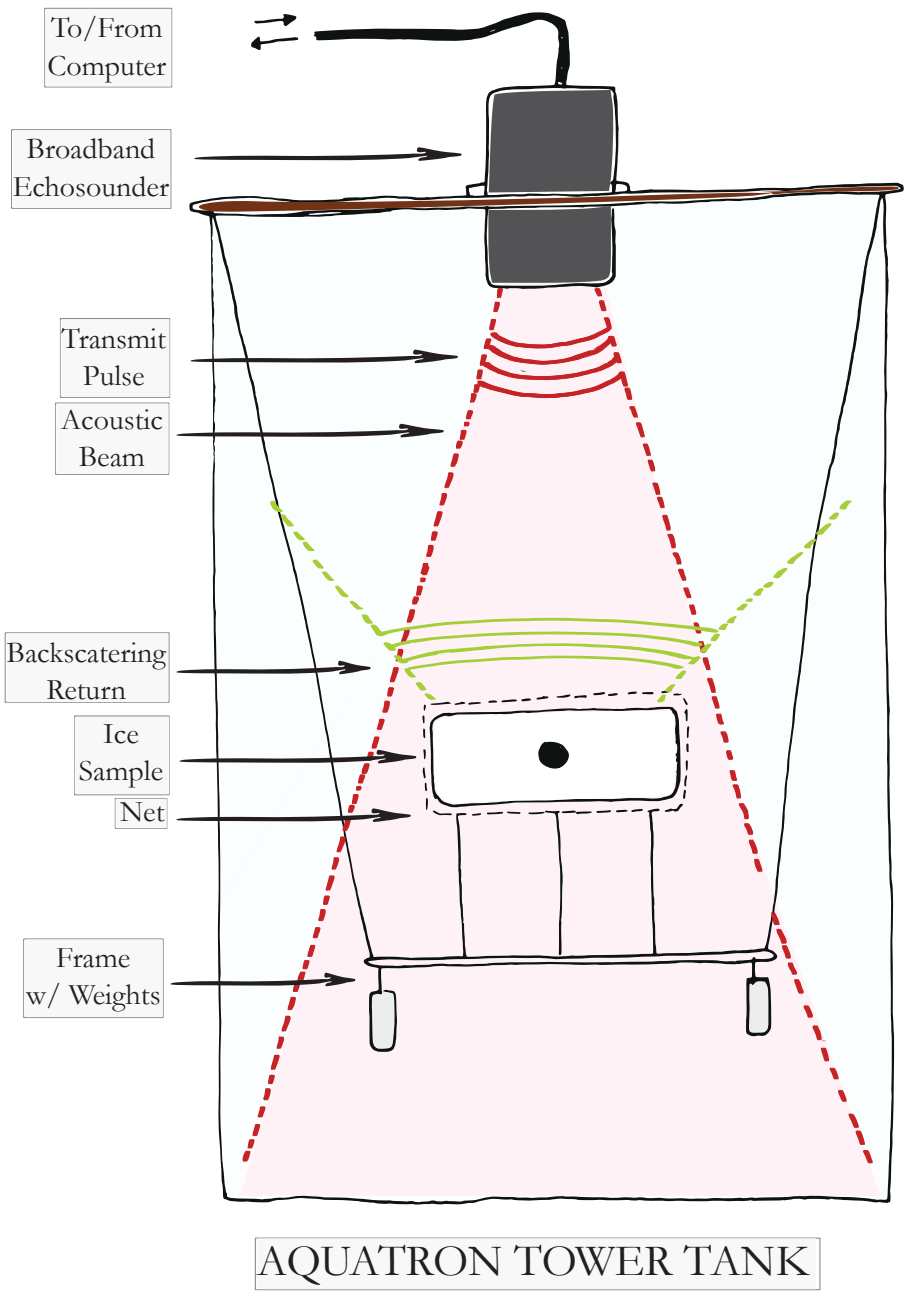

Figure 3.7: A sketch of the experimental setup in the Aquatron Tower Tank. The echosounder (SciFish 2100-B) mounted at the top transmits an acoustic pulse along a conical beam into the water. As this acoustic pulse encounters submerged objects, a fraction of the signal will scatter back to be recorded by the echosounder.

Table 3.2: Summary of Target Spheres in Water and Ice

Target ID	Date	Comments
CLB1	August 7th, 2014	38.1 mm WC sphere in water
CLB2		10 mm WC sphere in water
CLB3		38 mm hollow PP shell in water
CLB4		10 mm hollow PP shell in water
BLK1	October 22nd, 2012	Clear ice block (Control)
BLK2	October 23rd, 2012	20-10mm hollow PP shells in ice
BLK3		16-10mm WC spheres, 26-10mm hollow PP shells and 17-38mm hollow PP shells in ice
BLK4		1-38mm hollow PP shell in ice
BLK5	October 24th, 2012	Clear ice block (Control)
BLK6		1-38.1mm WC sphere in ice
BLK7		14-10mm WC spheres, 19-10mm hollow PP shells and 9 -38mm hollow PP shells in ice
BLK8	October 25th, 2012	20-10mm WC spheres in ice

occured when the target occupied the centre of the beam. Buoyant spheres (CLB 3/4 in Table 3.3) were weighed to ensure that they remained immobile during data collection.

The ice blocks with spherical inclusions were positioned in the beam of the echosounder by attaching the ice to a weighted frame. These experiments are summarized in Table 3.4. The frame was weighted with 60 lbs of lead and held the ice in a monofilament net (see Figure 3.7). The ice was held such that the beam encountered the 1/2 m x 1 m face ($A_i = 1/2$ m^2). A net, positioned beneath the block, caught the spheres that fell out as the ice melted. The lead weights held the ice down, so that it could be lowered into the far-field of the echosounder system. The setup was adjusted to make the surface of the ice as perpendicular as possible to the incident beam.

In the far-field, the beam area was large enough to fully ensonify the spherical targets, however, the relationship between the beam area and the surface of the ice blocks changed with the depth, and to a lesser degree, the orientation of the ice in the tank. Since the acoustic wavelength was much smaller than the width of the block, the beam width of

Table 3.3: Summary of Experiments: Target Spheres in Water. Backscattering from spheres [WC = solid tungsten-carbide spheres; PP = hollow (air-filled) polypropylene shells] measured with multiple pings for each experiment, at a range of depths and gain settings using a SciFish 2100-B echosounder.

Experiment ID	Gain Setting	Depth (in meters)
CLB1exp1 [38.1mm WC]	Normal Gain (22 dB)	5.1
CLB1exp2 [38.1mm WC]		7.3
CLB1exp3 [38.1mm WC]	Low Gain (17 dB)	6.2
CLB1exp4 [38.1mm WC]		8.1
CLB1exp5 [38.1mm WC]	High Gain (30 dB)	4.8
CLB2exp1 [10 mm WC]	Normal Gain(22 dB)	6.0
CLB2exp2 [10mm WC]		7.6
CLB3exp1 [38mm PP]		5.5
CLB3exp2 [38mm PP]		7.2
CLB4exp1 [10mm PP]		5.5

the scattered wave is proportional to the width of the ice surface (see Section 2.2.7). Consequently, the strength of the recorded echo from the ice surface should be relatively unaffected by diffraction, since the surface area of the block was much larger than the receiver. However, as the block melts and shrinks, the effect of diffraction becomes more pronounced since it it more likely that scattering at the edges of the block will interfere with the main echo. Therefore, changes in the position and orientation of the block become important. However, this should not be an issue until the surface dimensions of the block are comparable with the size of the receiver.

Since it was difficult to securely hold the block in place without introducing unwanted scattering from rigid frames, a camera was lowered into the tank to photograph the melting ice block, so that the changing shape and orientation of the ice could be observed. The echosounder was also mounted at at 6° and 10° angles to observe the dependence of backscattering from the ice block as a function of incidence angle (Table 3.4).

3.2 Data Processing

Backscattering data recorded by the echosounder were stored as a time series of peak-to-peak voltage (S_{bs}), which is proportional to pressure fluctuations at the receiver. This time

Table 3.4: Summary of Experiments: Target Spheres in Ice. Backscattering from spheres encased in ice, measured with multiple pings for each experiment, at a range of depths and incidence angles using a SciFish 2100-B echosounder. See Table 3.2 for description of targets in each block.

Experiment ID	Time Submerged (minutes)	Incidence Angle (degrees)	Approx. Depth (meters)	Notes
BLK4exp1	2	0	5.3	This ice block is
BLK4exp2	12	0	5.3	slightly tilted.
BLK4exp3	14	0	5.3	
BLK4exp4	23	10	5.3	
BLK4exp5	38	6	5.3	
BLK4exp6	62	0	5.3	
BLK5exp1	5	0	4.8	This ice block
BLK5exp2	21	6	4.8	is extensively
BLK5exp3	39	10	4.8	fractured.
BLK5exp4	55	0	4.8	
BLK5exp5	65	6	4.8	
BLK5exp6	73	10	4.8	
BLK5exp7	105	0	4.8	
BLK6exp1	3	0	4.5	
BLK6exp2	15	0	4.5	
BLK6exp3	26	6	4.5	
BLK6exp4	35	10	4.5	Ice cracked around the
BLK6exp5	45	0	4.5	sphere.
BLK6exp6	58	6	4.5	
BLK7exp1	6	0	5.1	This ice block is sharply
BLK7exp2	15	0	5.1	tilted and fractured at
BLK7exp3	31	5	5.1	the edges.
BLK7exp4	55	0	5.1	
BLK8exp1	6	0	6.2	Moved this block during
BLK8exp2	17	0	6.2	the experiment.
BLK8exp3	45	0	5.4	
BLK8exp4	46	0	5.4	

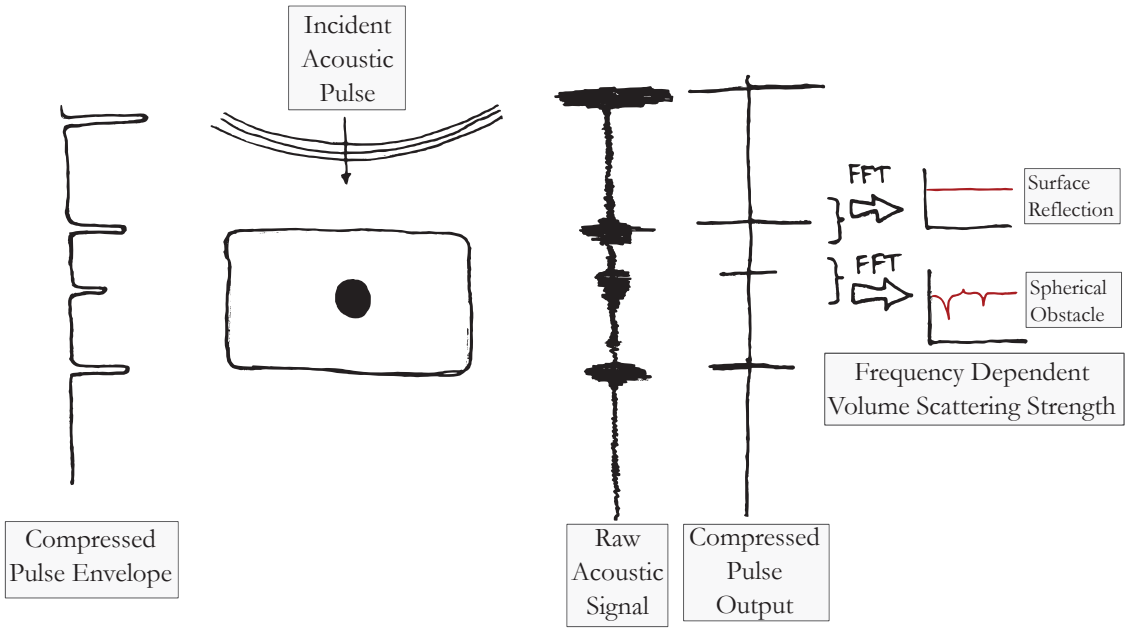

Figure 3.8: Acoustic backscatter is expected to originate from the surface of submerged ice and from inclusions within the ice. The raw acoustic data can be transformed into a compressed pulse output to help differentiate discrete returns. A Fourier transform is then applied to the compressed pulse data to generate observations of frequency dependent acoustic backscatter.

series was used to calculate the frequency-dependent target strength ($TS_{obs}(\omega)$) which was compared to the scattering models from Chapter 2. Figure 3.8 sketches the steps involved in extracting $TS_{obs}(\omega)$ from the raw acoustic backscatter measurements, discussed in detail in the following subsections.

3.2.1 Pulse Compression

Pulse compression was applied to the backscattering time series to simultaneously increase the signal-to-noise ratio and the spatial resolution of the signal (*Stanton et al.*, 1998). Without pulse compression, distinct returns would need to be separated by a distance of at least half the pulse length to avoid overlap. Thus, without pulse compression the spatial resolution can only be increased by decreasing the pulse length. However, the energy in the pulse, hence the signal-to-noise ratio, is proportional to the pulse length; therefore, a long pulse is needed to overcome noise (*Stanton et al.*, 1998). Pulse compression correlates a linear frequency modulated transmit pulse with the resultant echo. The correlation transforms echoes from a uniform-amplitude pulse with a duration of t_{pulse}, to a cardinal sine with a duration of approximately $t_{cp} = 1/\beta$ (*Klauder et al.*, 1960), where β is the

bandwidth of the pulse. In this case, β = 70 kHz. The spatial resolution of the compressed pulse output is $c/2\beta$ (*Stanton et al.*, 1998). As the name suggests, the energy in the return is not reduced by pulse compression, instead, it is compressed toward the centre of the pulse. This provides a selective, virtual gain to true echoes, proportional to βt_{pulse} (*Klauder et al.*, 1960). Pulse compression increased the spatial resolution of our system from 70 cm to 1 cm and amplified the returns by 70.

The compressed pulse output, $CP(t)$, is the scaled cross correlation of the broadband transmit pulse, S_{tr}, and and the backscattering time series, S_{bs} (*Chu and Stanton*, 1998).

$$CP(t) = \kappa_c(S_{tr} \otimes S_{bs}) \tag{3.3}$$

where κ_c is a proportionality constant related to the autocorrelation of the transmit pulse and $\otimes$ is the cross correlation (*Stanton et al.*, 1998). The cross correlation will remove background noise, since it is not correlated with the transmit pulse (*Stanton et al.*, 1998). A transmit pulse was not recorded in the tank, instead, a clipped transmit pulse appears in the first 500 samples (for a 1 ms transmit pulse) of each backscattering data file, and was used as S_{tr} (see *Ross et al.* (2013) for consequences of using a clipped transmit signal).

The envelope of the CP output is used to locate scattering sources and is corrected for spherical spreading by multiplying the CP output by R^2 (*Simmonds and MacLennan*, 2005). Peaks in the envelope of the CP output indicated returns most likely caused by distinct scattering sources. Peaks in the CP envelope may also indicate multiple reflections or partial-wave arrivals from a single target (*Stanton and Chu*, 2008).

3.2.2 Frequency Dependent Target Strength

Once a return was located, the sample volume is centred at the corresponding peak ($\tilde{R}$) in the CP output and a Discrete Time Fourier Transform was applied,

$$\hat{S}_{bs}(\tilde{\omega}) = \sum_{N=N_{\tilde{R}}-\frac{N_{\text{fft}}}{2}}^{N_{\tilde{R}}+\frac{N_{\text{fft}}}{2}} CP(N/f_s)e^{-i\omega\ N/f_s} \tag{3.4}$$

where, N_{fft} is the size of the Fourier transform window, N denotes sample numbers (starting at 0 at the beginning of the transmitted pulse) and $N_{\tilde{R}}$ is the sample number corresponding to the peak in the CP output, f_s is the sampling frequency ($f_s = 500kHz$), and $CP(N/f_s)$ is the compressed pulse (see Equation 3.3) and $N_{\tilde{R}} = 2f_s\tilde{R}/c$. The length

of the sample volume, $\Delta\tilde{R}$, (see Section 3.1.1) is set by the Fourier transform window, where $\Delta\tilde{R} = N_{\text{fft}}c/2f_s$. The depth vector, thus the length of the sample volume, depends on the local soundspeed and changes from water to ice. Table 3.5 shows that windows with $N_{\text{fft}} > 64$ cannot be used to isolate inclusions from the ice surfaces that were, at most, 25 cm apart.

$\hat{S}_{bs}(\tilde{\omega})$ is the backscattering spectra resolved at a set of discrete frequencies, $\tilde{\omega}$. The sampling frequency and number of samples contained in the Fourier transform window determines the spectral resolution, ω_{res}, which is also the lowest frequency resolvable by the Fourier transform, where $\omega_{res} = f_s/N_{\text{fft}}$. The Nyquist frequency, the maximum resolvable frequency of this system, is $f_s/2$ = 250 kHz. Backscattering spectra were plotted across a 60 kHz band, centred at 120 kHz (90 kHz to 150 kHz), where the echosounder system is most reliable (*Ross et al.*, 2013).

Table 3.5: Fourier Transform Window Height in Water and Ice. The number of samples used to calculate the FFT window (N_{fft}) gives a different spatial resolution (ΔR) in water and ice. The maximum spectral resolution (ω_{res}) is also a function of the size of the FFT window.

N_{fft}	ΔR in water (cm)	ΔR in ice (cm)	ω_{res} (kHz)
8	1.2	3.1	62.50
16	2.4	6.2	31.25
32	4.8	12.5	15.63
48	7.2	18.7	10.42
56	8.4	21.8	8.93
64	9.6	25.0	7.81
128	19.2	49.9	3.91
256	38.5	99.8	1.95
512	76.9	199.7	0.98

The backscattering spectra are used to calculate the frequency dependent target strength, TS, which is the magnitude of backscattering within a given sample volume, $V_b(\omega)$, normalized by the incident energy.

The target strength equation (Equation 3.5) was adapted from the SONAR equations (*Medwin and Clay*, 1998), i.e. $TS = EL + 2TL - SL$ where TS is the target strength of a single scatterer. The echo level, EL, is accounted for by removing the receiver gain from the magnitude of the backscatter spectra. The source level, SL, is the transmit voltage

with frequency dependent calibration adjustments. Transmission loss, TL, accounts for as spherical spreading ($20 \log R$) and attenuation (αR). Thus, the target strength equation is

$$\begin{aligned} TS_{obs}(\tilde{\omega}) = 20 \log_{10} |\hat{S}_{bs}(\tilde{\omega})| - \text{GAIN} \qquad & [\text{ Echo Level}] \\ -20 \log_{10} V_{pp} + K(\omega) \qquad & [\text{ Source Level}] \\ +40 \log_{10} \tilde{R} + 2\, \alpha(\omega) \tilde{R} \qquad & [\text{ Transmission Loss}]. \end{aligned} \tag{3.5}$$

The calibration constant, $K(\omega)$, is the difference between backscattering from a single tungsten carbide sphere measured by the echosounder system ($TS_{clb}(\omega)$) with an accurate scattering model ($[TS(\omega)]^{fs}$), for example, the *Gaunard and Uberall* (1983) model (*Stanton and Chu*, 2008), where

$$K(\omega) = [TS(\omega)]^{fS} - TS_{clb}(\omega). \tag{3.6}$$

Models from Chapter 2 predict TS_{mod} (see Equations 2.39 to 2.41c) are compared with observed target strength, TS_{obs} (see Equation 3.5) using

$$\epsilon = |TS_{mod} - TS_{obs}| \tag{3.7}$$

where, ϵ is useful for comparing the validity of the models across different measurements.

CHAPTER 4

RESULTS

4.1 Echosounder Calibration

The echosounder was calibrated using tungsten carbide spheres. The calibration curve ($K(\omega)$) was calculated from the difference between the observed and predicted target strength (TS) from a 38.1 mm diameter sphere, shown in Figure 4.1, following Equation 3.2.2. A 512-point Gaussian window, centred at the peak in the compressed pulse (CP) envelope was used, resulting in a 980 Hz resolution TS spectrum that shows well defined resonances. The observed frequency dependence matches the *Gaunard and Uberall* (1983) model (Equation 2.41a) in the vicinity of the resonance at 135 kHz, parameterized using a compressional WC soundspeed of 7286 m/s and a shear soundspeed of 4154 m/s, and water soundspeed of 1502 m/s. The possible variation in elastic parameters of the sphere and surrounding medium, given in Table 2.1, lead to uncertainty in the model (shown as a pink patch in Figure 4.1). Note that the calibration curves depend upon spectral resolution (Figure 4.2); windows smaller than 128 points deviate from the better resolved $K(\omega)$s. Thus, for windows smaller than 128 points a constant $K = 28.75$ dB was used. While this does not capture the frequency dependence of the transducer sensitivity, it affords better estimations of the echo amplitude.

Multiple backscattering observations from large and small WC spheres, shown in Figure 4.3, were independent of receiver gain and range to the target. The error bars in Figure 4.3 represent the average frequency dependent variance from all pings for each experiment. Calibration curves obtained from the two sizes of spheres do not agree perfectly, likely as a result of lower signal-to-noise ratio (SNR) in the returns from the small spheres. Thus, the $K(\omega)$ obtained from the 38.1 mm WC sphere were used in the following analysis.

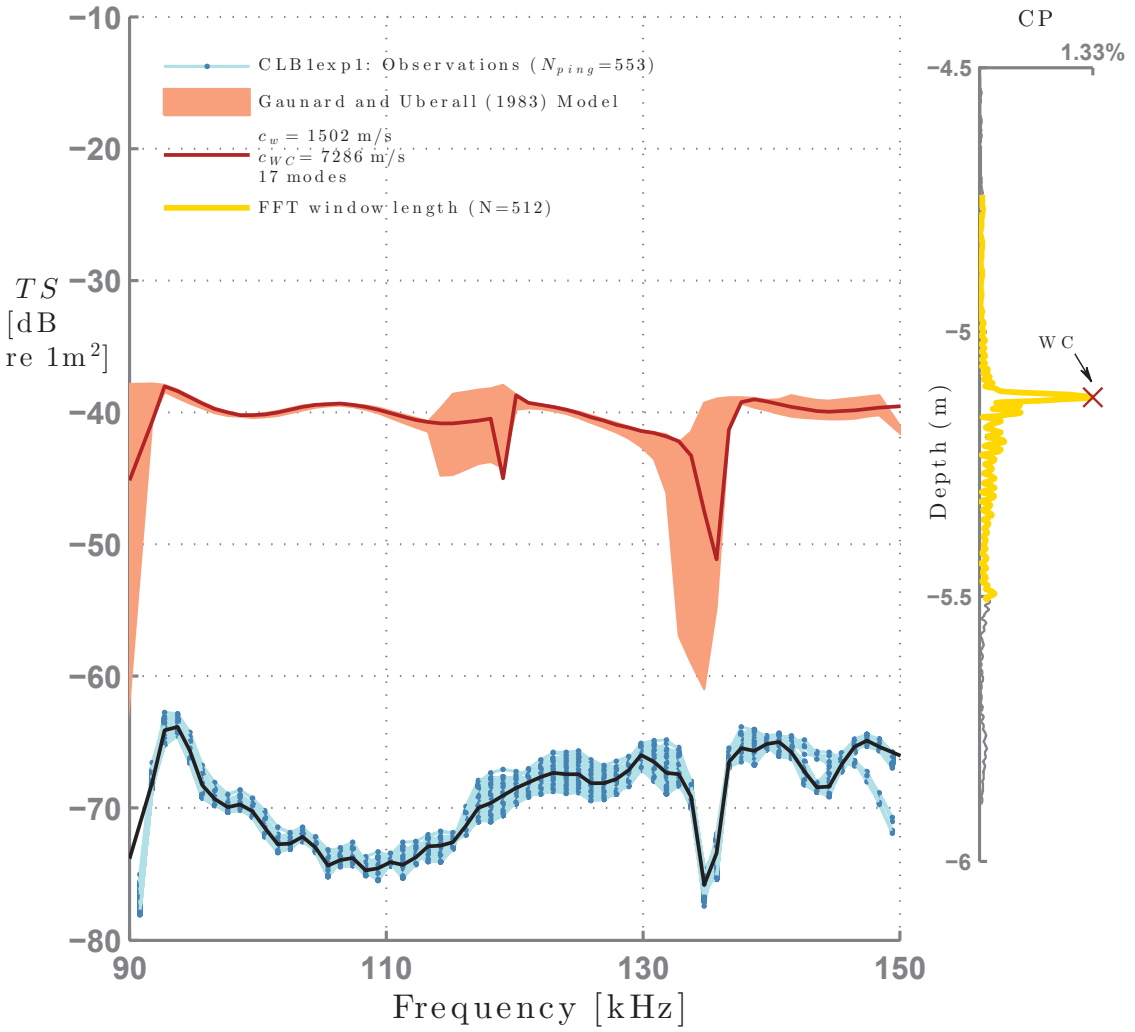

Figure 4.1: Left panel: Mean uncalibrated target strength from a 38.1 mm diameter WC sphere [CLB1exp1] (solid black line), calculated with a 980 Hz resolution from an ensemble of pings (shown in blue), and the *Gaunard and Uberall* (1983) model (shown with its uncertainty in red). Right panel: The CP envelope shows the average strength of the return, calculated from an ensemble of pings, relative to the transmit pulse. The main peak in the CP envelope (red x), shows the depth of the sphere (WC), and the size of the FFT window is indicated in gold.

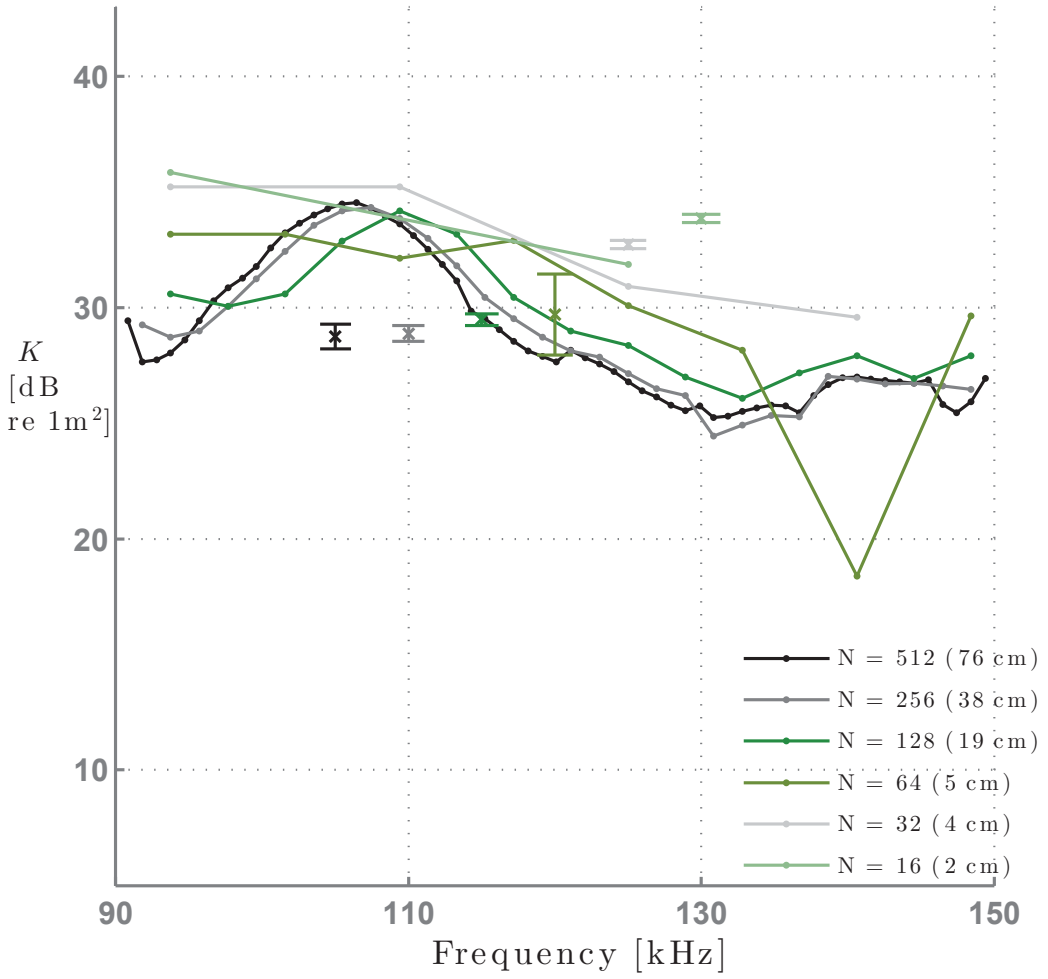

Figure 4.2: $K(\omega)$ as a function of the size of the FFT window (N) calculated from CLB1exp1 (38.1 mm WC sphere). The dots indicate the discrete frequencies resolved by the Discrete Fourier Transform. Error bars represent the average variance in the calibrations and are centred at the mean K .

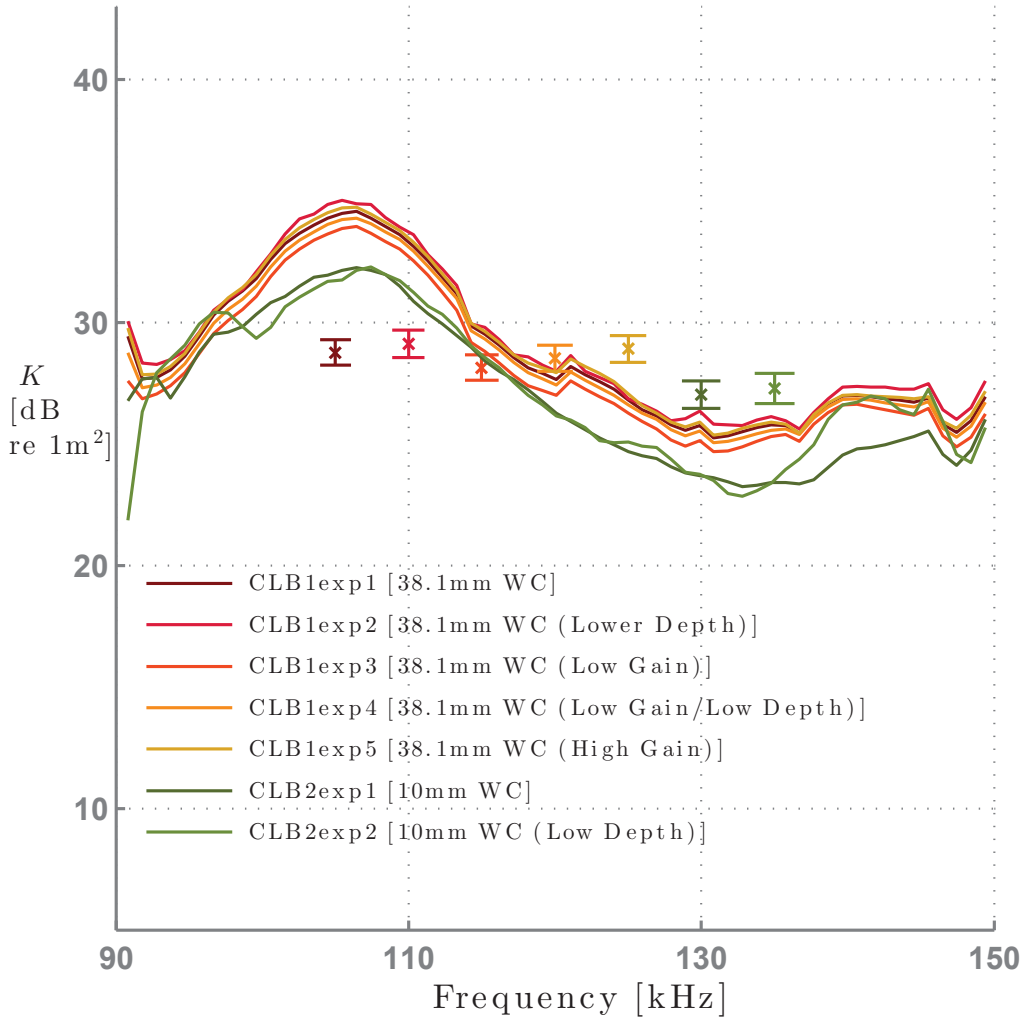

Figure 4.3: $K(\omega)$ with a 980 Hz resolution determined from different observations from 38.1 mm diameter WC spheres, in red and orange solid lines, and 10 mm diameter WC spheres in green solid lines. Error bars represent the mean variance and are centred at the mean K for each experiment.

4.2 Observations of Target Spheres in Water

4.2.1 Tungsten Carbide

Observed target strength, TS, calculated using Equation 3.5, for large solid spheres agrees well with modelled TS, shown in Figure 4.4. The model accurately predicts strong resonance at 91 kHz and slightly over-predicts the strength of the resonance at 135 kHz. The data do not show the resonance predicted at 119 kHz. The model-measurement mismatch, defined by Equation 3.7, is shown in Figure 4.5 for independent measurements from large solid spheres. These observations from a 38.1 mm diameter WC sphere have a mean absolute mismatch of 1 dB (Table 4.1). The *Gaunard and Uberall* (1983) model, calculated using ${A_n}^{Fs}(\omega)$ in Equation 2.41a, consistently underestimated the observed TS from 10 mm diameter solid WC spheres in water, shown in Figure 4.6. Noise appears in the compressed pulse (right panel of Figure 4.6) as small, diffuse peaks before the large peak associated with the sphere. The mean absolute mismatch from 10 mm diameter WC spheres is 1.9 dB (Table 4.1).

4.2.2 Hollow Polypropylene

Observations from 38 mm diameter PP shells, shown in Figure 4.7 are similar to the *Anderson* (1950) model, for an air bubble without a shell, using soundspeeds of 1502 m/s and 321 m/s, for water and air, respectively. Two distinct peaks appear in the CP envelope (right panel of Figure 4.7) and were attributed to reflections from the top and bottom of the PP shell (PPt and PPb, respectively) approximately 3 cm apart . The *Gaunard and Werby* (1987) model explicitly considered air encased in a PP shell, using a compressional PP soundspeed of 2097 m/s and a shear PP soundspeed of 748 m/s. This model, characterized by multiple strong resonances, varies significantly over the plausible range of shell properties (Figure 4.7). The observations were consistently overestimated by the *Gaunard and Werby* (1987) model and did not show the resonances evident in the model. Similar mismatch for 10 mm diameter PP shells (Figure 4.8), reinforce that the *Anderson* (1950) model is more appropriate for these targets. Note that the observations do not agree with either model at low frequencies. The mean absolute mismatch between the *Anderson* (1950) model and observations is 1.2 dB for 38 mm PP shells and 2.1 dB for 10 mm PP shells (Table 4.1). The mean absolute mismatch between the *Gaunard and Werby* (1987) model and observations is 7.3 dB for 38 mm PP shells and 4.9 dB for 10 mm

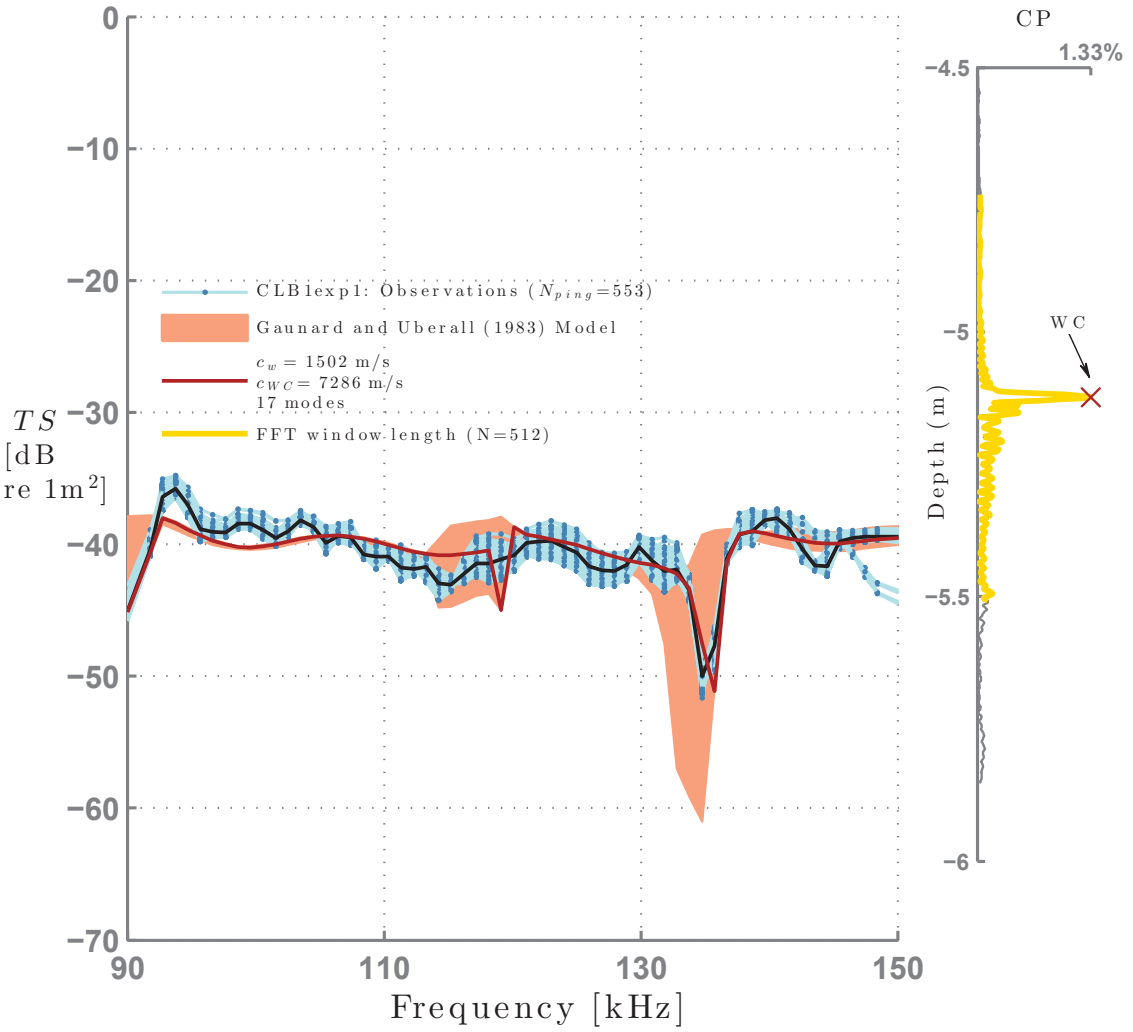

Figure 4.4: Left panel: Mean target strength from a 38.1 mm diameter WC sphere [CLB1exp1] (solid black line), calculated with a 980 Hz resolution from an ensemble of pings (shown in blue), and the *Gaunard and Uberall* (1983) model (shown with its uncertainty in red). Right panel: The CP envelope shows the average strength of the return, calculated from an ensemble of pings, relative to the transmit pulse, where the main peak in the CP envelope (red x) shows the depth of the sphere (WC), and the size of the FFT window, is indicated in gold.

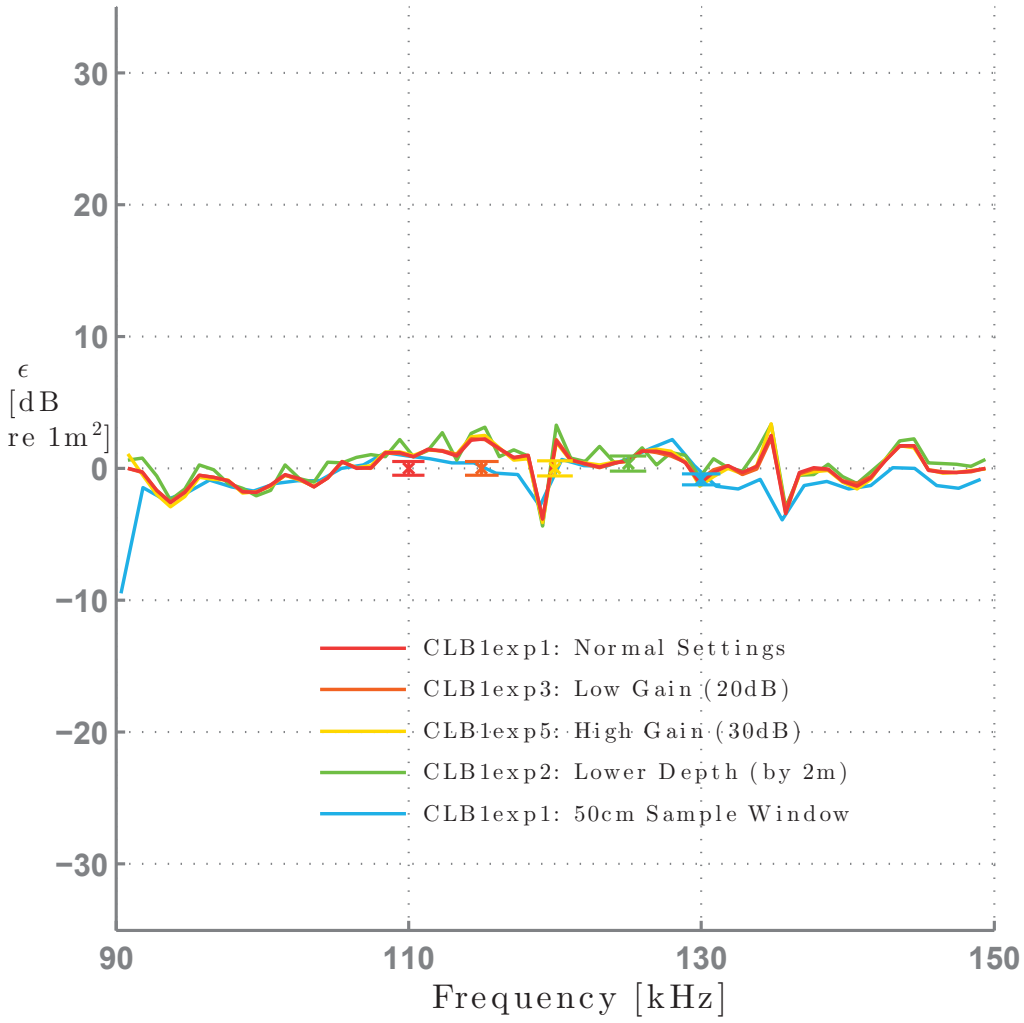

Figure 4.5: Model-measurement mismatch, ϵ, from 38.1 mm WC spheres in water with a 980 Hz resolution. The mismatch is calculated from mean TS as solid lines. Error bars represent the ping to ping variance in the TS, centred at the mean ϵ for each experiment.

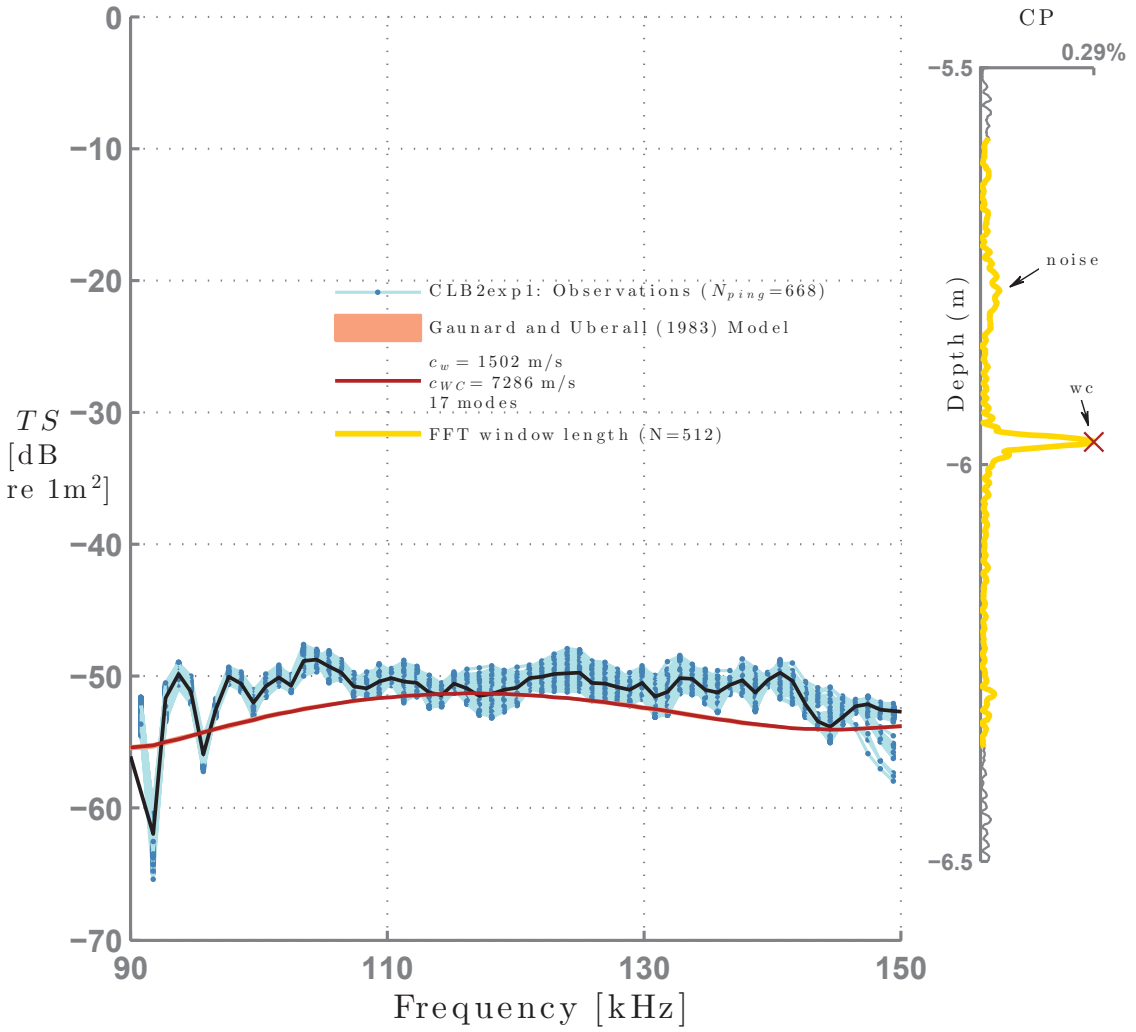

Figure 4.6: Left panel: Mean target strength from a 10 mm diameter WC sphere [CLB2exp1] (solid black line), calculated with a 980 Hz resolution from an ensemble of pings (shown in blue), and the *Gaunard and Uberall* (1983) model (shown with its uncertainty in red). Right panel: The CP envelope shows the average strength of the return, calculated from an ensemble of pings, relative to the transmit pulse, where the main peak in the CP envelope (red x) shows the depth of the sphere (wc), and the size of the FFT window, is indicated in gold.

PP shells (Table 4.1). Mean TS from small hollow spheres is similar to mean TS from small solid spheres (Figure 4.9), and TS from large solid and hollow spheres only differed due to the strong resonance at 135 kHz, seen in the TS observed from the WC spheres, but not the PP shells.

4.3 Target Spheres in Ice

4.3.1 Single Large Sphere

The returns from the target spheres were difficult to locate in ice due to the ice surface reflection (ISt), seen in the CP envelope of Figure 4.10 (right panel). Note that the small peaks between reflections from the top (ISt) and bottom (ISb) surfaces of the ice block are approximately 5 times larger than the return from the WC sphere in water. The magnitude of the CP envelope within the ice (Figure 4.10, right panel at 4.6 meters) suggests that reverberation from the ice block surfaces was stronger than the backscattering from the large WC sphere, since a distinct peak that could be attributed to the sphere was not observed. As a result, the observed TS will be a combination of the return from the sphere and reverberation from the ice surface. Since the exact location of the target spheres was not monitored through the experiments (though it was known to be 12.5 cm from either surface at the start), the best approximation was to centre a 32-point window at the peak closest to the initial location of the spheres, 12.5 cm from the ice surface. The window covers 12.5 cm in ice, so that as the ice melted, the sphere should be contained in this window. The smaller window, which helps to isolate the echo from the sphere from ice surface reverberation, has a spectral resolution of 16 kHz and only contained a portion of the echo expected from the target sphere. I account for the decreased frequency resolution by calculating the *Flax and Uberall* (1980) model, using only the first two modes (using Equation 2.37, summing until $n = 2$). The higher order modes that are used to resolve interference effects due to multiple wave arrivals can be ignored since the tail of the echo was not contained in the 32-point window. However, even with this correction, the model underestimated the observed TS from the large WC sphere (Figure 4.10). The model did not describe reverberation from the ice surface; thus, as the block melted and the ice surfaces moved closer to the sphere, both the magnitude of the mismatch and the observed mid-block TS increased. The models underestimated TS from large WC inclusions under all experimental conditions, as seen in Figure 4.11, with a mean absolute mismatch from a

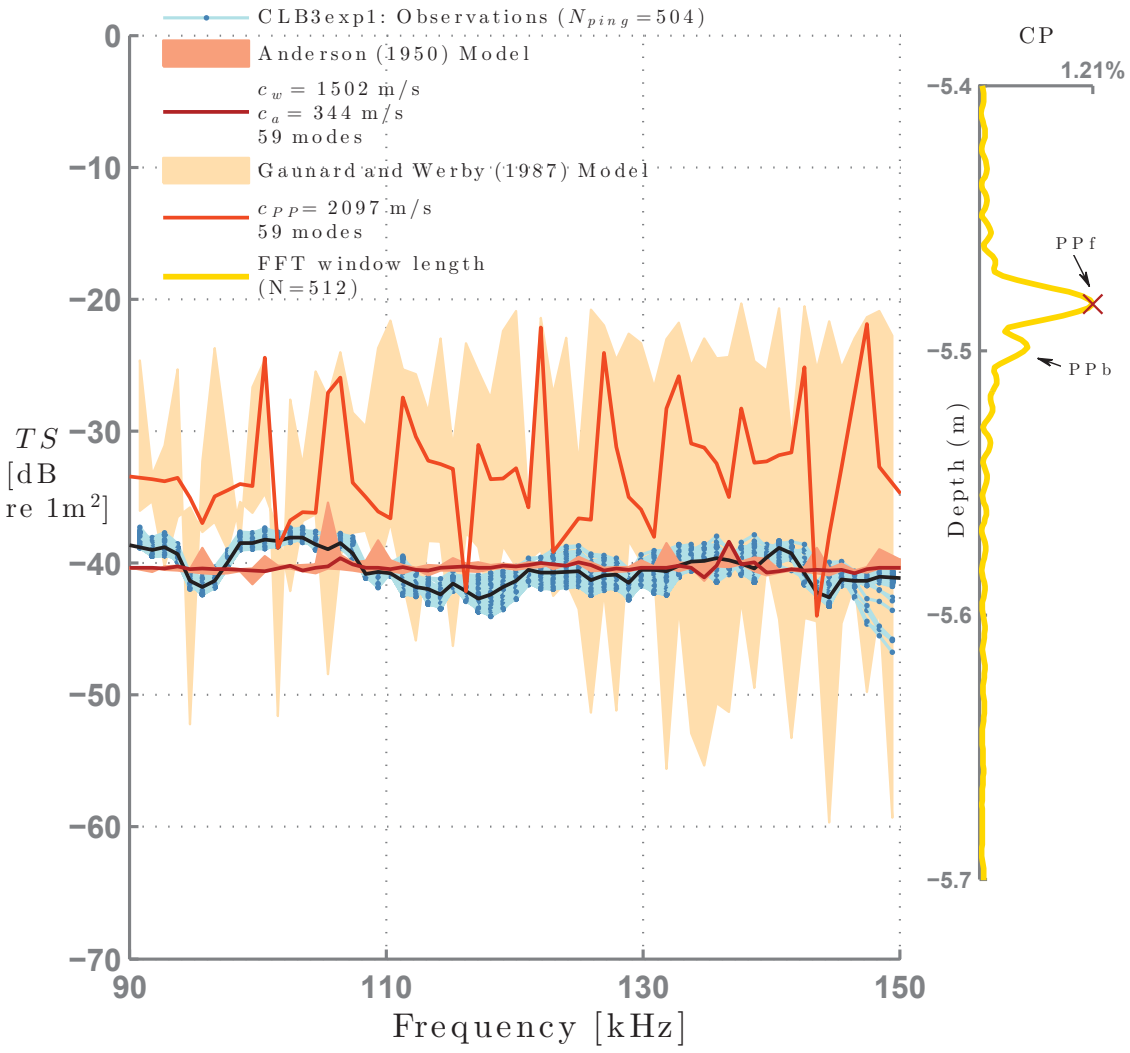

Figure 4.7: Left panel: Mean target strength from a 38 mm diameter air-filled PP shell in water [CLB3exp1] (solid black line), calculated with a 980 Hz resolution from an ensemble of pings (shown in blue), and the *Gaunard and Werby* (1987) and *Anderson* (1950) models (shown with their respective uncertainties in orange and red). Right panel: The CP envelope shows the average strength of the return, calculated from an ensemble of pings, relative to the transmit pulse, where the main peak in the CP envelope (red x) shows the depth of the sphere (PPt), followed by a reflection from the bottom of the sphere (PPb) and and the size of the FFT window, is indicated in gold.

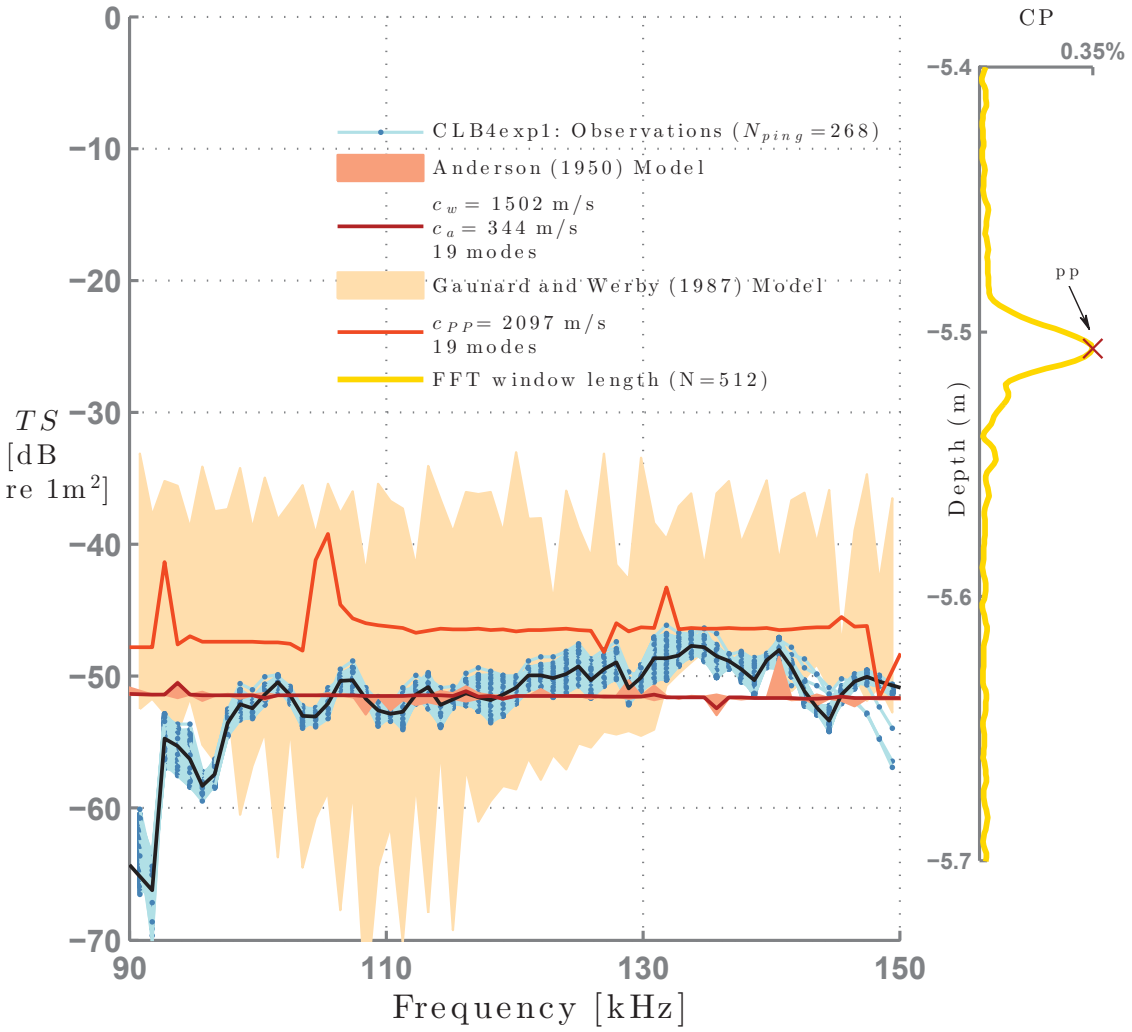

Figure 4.8: Left panel: Mean target strength from a 10 mm diameter air-filled PP shell in water [CLB4exp1] (solid black line), calculated with a 980 Hz resolution from an ensemble of pings (shown in blue), and the *Gaunard and Werby* (1987) and *Anderson* (1950) models (shown with their respective uncertainties in orange and red). Right panel: The CP envelope shows the average strength of the return, calculated from an ensemble of pings, relative to the transmit pulse, where the main peak in the CP envelope (red x) shows the depth of the sphere (pp), and the size of the FFT window, is shown in gold.

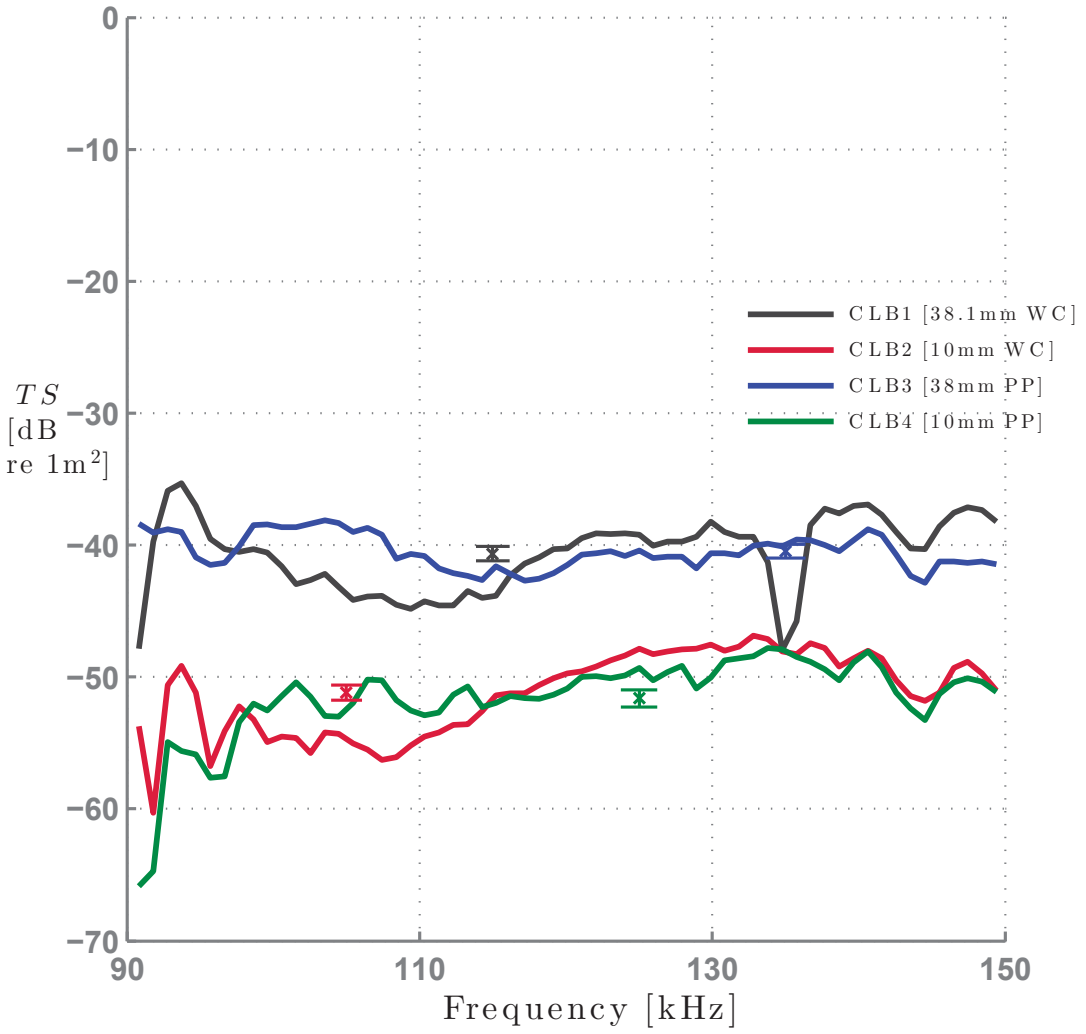

Figure 4.9: Observed TS from 38.1 mm and 10 mm diameter WC spheres and 38 mm and 10 mm diameter air-filled polypropylene shells. Mean TS is calculated with a 980 Hz resolution averaged over all experiments (Table 3.3). Error bars represent the variance across experiments in the TS, centred at the mean TS.

38.1 mm WC sphere in ice of 14.1 dB, averaged over all experiments (Table 4.1).

Compared to the large WC sphere, the mean observed mid block TS for large air cavities in ice has a smaller model-measurement mismatch, but still does not agree with the *Gaunard and Uberall* (1978) model predictions (Figure 4.12) . The reverberation was weaker than during the WC sphere experiment, where the observations from BLK4 were characterized by larger ping to ping variability. The ice surface reflection, at 5.31 m, in Figure 4.12 (right panel) compared with 4.49 m in Figure 4.10, was much weaker; 13 % vs. 51%. There was consequently weaker surface reverberation, but the echo from the inclusion was still not clear in the CP envelope (Figure 4.12, right panel). The mean absolute model-measurement mismatch from 38 mm PP shells in ice was 9.0 dB (Table 4.1).

Echoes from solid spheres, expected to have similar mean TS in water and ice, appeared stronger in ice (Figure 4.13), however scattering from the spheres in ice could not be unambiguously detected. Note that for the spheres in water, a 32-point window and frequency independent calibration was used producing a TS where resonances from the sphere in water are no longer resolved, compared with Figure 4.9.

4.3.2 Scattering from the Ice Surface

When the surface reflection from inclusion-free ice was windowed using a 32-point window, shown in Figure 4.14, the *Langleben* (1970) model, calculated using Equation 2.39, significantly overestimated TS. Note that the CP envelope (Figure 4.14, right panel) does not contain a strong surface reflection for the fractured block. Surface reflections from ice blocks with minimal fracturing were stronger and were generally underestimated by the reflection model (Figure 4.15 and 4.16) .

The observed TS from the surface reflections varied significantly between different experiments (Figure 4.16). Observations of surface scattering from blocks with fractures deviated the most from the *Langleben* (1970) model. Only one non-fractured block agreed with the modelled TS, and the others had a similar frequency dependence with a mean absolute mismatch of 7.2 dB, averaged over all experiments. Conversely, ice blocks with fractured surfaces did not agree with the *Langleben* (1970) model, with a mean absolute mismatch of 16.4 dB.

Observations isolated from the bottom surface show reasonable agreement with the surface reflection model, adjusted for transmission through the surface of the ice calculated

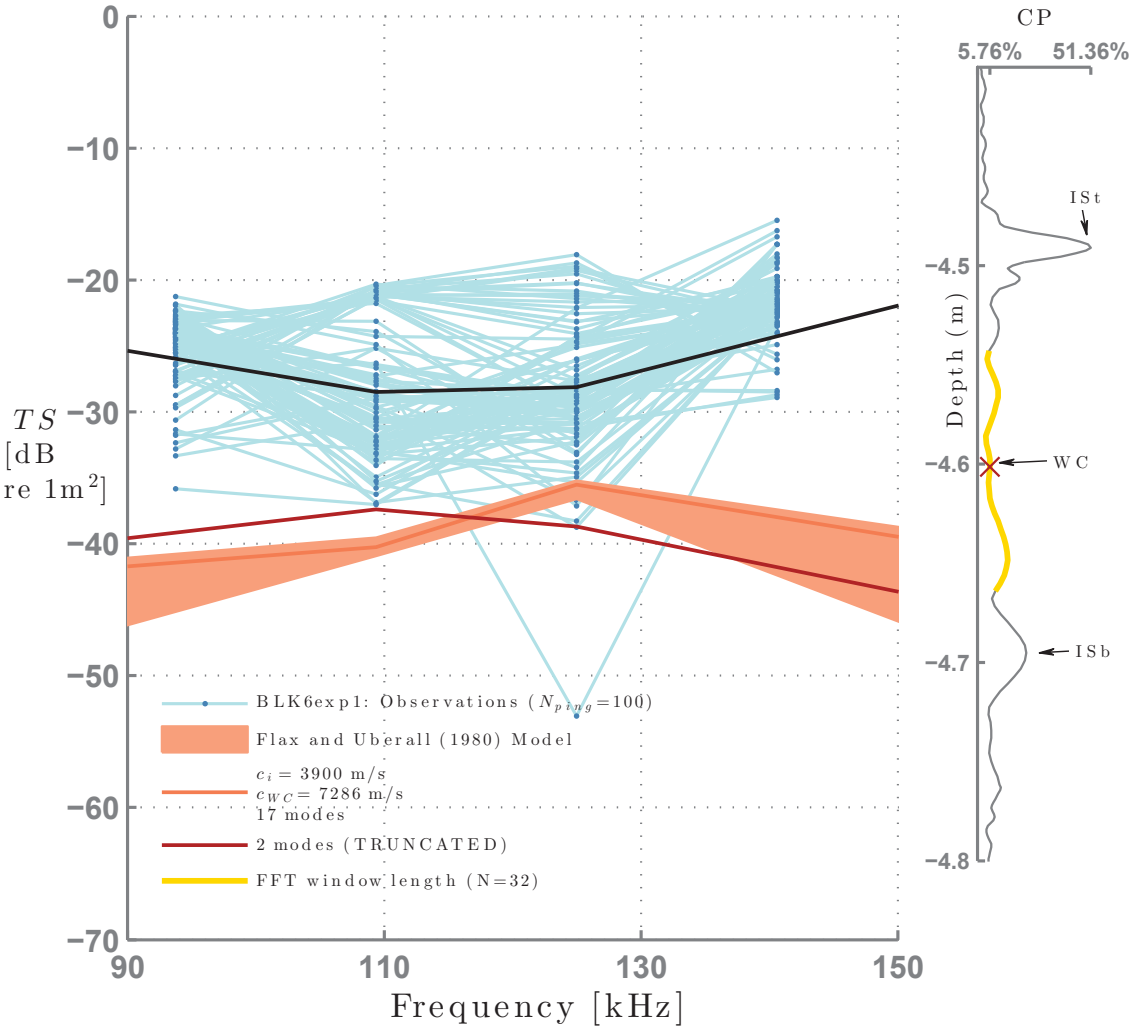

Figure 4.10: Left panel: Mean target strength from a 38.1 mm diameter WC sphere in ice [BLK6exp1] (solid black line), calculated with a 16 kHz resolution from an ensemble of pings (shown in blue) and the *Flax and Uberall* (1980) model (shown with its uncertainty in red). The dark red solid line shows a truncated manifestation of this model, to compare with low-resolution observations. Right panel: The CP envelope shows the average strength of the return, calculated from an ensemble of pings, relative to the transmit pulse, where the main peak in the CP envelope (red x) shows the assumed depth of the sphere (WC), and the size of the FFT window, is indicated in gold. The surface of the ice (ISt) produces a strong reflection, followed by a reflection from the bottom surface (ISb).

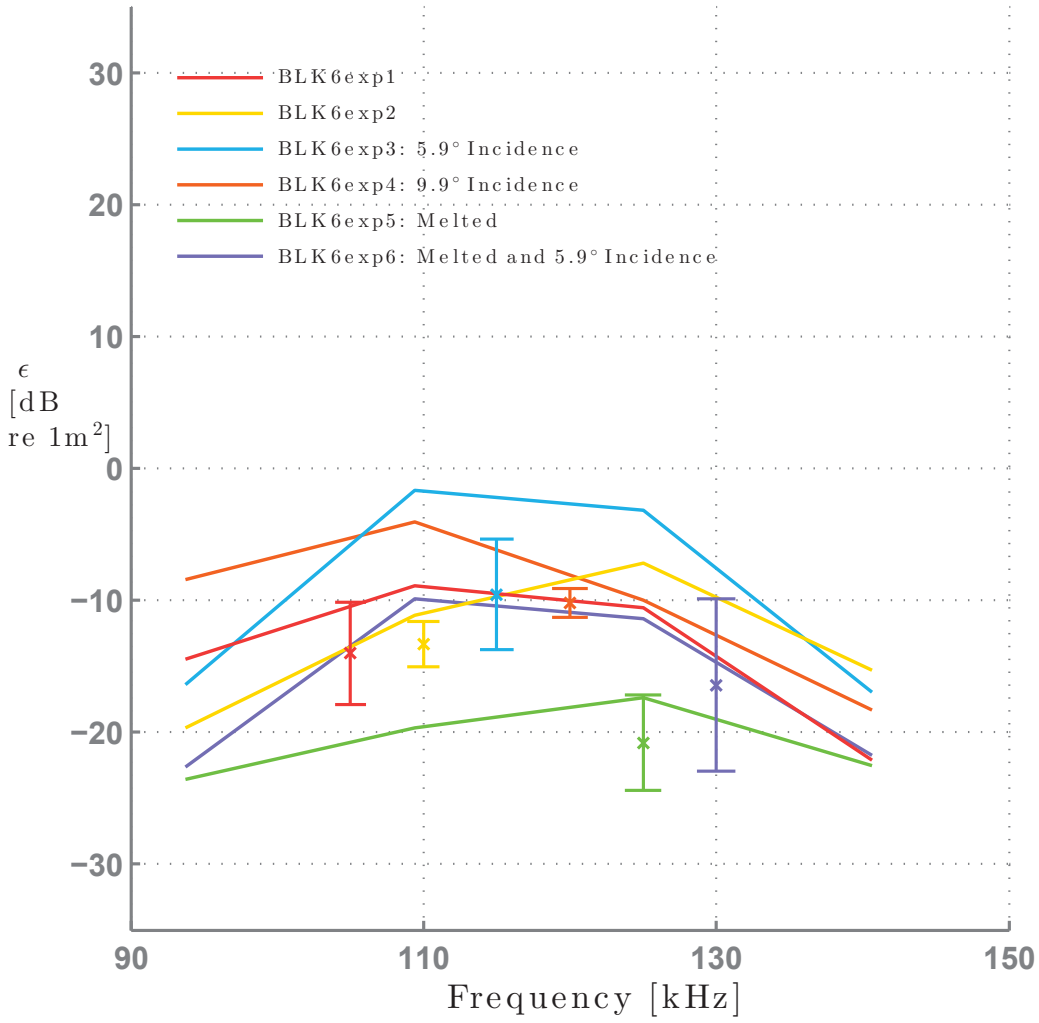

Figure 4.11: Model-measurement mismatch, ϵ, from a 38.1 mm WC sphere in ice with a 16 kHz resolution. The mismatch is calculated from mean TS. Error bars represent the ping to ping variance in the TS, centred at the mean ϵ.

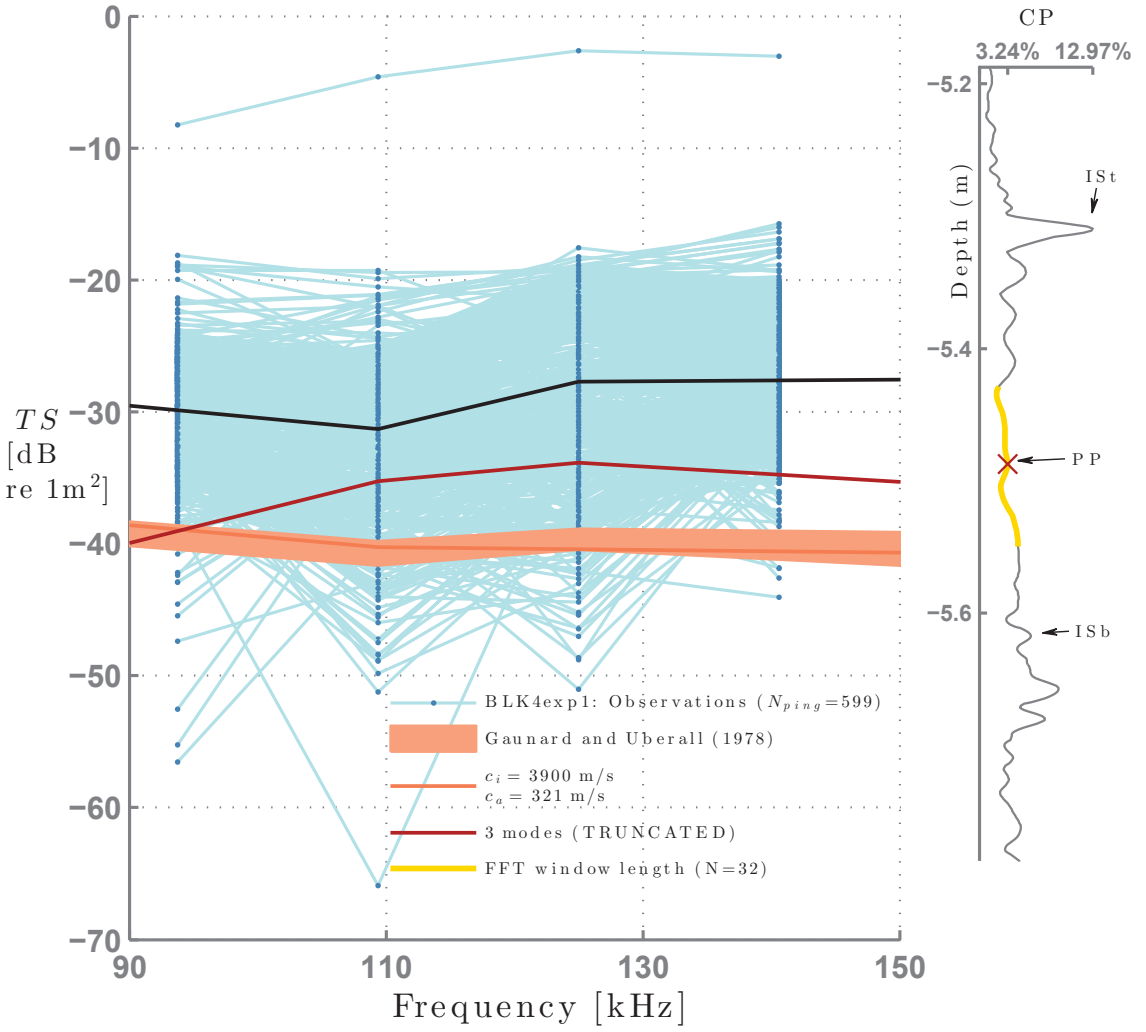

Figure 4.12: Left panel: Mean target strength from a 38 mm diameter hollow PP shell in ice [BLK4exp1] (solid black line), calculated with a 16 kHz resolution from an ensemble of pings (shown in blue) and the *Gaunard and Uberall* (1978) model (shown with its uncertainty in red). The dark red solid line shows a truncated manifestation of this model, to compare with low-resolution observations. Right panel: The CP envelope shows the average strength of the return, calculated from an ensemble of pings, relative to the transmit pulse, where the main peak in the CP envelope (red x) shows the assumed depth of the sphere (PP), with the size of the FFT window, is indicated in gold. The surface of the ice (ISt) produces a strong reflection, followed by a reflection from the bottom surface (ISb).

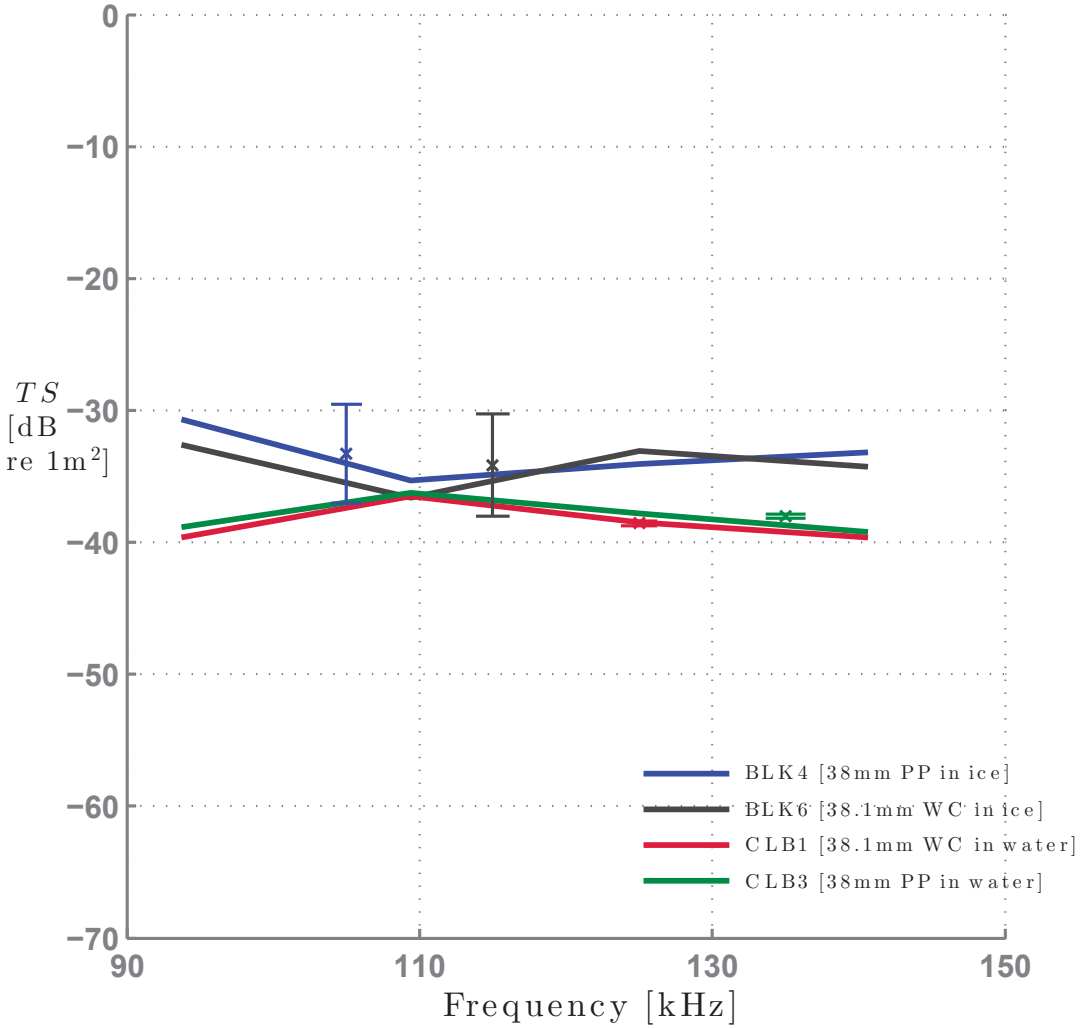

Figure 4.13: Mean observed TS from WC and PP spheres in water and ice, as solid lines, calculated with a 32-point window (16 kHz resolution). Error bars represent the variance in the TS averaged over all experiments, centred at the mean TS.

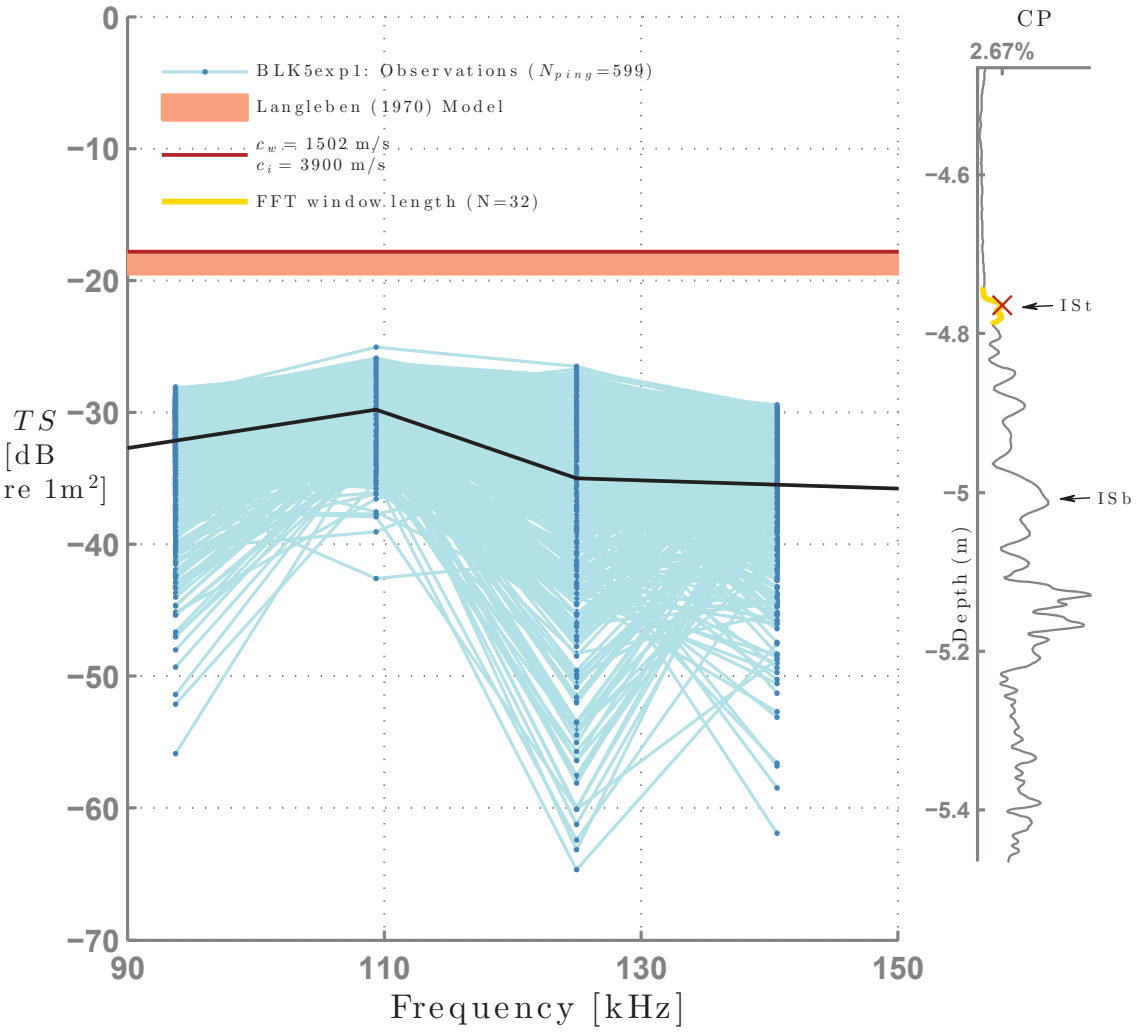

Figure 4.14: Left panel: Mean target strength from the surface of a fractured ice without inclusions [BLK5exp1] (solid black line), calculated with a 16 kHz resolution from an ensemble of pings (shown in blue), and a simple reflection model (shown with its uncertainty in red). Right panel: The CP envelope shows the average strength of the return, calculated from an ensemble of pings, relative to the transmit pulse, where the peak in the CP envelope (red x) shows the surface of the ice (ISt), with the size of the FFT window, is indicated in gold. The bottom surface of the ice (ISb) is followed by reflections from fractures within the ice.

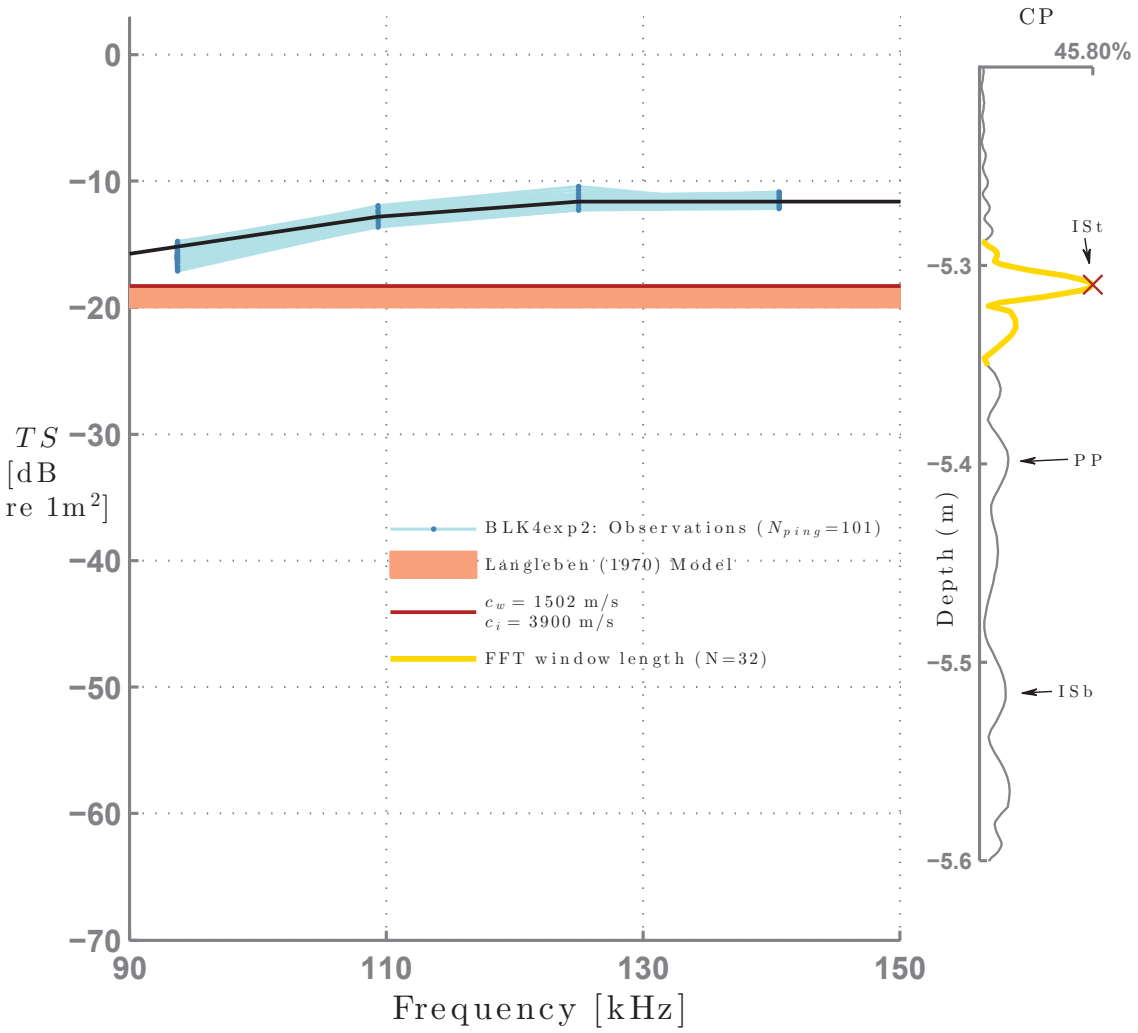

Figure 4.15: Left panel: Mean target strength from the surface of an ice block without fractures [BLK4exp2] (solid black line), calculated with a 16 kHz resolution from an ensemble of pings (shown in blue), and simple reflection model (shown with its uncertainty in red). Right panel: The CP envelope shows the average strength of the return, calculated from an ensemble of pings, compared to the transmit pulse, where the peak in the CP envelope (red x) shows the surface of the ice (ISt), and the size of the FFT window, is indicated in gold. The peak from a hollow sphere (PP) and the bottom of the ice (ISb) follow.

using Equation 2.40 (Figure 4.17). The observation varied more than the surface reflection, likely due to reverberation from within the ice.

4.3.3 Mixed Inclusions

TS from the blocks with multiple inclusions was modelled by linearly combining the backscattering cross section from *Gaunard and Uberall* (1983) to account for the number of spheres in the block, assuming that scattering is incoherent and intensities add; however, multiple scattering was not considered. Observations from multiple small, solid spheres in ice (see BLK 8 in Table 3.2) are underestimated using this simple combined model using Equations 2.41b, where the backscattering cross section was summed for each sphere contained in the beam (Figure 4.18). The 20 small solid spheres were frozen in a plane parallel to the surface, and 12.5 cm from it, but, as with single spheres, did not appear above the reverberation from the ice surface in the CP envelope. The observed TS varied from ping to ping and frequently exhibited an interference-like frequency dependence. The mean absolute mismatch from ice with multiple WC inclusions is 13.8 dB.

Observations from ice containing a mixture of different sized solid and hollow spheres (see BLK7 in Table 3.2) were overestimated by a combined model (Figure 4.18), although often had the same order of magnitude. The spheres, frozen in a parallel plane, could not be clearly identified in the CP envelope, with strong reverberation following the block.

The mean absolute mismatch was generally higher for targets in ice (Table 4.1). The uncertainty in the mismatch is the mean variance (squared standard deviation) in the mismatch calculated for all experiments from each target.

Target strengths calculated using a window large enough to contain scattering from both the top and bottom ice surfaces as well as any inclusions are shown in Figure 4.19. Observations from ice blocks with different inclusions have similar TS demonstrating that the total echo from the ice was dominated by the surface reflection.

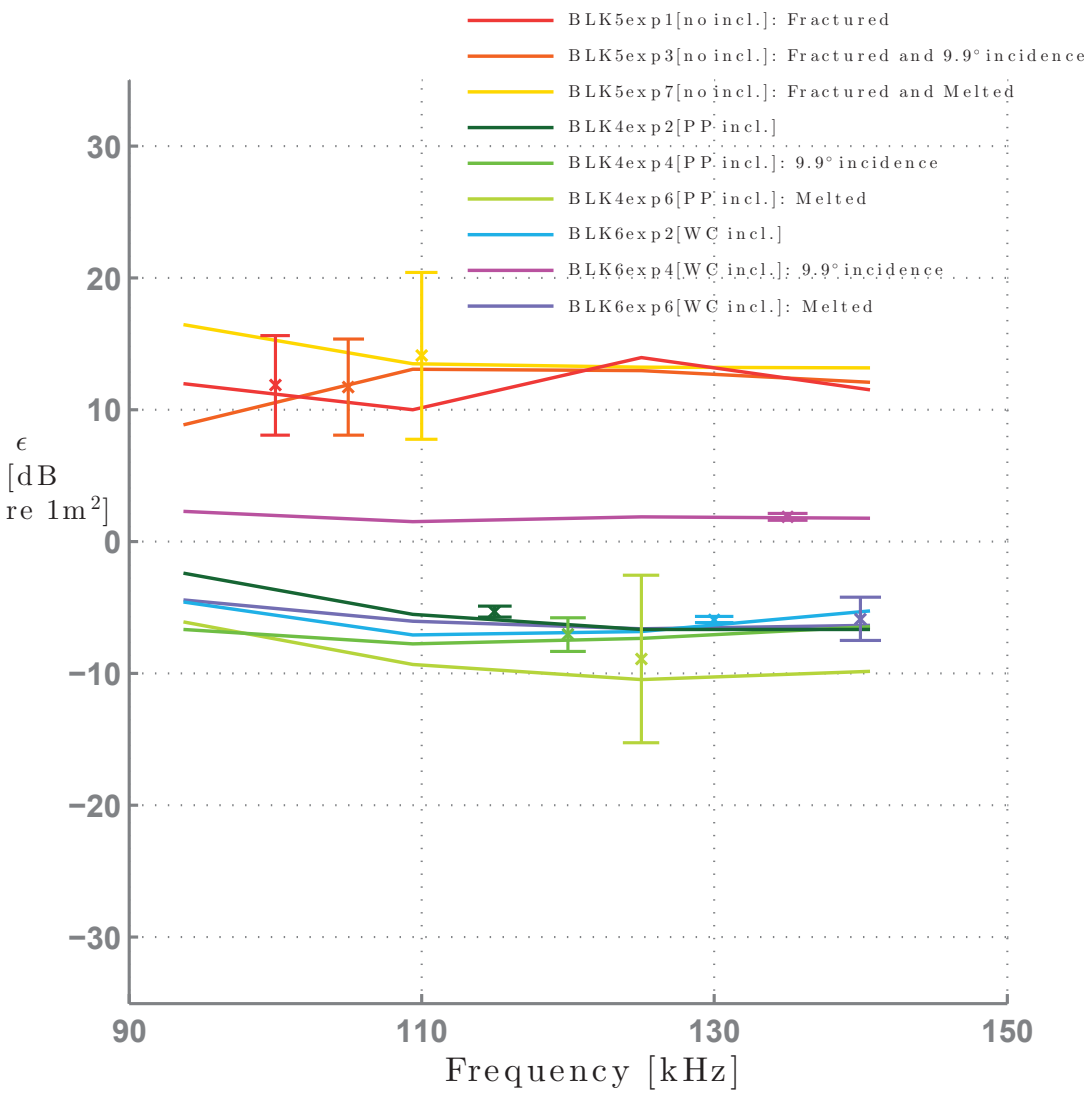

Figure 4.16: Model-measurement mismatch, ϵ, from ice surfaces with a 16 kHz resolution. The mismatch is calculated from mean TS. Error bars represent the ping to ping variance in the TS, centred at the mean ϵ.

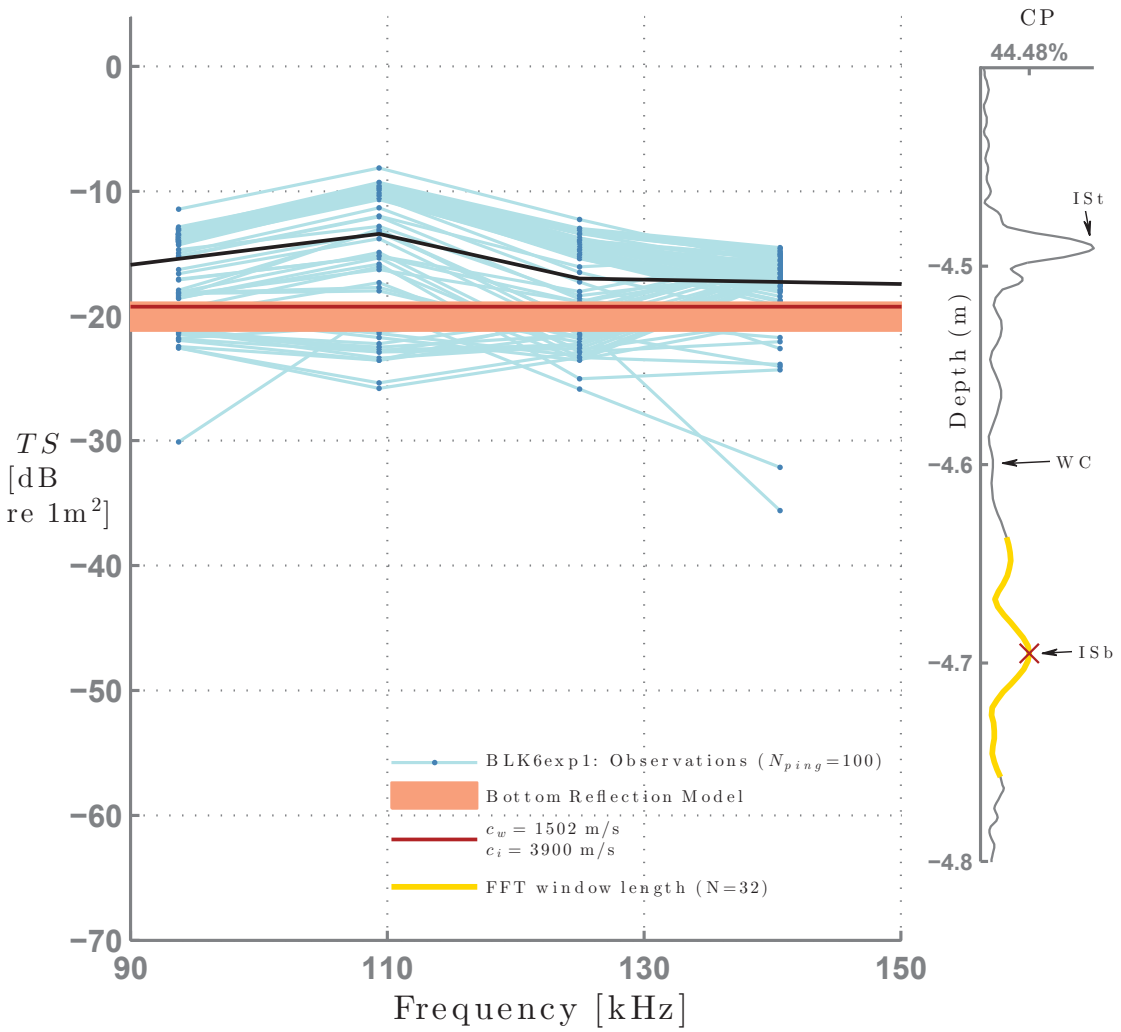

Figure 4.17: Left panel: Mean target strength from the bottom surface of an ice block without fractures [BLK6exp1] (solid black line), calculated with a 16 kHz resolution from an ensemble of pings (shown in blue), and simple reflection model adjusted for transmission through the top surface (shown with its uncertainty in red). Right panel: The CP envelope shows the average strength of the return, calculated from an ensemble of pings, relative to the transmit pulse, where the peak in the CP envelope (red x) shows the bottom surface of the ice (ISb), with the size of the FFT window, is indicated in gold.

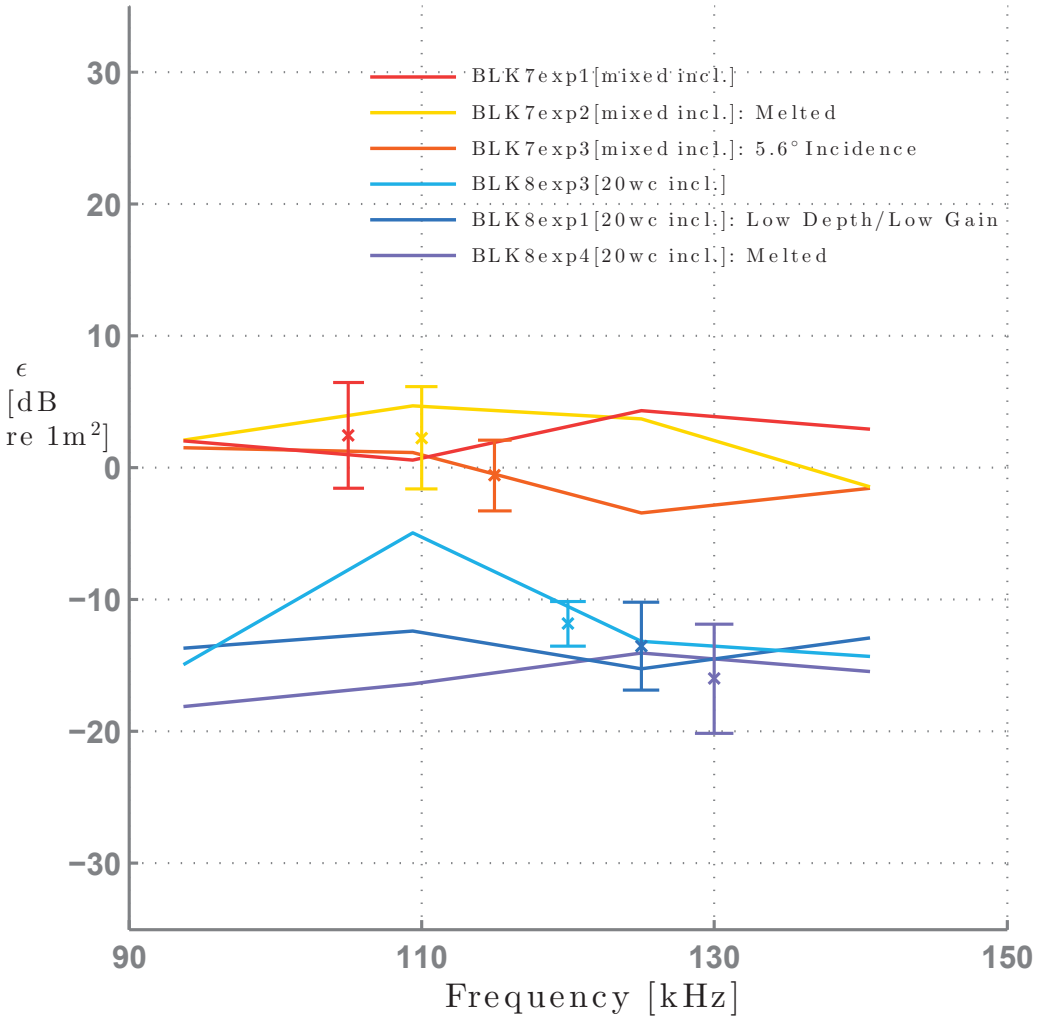

Figure 4.18: Model-measurement mismatch, ϵ, from ice with multiple inclusions with a 16 kHz resolution. Error bars represent the ping to ping variance in the TS, centred at the mean ϵ.

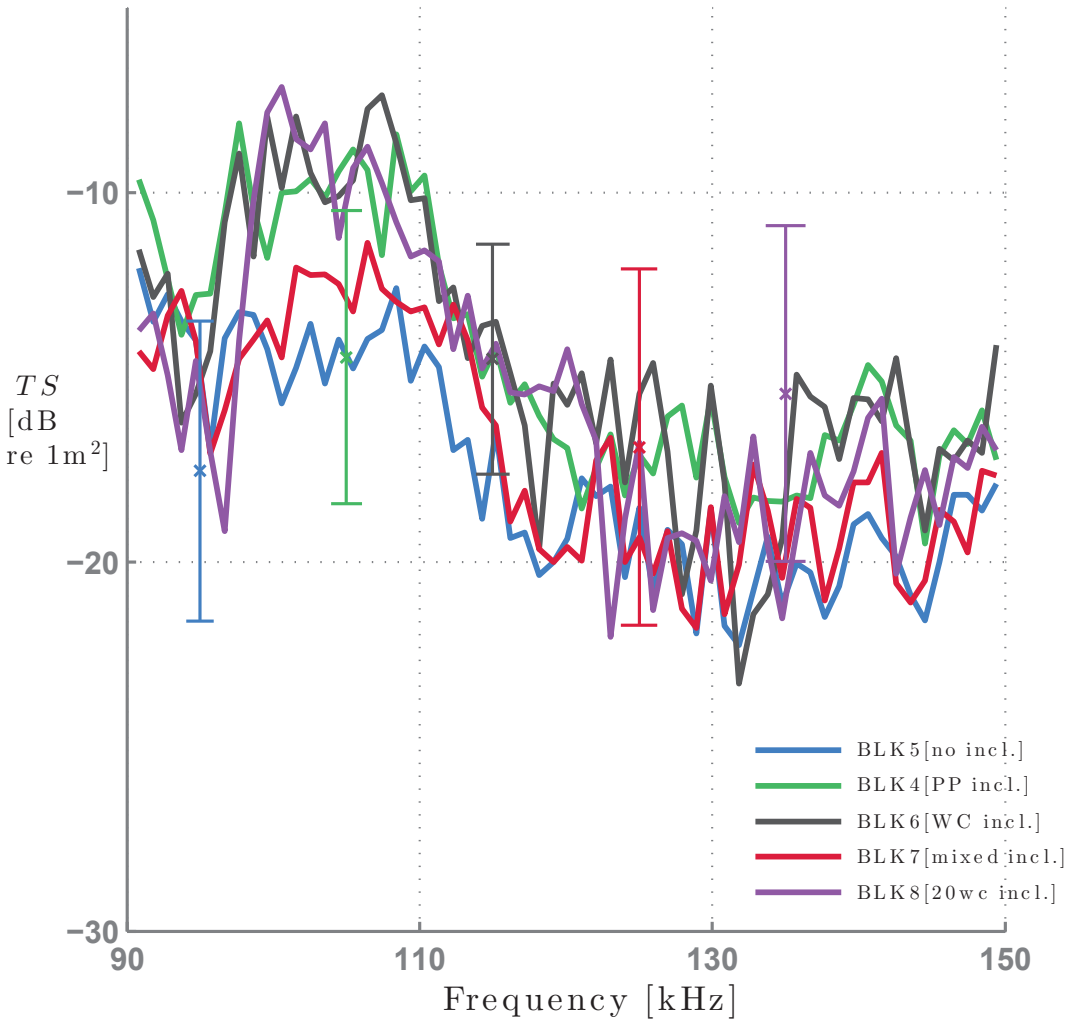

Figure 4.19: Mean observed total TS from ice blocks with various inclusions, calculated using a 512 point window containing scattering from ice surfaces and inclusions with a spectral resolution of 980 Hz. Error bars represent the variance across experiments in TS, centred at the mean TS.

Table 4.1: Summary of Mean Absolute Mismatch from Target Spheres. The mismatch shows the mean absolute value from 90-150 kHz of the difference between modelled and observed TS from each target, averaged and over all experiments. The uncertainty shows the average ping to ping variance over all experiments.

Target	$\lvert\overline{\epsilon}\rvert$ Mean Absolute Mismatch [dB re 1m^2]	Uncertainty [dB re 1m^2]	Depth [meters]
38.1 mm WC in water [CLB1]	1.0	0.5	5.1
10 mm WC in water [CLB2]	1.9	3.2	6.0
38 mm PP in water [CLB3]	1.2	0.7	5.5
10 mm PP in water [CLB4]	2.2	4.1	5.5
Fractured Ice Surface [BLK5]	16.4	3.5	4.8
Non-Fractured Ice Surface [BLK4,6]	7.2	1.6	5.3-6.2
38.1 mm WC in ice [BLK6]	14.0	3.5	4.5
38 mm PP in ice [BLK4]	9.0	4.8	5.3
Mixed Inclusions [BLK 7]	2.5	3.8	5.1
Multiple WC [BLK 8]	13.8	4.3	5.4

CHAPTER 5

DISCUSSION

Echoes from solid and hollow spheres were observed in water and ice and compared with acoustic scattering models. The observed frequency dependent TS from WC spheres in water agreed with those of *Gaunard and Uberall* (1983) and *Stanton and Chu* (2008) and could be used to calibrate the echosounder. Spheres were frozen in bubble-free ice blocks and compared with models from *Flax and Uberall* (1980) for a solid spherical inclusion and *Gaunard and Uberall* (1978) for a fluid spherical inclusion to determine whether acoustic scattering models could be used to describe the scattering from spheres in ice.

5.1 Backscattering Observations

5.1.1 Detecting Target Spheres in Water

5.1.1.1 Solid Tungsten Carbide Spheres in Water

Target spheres in water were clearly identifiable as peaks in the CP envelopes (Figures 4.4, 4.6, 4.7 and 4.8) corresponding to the location of spheres in the tank. Equation 3.3 shows that peaks in the CP output only occur where the transmitted pulse is backscattered since any other signal will be uncorrelated with the transmitted pulse. Observed TS from target sphere experiments in water confirm that the tank contained no other significant sources of scattering, since peaks were only seen at the depth of the target spheres and the bottom of the tank.

Smaller peaks that appear after the main peak attributed to the front of the sphere (Figure 4.4) are attributed to multiple wave arrivals from the sphere (*Gaunard and Uberall*, 1983); due to surface waves, such as Rayleigh waves and whispering gallery waves, that travel slower than pressure waves and circumnavigate the sphere before scattering energy back to

the transducer, thus arriving later (*Gaunard and Uberall*, 1983). The delayed returns from multiple waves extended the envelope of the scattered pressure wave and are responsible for the resonances in the observations, which result from interference between multiple scattered waves (*Gaunard and Uberall*, 1983).

Pulse compression effectively removed noise; for example no peaks were observed in the CP envelope before the 38 mm diameter sphere (Figure 4.4). However, noise is evident in the CP envelope before the return from the 10 mm diameter WC sphere in Figure 4.6, which appears as a wide diffuse peak before the return from the sphere. The returns from the 10 mm diameter spheres were less than 1% of the range corrected incident energy, which is close to the order of magnitude of system noise (0.3 % scattered return vs. 0.03 % noise floor; see Figure C.4) and the peak in the CP envelope is still clearly discernible. The returns from 38.1 mm diameter WC spheres were 4 times stronger than 10 mm diameter WC spheres (Figures 4.4 and 4.6), so that noise was not apparent in the CP envelopes from large spheres. The small peaks that occurred in front of the return from the sphere are artifacts from pulse compression, where some of the energy in the peak leaks out resembling a cardinal sine function (*Stanton and Chu*, 2008). These processing side lobes are significantly smaller than the main return and subsequent arrivals from the sphere (Figure 4.4), thus they do not inhibit detection of the target.

As expected, observed TS agrees well with the *Gaunard and Uberall* (1983) model, with a mean absolute mismatch of 1.0 dB for 38.1 mm spheres and 1.9 dB for 10 mm spheres. The mismatch from the 38.1 mm diameter sphere is due to ping variability between experiments. The largest mismatch for the 38.1 mm sphere occurs near resonant frequencies (Figure 4.5), since the precise location of the resonances change slightly with the size of the FFT window; where larger windows more accurately locate the resonant frequencies, but introduce more noise into the spectrum as the proportion of the window containing background noise increases (compare CLB1 and CLB3 in Figure 4.9 (980 Hz resolution) and Figure 4.13 (16 kHz resolution)). Windows that contain less than 64 points no longer reliably resolve the strongest resonance at 135 kHz (Figure 4.13).

The mismatch from the 10 mm WC sphere and the *Gaunard and Uberall* (1983) model results from noise that could not be removed from the signal (Figure 4.6). The frequency dependence from the observations agrees with the model, although significantly higher mismatch occurs in the lower band of the receiver (between 90-110 dB) which is attributed

to a higher noise floor at these frequencies (see Appendix C, Figure C.4), consistent with Figure 4.8. Since the noise floor is higher in the low frequency range the return from the sphere may be masked by noise and removed as a result of pulse compression. Scattering observations from WC spheres are provided in *Faran* (1951), *Gaunard and Uberall* (1983), *Stanton and Chu* (2008) and *Dragonette et al.* (1981) and also agree well with the *Gaunard and Uberall* (1983) model, however these measurements are made using higher frequency echosounders, where $14 < ka < 70$, using spheres that are at least 25 mm in diameter. My observations show that these models are valid for 10 mm and 38 mm diameter spheres from 90-150 kHz ($1 < ka < 12$) *Stanton and Chu* (2008) suggest better resolution from larger spheres, since the echo from the front interface and multiple wave arrivals will be better resolved.

5.1.1.2 Echosounder Calibration

The strong scattering from the 38.1 mm diameter WC sphere and good model comparison make it an ideal calibration target using the method of *Stanton and Chu* (2008) (Section 3.2.2), since it can be clearly distinguished from background noise (right panel, Figure 4.1). The uncalibrated return exhibited strong resonances and low ping variability (Figure 4.1), and therefore deviations from the *Gaunard and Uberall* (1983) model were attributed to the frequency dependent response of the echosounder system (*Stanton and Chu*, 2008). The observed TS spectra, and thus the calibrations, contained spectral noise that differed between measurements, such as in Figure 4.5. Applying a 10 kHz moving average filter smoothed the calibrations, producing a consistent frequency dependence. Calibrations made from WC spheres of different sizes, gain settings and depths had a consistent frequency dependence and magnitude (Figure 4.3). Note that excluding the diffuse noise peak before the 10 mm WC sphere from the FFT window did not produce a significantly better calibration. This suggests that the model-measurement mismatch is due to noise recorded simultaneously with scattering from the sphere. The calibrations from 38.1 mm WC were most affected by the size of the FFT window, where Figure 4.2 shows that windows containing less than 128 points have a magnitude and frequency dependence that is inconsistent with larger, more reliable, windows; due to the exclusion of multiple wave arrivals from the window that are required to resolve the elastic resonant response of the sphere.

5.1.1.3 Hollow Polypropylene Shells in Water

The CP envelope from 38 mm diameter hollow spheres were also clearly distinguishable in water (Figure 4.7). The scattering from PP shells was differentiated from that of WC spheres by less pronounced multiple wave returns. This indicates that circumferential shear waves were not as strong, compared with WC spheres. *Gaunard and Werby* (1991) observed strong multiple wave arrivals from air-filled steel shells, which suggests that the PP shell does not support strong circumferential waves, compared with steel, likely because PP has a lower shear modulus (Table 2.1). Compared with *Gaunard and Werby* (1991), my observations show that changing the material of the shell effects the envelope of the scattered wave.

Since there are no comparisons of models and observations of scattering from air-filled PP shells in the literature, I compared observed TS with the *Gaunard and Werby* (1987) model and the *Anderson* (1950) model. Observations from both large and small hollow shells agree well with the *Anderson* (1950) model, with a mean absolute mismatch of 1.2 dB and 2.2 dB, respectively, but are offset from the *Gaunard and Werby* (1987) model by 7.3 dB and 4.9 dB, respectively, partially owing to the poor resolution of resonances in the observation (Figures 4.7 and 4.8). The absence of strong resonances in the observed TS suggest that the properties of the shell are not well determined or that multiple wave arrivals from the shell are smothered by the echo from the air-filled cavity. This result suggests that hollow PP shells may be used to simulate scattering from large air bubbles in water. For the small shells, the observations do not agree with the *Anderson* (1950) model at low frequencies, consistent with low SNR from the small WC sphere (compare CP envelope (right panel) in Figure 4.6 and 4.8 with Figure C.4). The apparent frequency dependence in these observations could be due to a weak contribution from the PP shell, or noise in the system. *Anstee* (2002) measured frequency dependent TS from various spheres and spherical shells filled with different fluids, including a 400 mm diameter air-filled nylon shell with a 3 mm wall thickness and concluded that air-filled plastic shells are not viable calibration targets since scattering strength varies strongly with frequency. In my case, since the shell is thinner (≈ 1 mm), it appeared to have an insignificant effect on frequency dependence of the echo. Both *Gaunard and Werby* (1987) and *Anstee* (2002) were able to model backscattered TS from air-filled steel or ceramic shells.

The observed TS of target spheres in water suggest that backscattering across the 90-150 kHz bandwidth is sufficient to differentiate between the different sizes of spheres, but are less effective at differentiating the material properties of the spheres (Figure 4.9). Observations from large solid and hollow spheres are only distinguishable by the presence of a strong resonance at 135 kHz (ka=10.8), while the echo from small hollow spheres is generally indistinguishable from the of small solid spheres. Since observed TS from WC and PP target spheres agree with the scattering models, developed in Chapter 2; I expected that these models with boundary conditions appropriate to ice as a surrounding medium should also apply to these same targets in ice. However, let's first consider scattering from the ice surface.

5.1.2 Reflections from Ice Surfaces

Observations from the ice blocks typically show multiple strong reflections, where the first return is the compressional wave reflected from the top surface, which can be modelled as a simple planar interface (see Section 2.2.7). The reflection from the top surface of planar ice without cracks is the strongest feature in the CP envelope in Figures 4.10 (BLK6), 4.12 (BLK4) and 4.15 (BLK4). Reflections from the top surface of the ice are underestimated by the model by 8 dB at normal incidence (Figure 4.16). The observations generally follow the expected spectral shape, except at low frequencies. This may indicate surface roughness, which was not quantified. However, the effect of block shape and surface roughness on TS can be considered negligible for observations made soon after the ice was introduced to the water, since the ice was initially planar.

In addition, the top surface of the ice remained smooth and generally planar as the ice melted. As the ice melted, a fresh water plume rose from the block, since the fresh melt water from the block was lighter than the water in the tank (see Figure C.2). Since this melting water flowed away from the ice block, it did not contribute to uneven melting at the top surface. This plume may also explain the presence of small peaks in the CP envelope that occur before the surface of the ice (Figures 4.10, 4.12 and 4.15). Conversely, as the block melted from the bottom surface, fresh water would be forced past the block due to buoyancy. Any small scale roughness that was present would trap the rising water under the ice; a feedback that could produce the large scale roughness along the bottom surface observed at the end of the experiments. *Skyllingstad et al.* (2003) and *McPhee et al.* (2008) show that melt water below sea ice keels tends to flow upwards, forming convective

cells beneath the ice sheet that can contribute to the growth of bottom roughness. This melt water was observed using acoustic scattering measurements (*McPhee et al.*, 2008).

Blocks with significant cracks (see Figure 5.1) reflected considerably less of the signal back to the transducer (Figure 4.14) and are overestimated by as much as 15 dB by the surface reflection model (Figure 4.16). This suggests that surface deformation, resulting from cracks within the block, diminishes the echo from the top ice surface. This energy is diffusely scattered and not transmitted into the ice. Previous observations show that acoustic reflections from sea ice are best modelled by assuming that an acoustically soft layer is present at the ice-water interface due to melting, cracks and open pores at the ice surface (*Mayer*, 1974; *Stanton et al.*, 1986; *Garrison et al.*, 1991). *Langleben* (1970) measured the reflection coefficient at seawater-sea ice interfaces and found that the density of the surface layer increases ($996\ kg/m^3$), while the soundspeed decreases ($1810\ m/s$), which implies that the surface layer, referred to as the skeletal layer, is a mixture of ice and water. The skeletal layer is assumed to lower the reflection strength from submerged ice surfaces (*Stanton et al.*, 1986). My observations show that the strength of the surface reflection does not change significantly as the block melts (Figure 4.16) which implies that a skeletal layer is not present as the bubble-free ice blocks melted. However, increased surface roughness due to cracks is assumed to decrease the strength of the specular surface reflection (*Garrison et al.*, 1991).

The ice surface reflection model indicates that the strength of the reflection should not vary strongly over the range of incidence angles ($\theta < 10°$) (*Langleben*, 1970) in the scattering experiments (Figure 2.7), which generally agrees with my observations (BLK4 and BLK5 in Figure 4.16). The dependence of the amplitude of the reflected wave on incidence angle was modelled using Snell's Law in Equation 2.33 (*Medwin and Clay*, 1998), which implies that the strength of the surface reflection should increase, since less energy is transmitted through the surface at non-normal incidence; however, at significantly oblique incidence the reflection from the ice surface will not be scattered toward the transducer. The strength of the reflection decreases in some observations (BLK6 in Figure 4.16) at oblique incidence,which indicates that the surface reflection was not scattered toward the transducer. The surface reflection model also does not consider that the beam encounters the lateral faces of the ice at oblique incidence, however it is unlikely that scattering from the lateral faces will be recorded at the echosounder. Measurements

from *Langleben* (1970) agree with the simple reflection model and show that the strength of the reflection from ice surfaces increases with increasing angle of incidence and shows no tendency to increase with increasing frequency.

The surface reflection model assumes that only compressional waves will be transmitted into the ice, which allowed me to ignore the effect of shear wave generation in the ice block, which is deemed reasonable by observations of surface reflections from *Langleben* (1970). However, *Miller and Schmidt* (1991) observed that a compressional wave at oblique incidence generated shear waves in ice. These shear waves may scatter additional compressional waves from the ice surface, due to mode conversion (*Xie and Farmer*, 1994), that could extend the envelope of the bulk reflection from the ice surface, referred to here as surface reverberation (seen in the right panel of Figure 4.15, following ISt).

Reflections from the bottom surface confirm that sound enters the non-cracked ice block, but must encounter a strong enough target in order to be identified above surface reverberation. Reflections from the bottom surface of the ice are underestimated by 8 dB using a combined ice surface reflection and transmission model. In non-cracked ice, a strong peak after the top ice surface was associated with an echo from the bottom ice surface (Figure 4.17), the strength of which was underestimated using estimates of reflection and transmission at normal incidence (see Equation 2.40). As the ice melted, the reflection from the bottom surface became harder to identify. The large variance in the observations from the bottom ice surface can be attributed to overlapping reverberation from other ice surfaces, since ice reverberation depends on the shape and location of the ice in the tank, and thus changes between pings as the ice melts. The reflection from the bottom ice surface will also become more diffuse as the ice melts and the bottom surface becomes rough. A reflection from the opposite ice surface in ice have been identified in sea ice reflections by *Winebrenner* (1991) and *Garrison et al.* (1991). *Winebrenner* (1991) shows that the bottom reflection is only identified at low incidence angles and when the skeletal layer is minimal.

5.1.2.1 Ice Reverberation

The reverberant echoes that follow the top and bottom surface of the ice can attributed to reverberation, due to shear and flexural waves along the ice surfaces and multiple reflections from compressional and shear waves trapped in the ice (*Chamuel*, 1990), or the frame and lead weights used to oppose the buoyancy of the ice. Scattering from the frame

occurred more than a meter from the bottom surface of the ice and was clearly identified in the backscattered signal. The structure of the reverberant echo varies significantly between pings and experiments and appears to depend on the shape, surface roughness and orientation of the block (*Chamuel*, 1990). Reverberation from ice surfaces have been identified in a number of studies; summarized in *Kutschale* (1969). *Milne* (1964), *Brown and Brown* (1966) and *Mellen and Marsh* (1965) attribute strong reverberation from the underside of sea ice to surface roughness and local under-ice topography and multiple reflection from within the ice sheet (*Kutschale*, 1969). My observations show that reverberation following the ice block can be stronger than distinct surface reflections, which suggests that multiple compressional waves arrive simultaneously at the receiver (Figures 4.12 and 4.14) . Multiple reflections from ice surfaces can add constructively or destructively depending on the phase of the scattered waves.

Reverberation from ice surfaces can also be attributed to scattered compressional waves that are the result of mode conversion from flexural surface waves and shear waves in ice (*Xie and Farmer*, 1994; *Anderson*, 1961; *Weng and Yew*, 1990; *Mayer*, 1974; *Williams and Robinson*, 1981; *Oliver et al.*, 1954; *Hunkins*, 1960; *Miller and Schmidt*, 1991). The presence of flexural and shear waves on ice surfaces in contact with water were modelled by *Ewing et al.* (1934) and *Press and Ewing* (1951), who predict that a floating ice sheet is capable of supporting compressional, shear, longitudinal, flexural and surface (Rayleigh, Stoneley and Love) waves. *Dugan et al.* (1992) observed flexural waves in ice between 1-10 kHz and *Squire et al.* (1995) shows that flexural waves with frequencies up to 100 kHz can exist in ice. Both *Dugan et al.* (1992) and *Squire et al.* (1995) show that acoustic compressional waves dominate the vibrational motions of ice above 50 kHz. Surface and flexural waves are coupled with the surrounding fluid and depend on the frequency of the vibration, the density of the water and ice, the elasticity and flexural rigidity of the ice sheet, the thickness of the ice and the depth of water (*Press and Ewing*, 1951). These waves are dispersive, such that the wave speed depends on frequency (*Anderson*, 1963). Flexural waves in Arctic ice have been observed by *Williams and Robinson* (1981) at less then 1 Hz and surface waves in porous sea ice have been identified by *Weng and Yew* (1990) between 1-10 kHz. In both cases, a seismic transducer was affixed to the ice surface. The generation of shear and surface waves from a purely compressional incident wave was observed by *Mayer* (1974) and *Xie and Farmer* (1994), who found that compressional

waves at oblique incidence would form shear waves in ice. Flexural, surface and shear waves are not supported in water and would only be identified in my experiments once converted to compressional waves in water and scattered toward the transducer.

The interactions between shear waves along the surface of the ice and the surrounding water due to mode conversion were ignored in my surface scattering model. Elastic wave models are available, however, for non uniform (*Robins*, 1998), anisotropic (*Mandal*, 1991), rough (*Abeele et al.*, 1996) or porous (*Weng and Yew*, 1990) ice surfaces that consider the effect of shear, flexural and surface waves; extrapolated from the *Ewing et al.* (1934) elastic wave propagation model. The portion of ice reverberation that results from multiple reflections by compressional waves may be explained by accounting for the time delay from the main surface reflection and then estimating the magnitude of successive arrivals by combining reflection and transmission coefficients (see Equations 2.33 and 2.34). Since modelling multiple reflections of elastic waves from lateral ice surfaces was outside the scope of my work, observations from inclusion-free ice blocks were made in an attempt to characterize the reverberation from the ice surface as the block melted. A true control was not obtained since all inclusion-free ice blocks cracked in the water (see Figure 5.1).

In addition, my observations show that the duration of reverberation varies between experiments and is especially sensitive to cracks that act as sources of scattering within the ice (compare the right panel, following ISb, of Figure 4.14 with Figure 4.15). *Chamuel* (1990) suggest that surface and flexural waves are attenuated and scattered by cracks and ice porosity, which implies that reverberation due to surface and flexural waves in my experiment would be sensitive to surface cracks.

5.1.3 Detecting Target Spheres in Ice

Target spheres could not be located within the ice block. The inclusions did not produce distinct CP peaks stronger than ice reverberation (Figure 4.10 and 4.12). The TS from within the ice block suggests that the echoes from target spheres in ice are masked by multiple waves scattered from the ice surface. The CP envelopes in Figure 4.10 and 4.12 show that, as expected (see Figure 2.8), the magnitude of the echo from ice surface was at least an order of magnitude higher than the echo from target spheres . However, I observed peaks that appeared to originate from within the ice that are 3 to 5 times stronger than the echoes from target spheres in water (right panel, Figures 4.10 and 4.12). Since the target's impedance contrast is greater in water the strength of the echo from targets in water is

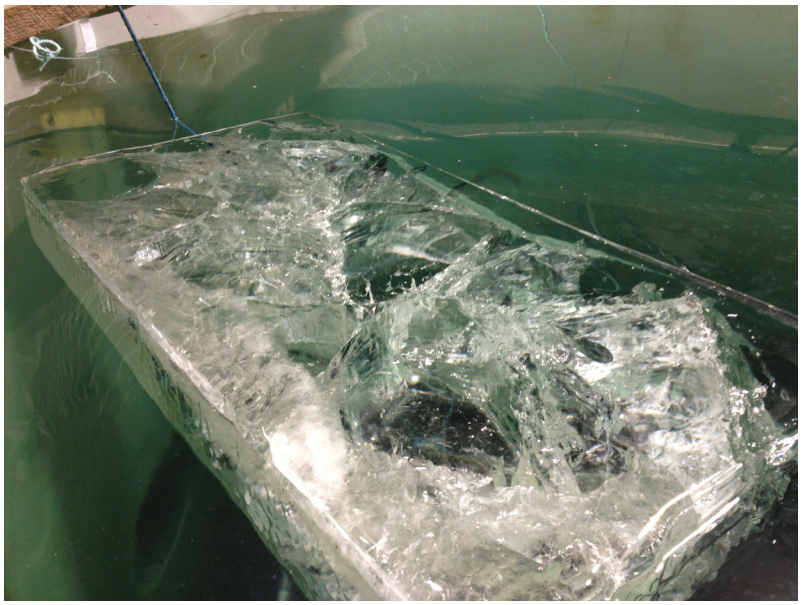

Figure 5.1: Ice blocks without inclusions cracked extensively when introduced to the water.

expected to be stronger than from targets in ice. Hence, the peaks from within the ice correspond to ice reverberation that masked the echo from the encased target spheres. Note that the observed TS from inside the ice was characterized by large ping to ping variation compared with target spheres in water (Figure 4.13), which is likely due to the variance in ice reverberation, whose magnitude and envelope are affected by the ice melting and shifting in the net throughout each experiment. The elastic wave models in *Chamuel* (1990) and observations in *Jezek et al.* (1990) show that surface wave propagation and attenuation are sensitive to melting and cracking at the ice surfaces.

As a result, when I isolated the scattering from the range of the spheres by applying a 32-point window, 12.5 cm from the surface reflection, the observed TS isolated from target spheres in ice did not reproduce the modelled frequency dependence (Figure 4.11). Although the exact location of the spheres within the block was not quantified as the ice block melted, most ice blocks contained a local maximum in the CP envelope near the assumed location of the sphere (right panel, Figure 4.10). However, since this peak occurred within reverberant echoes from the ice surface, I am not able to conclusively attribute any peaks in the CP to the encased sphere. It is most likely that the reverberation that masked the sphere is indicative of surface or shear waves, since there are no scattering mechanisms or cracks between the surface and the encased target spheres in Figures 4.10 and 4.12. As a result, multiple reflections from compressional waves would arrive after

scattering from an encased target.

Observations from multiple targets in ice also show poor agreement with models and reinforce my conclusion that the ice surface dominates the echo and that cracks at the surface diminish the the magnitude of the surface reflection and reverberation within the ice (Figure 4.18). TS from the interior of non-cracked ice with multiple encased targets (BLK8 in Figure 4.18) was underestimated by the combined scattering models (Equation 2.41b), while TS from the interior of cracked ice (BLK 7) with multiple targets is of the same order of magnitude expected from the scattering model. Again, since the target spheres did not produce a peak in the CP envelope I conclude that the echoes from ice inclusions are swamped by ice reverberation.

Observed TS from ice blocks fully contained within the Fourier transform window are generally indistinguishable (Figure 4.19), which supports the conclusion that scattering from ice surfaces dominate the echo. This shows that even though the surface reflection from the cracked blocks was lower than the reflection from blocks without cracks, including the multiple wave returns in the window brings the observations into agreement with the combined scattering model (see Equation 2.41c).

Unfortunately, the observed TS from spheres in ice did not allow me to comment on the validity of the *Flax and Uberall* (1980) or *Gaunard and Uberall* (1978) models, since the echoes from the spheres were smaller than those due to ice reverberation. However, these models have been verified by previous observations; for example *Sessarego et al.* (1998) showed that the *Flax and Uberall* (1980) model agrees well with scattering from an aluminum inclusion in Plexiglas and *Bin et al.* (2006) showed that the *Gaunard and Uberall* (1978) model can be used to predict scattering from air cavities in neoprene and rubber. In both cases, the transducer is affixed to the encasing solid medium so that scattering did not occur at the solid interface. *Ying and Truell* (1956) suggested that it is difficult to ensure that the sphere is in contact with the solid medium, as a result, measurements validating these models are sparse. In order to test these models where the transducer is not flush with the surface of the solid, the spheres must be placed far from the solid interfaces, requiring very large blocks. A model that predicts reverberation from the ice surfaces will be needed to determine the adequate spacing (for example, see *Chamuel* (1990)).

My results demonstrate that propagation and mode conversion of elastic waves at ice surfaces must be well characterized in order to separate surface scattering from internal

scattering; which requires characterization of shape, surface roughness and crack extent of the ice as it melts (*Jezek et al.*, 1990). Note that both the spherical inclusion models (*Flax and Uberall* (1980) model and the *Gaunard and Uberall* (1983) model) assume that the solid medium is isotropic, which may not be appropriate for ice (*Anderson*, 1961). *Anderson* (1963) suggested that sea ice will have both macroscopic anisotropy, due to thermal gradients in the ice, and microscopic anisotropy, due to crystal orientation. *Anderson* (1961) argue that surface waves observed on floating ice sheets can be modelled by assuming the ice is locally polar anisotropic, or transversely isotropic; which mean that the material properties are symmetric about one planar axis (*Anderson*, 1961). The spherical inclusion models also assume that the wave incident on the sphere is purely compressional, which also does not appear to be the case. Reflection models from *Jezek* (1985) and *Langleben* (1970) imply that shear waves can be generated by compressional waves that encounter the surface at non-normal incidence. *Miller and Schmidt* (1991) observed compressional, flexural and transverse waves generated by a complex compressional wave underneath Arctic sea ice.

5.2 Application to Sediment-Laden Ice

My results show that reverberation from the smooth, bubble-free ice surface is strong enough to swamp echoes from large WC and air-filled spheres in ice. These spheres are much stronger targets than individual air and sediment particles, and are more separated from the ice surface and other inclusions then they would be in SL ice, which suggests that it will be much harder to isolate scattering from individual sediment and air inclusions in ice. The echoes from sediment and air inclusions will arrive at the echosounder simultaneously with reverberation from the ice surface; and once echoes overlap, it is difficult to decompose the signal by source contribution. *Winebrenner* (1991) mentions the possibility of observing scattering from inhomogeneities in sea ice in acoustic reflections, and similarly concludes surface scattering effects will dominate scattering from ice inclusions and suggest that inclusions in ice may behave similarly to surface roughness and extend the envelope of the scattered wave.

Since the surface of SL ice is expected to be rough and cracked, the strength of the surface reflection is expected to be weaker in SL ice than the blocks in my experiment, as *Garrison et al.* (1991) showed that the reflection from ice is strongly dependent on

surface roughness and cracks. Both *Black* (2013) and *Trowse* (2013) describe a boundary layer where melting occurs in SL ice, which is similar to the transition, or skeletal layer in sea ice, described by *Stanton et al.* (1986) and *Garrison et al.* (1991). The skeletal layer, which was not identified in my experiments, is expected to influence surface scattering in SL ice. *Winebrenner* (1991) showed that transmission of elastic energy into ice would be diminished by the skeletal layer. *Sanderson et al.* (2012) observed that the surface of SL ice blocks is more porous than the interior of the ice block, and that at low tide, SL ice blocks are observed by *Sanders and Baddour* (2008) to be covered in a thin layer of unconsolidated mud, deposited as the tide recedes. This layer of sediment freezes to the block and contributes to the growth of SL ice blocks (*Black*, 2013). In the case of a gradual transition into a rigid ice matrix, shear and compressional waves will be attenuated at the surface of SL ice, further inhibiting the likelihood of identifying inhomogeneities in ice (*Winebrenner*, 1991).

Reverberation from the ice surfaces is also expected to increase as cracks and surface roughness increase (*Chamuel*, 1990). My observations imply that reverberation from SL ice blocks will likely be complex since the duration and magnitude of ice reverberation appears to increase as the surface is deformed. In order to model the reflection from a submerged SL ice block, the effect of surface roughness, porosity and crack extent on the strength of the reflection must be verified.

My observations imply that scattering from sediment or air inside ice cannot be identified using the *Gaunard and Uberall* (1978) or *Gaunard and Uberall* (1983) models; thus, these models should not be used to estimate sediment content or porosity of SL ice blocks from acoustic backscattering.

5.2.1 Recommendations for Future Work

Acoustic detection of ice strength may still be feasible, since the strength of the reflection from ice surfaces depends on the extent of surface cracks. If surface cracking is a reasonable measure of the ability of an ice block to withstand a collision, where surface cracks indicate a network of internal fractures, the strength of the surface reflection may be used to assess the risk ice blocks pose to tidal turbines. *Stein et al.* (1998) devised a method to monitor the mechanical properties of ice by measuring the dispersion rate of the flexural waves. However, this method requires that the transducer is fixed to the ice surface (*Stein et al.*, 1998). *Stein et al.* (1998) shows that if shear wave scattering can be detected, the ice density

and lamé parameters are calculated from the longitudinal and shear soundspeed. Since remote detection of SL ice requires that the transducer is not attached to the ice, properties of shear waves in ice must be inferred from corresponding scattered compressional waves using the mode conversion models provided in *Graff* (1975) and *Aki and Richards* (1980). Furthermore, *Weeks and Assur* (1967) showed that the mechanical and elastic properties of ice exhibit a strong temperature dependence, observed by *Rajan et al.* (1992) by measuring the variation in temperature and wave speed in sea ice. These studies suggest a relationship between the strength of the ice surface reflection and the strength of SL ice blocks. In order to test this conjecture, the strength, surface fracture extent and porosity of sediment-laden ice should be sampled (for example, see *Notz et al.* (2005)) and compared with surface reflection observations and models.

Elastic wave propagation models for porous solids may be applied to porous sediment laden ice blocks (*Biot*, 1962; *Williams and Francois*, 1992; *Laible*, 1995; *Sharma*, 2007). *Biot* (1962) developed a theory which laid the foundation for poromechanics by coupling increasing pore pressure to compression of the medium. Biot theory can be used to determine the elastic moduli in anisotropic, open pore media, where the pore space is connected; however, this method requires at least 12 parameters, many of which are difficult to measure (*Biot*, 1962). *Williams and Francois* (1992) simplify the Biot theory for an isotropic, closed pore medium; requiring 7 parameters that are measurable in ice and related to ice temperature and salinity (*Williams and Francois*, 1992). This model produced reasonable estimates of porosity and ice temperature and salinity in melting sea ice (*Williams and Francois*, 1992). *Sammelmann* (1993) partitioned the sea ice into two layers; a solid viscoelastic layer and a dendritic, skeletal (Biot-Stoll) layer. Estimates of reflection coefficients are sensitive to small variations in the thickness and porosity of this layer (*Yew and Weng*, 1987). If the porosity of ice could be controlled, an experiment to measure the strength of the surface reflection while varying the porosity of the surface layer of ice may provide a method to remotely estimate the surface strength of a SL ice block. Observations of porosity in different layers of SL ice are provided by *Sanderson et al.* (2012) and could be used to parameterize the Biot model to estimate the reflection strength from SL ice blocks. Note, however, that this model does not incorporate scattering from frozen or unconsolidated sediment in the skeletal layer.

Passive acoustic monitoring of sediment laden ice may be a cost-effective option for

monitoring ice near turbines. Acoustic waves are naturally generated by ice cracking and colliding in the water, which is identified as a major source of noise in the Arctic (*Dyer*, 1993) . The acoustic emissions from cracking events have been modelled by *Stein* (1988) and *Farmer and Xie* (1995) showed that it is possible to attribute transient acoustic waves in water to acoustic emissions from large sea ice fracture events (*Farmer and Xie*, 1995) and resultant flexural and Rayleigh surface waves that also produce acoustic waves in water (*Stein*, 1988). *Wadley et al.* (1981) and *Langhorne and Haskell* (1996) both showed that these acoustic emissions can be used to infer properties of the ice. For example, *Langhorne and Haskell* (1996) suggested that the timing of fractures can be used to indicate ice strength; where frequency acoustic emissions associated with cracking preclude the failure of the ice block (*Zakarauskas*, 1993). While these fracturing events are much louder than expected from SL ice, fracturing events from SL ice may have a unique frequency dependence that allows them to be differentiated from other sound sources. In addition, *Weber* (1978) showed that the sound of ice collisions can be used to track ice floes; however, their observations showed that noise from an ice floe is too loud to detect ice strengths or velocity changes.

Acoustic backscattering observations should be made from SL ice blocks. Observations in a laboratory could be made from single, submerged SL ice block that are centred in the beam of the transducer and ensonified at different grazing angles. Since reliable melt rate model for SL ice is provided by *Trowse* (2013), surface reflection strength may provide an additional measure of the development of a skeletal layer on submerged ice blocks. Alternatively, an echosounder mounted to the surface or seafloor in Minas Passage, where SL ice floes are proposed to occur, may identify submerged solid objects. While a large range of target strengths are expected from the ice surface, observations from the Minas Passage could be compared with observations from sea ice (for example, *McCammon and McDaniel* (1985); *Yew and Weng* (1987); *Laible and Rajan* (1996); *Stein et al.* (1998)) to provide a first order estimate of where and whether SL ice is found in the water column.

5.3 Summary and Conclusions

The goal of my thesis was to test the possibility that, using broadband acoustic techniques, inclusions in ice could be isolated from surface scattering and identified by comparison

with an acoustic scattering model. I found that scattering from a planar surface of bubble-free ice overwhelmed the echo from a 38 mm and 10 mm tungsten carbide spheres and polypropylene shells encased in ice. The surface echo inhibited the detection of the spheres in ice, so that acoustic scattering models could not be verified. As such, I am unable to conclusively detect or distinguish between solid and hollow spheres in ice using broadband acoustics. The total echoes from ice with inclusions could not be differentiated from ice without inclusions, however, inclusion free ice could not be maintained underwater without cracking. This implies that echoes from sediment laden ice blocks cannot be interpreted by modelling separate scattering mechanisms within the ice, and that future modelling should focus on bulk parameterization of sediment laden ice.

APPENDIX A

SPHERICAL HARMONICS

Spherical harmonics, composed of different kinds of spherical Bessel functions and Legendre polynomials are common in wave scattering problems with spherical symmetry (*Boas* (1966)). These functions form a complete orthonormal basis set, much like trigonometric functions in the Fourier series, where any function can be expanded in terms of a sum of orthogonal functions (*Boas* (1966)). The Bessel function, J_n, is defined using integral notation,

$$J_n(kr) = \frac{1}{\pi}\int_0^{\pi} \cos(n\tau - (kr)\sin\tau)d\tau \tag{A.1}$$

where unique solutions, normalized between 1 and 0, exist for all kr for discrete values of n. Where n is the mode number of the function and kr is a dimensionless length. Any function can be expressed as an infinite linear combination of Bessel functions, where $f(x) = \sum_{n=0}^{\infty} c_n J_n(x)$ and c_n are problem-specific coefficients, commonly determined by initial or boundary conditions. While summing over an infinite number of modes is prescribed, a finite number is often sufficient ($n > kr + 5$). The output of Equation A.1 is a periodic function that resembles a sine or cosine that decays proportionally to $1/\sqrt{kr}$.

The spherical Bessel function, j_n, in Figure A.1, is a solution to Helmholtz differential equation (Equation 2.7a and 2.7b) in spherical coordinates. The spherical Bessel functions are related to the Bessel function of the first kind, J_n, by $j_n(kr) = \sqrt{\frac{\pi}{2kr}}J_{n+1/2}(kr)$, where n specifies the vibrational mode (*Boas* (1966)). The spherical Hankel function, h_n, in Figure A.2, is a combination of the spherical Bessel function with a spherical Neumann function, y_n, in the complex plane, such that $h_n = j_n + iy_n$ (*Boas* (1966)). The Bessel and Neumann function are linearly independent solutions to the Helmholtz equation, where the

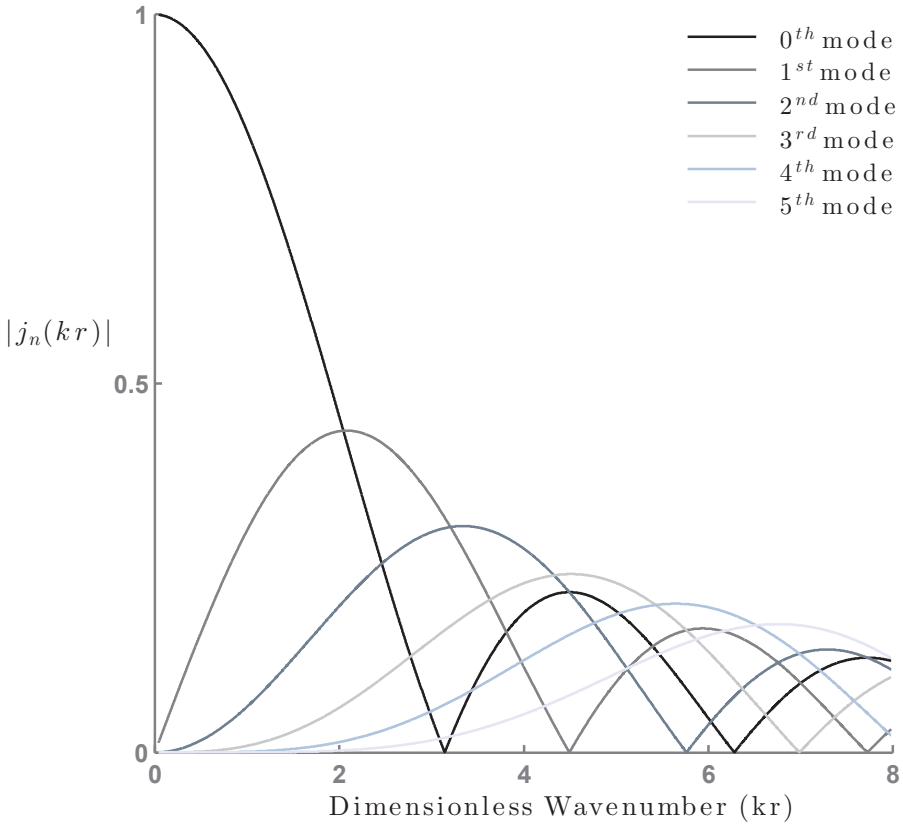

Figure A.1: First five modes of the spherical Bessel function with respect to the dimensionless wavenumber (kr).

Bessel function is bounded at the origin and the Neumann function diverges at the origin (*Boas* (1966)). Correspondingly, the spherical Hankel functions are related to the Hankel functions of the first kind, H_n, by $h_n(kr) = \sqrt{\frac{\pi}{2kr}} H_{n+1/2}(kr)$ (*Boas* (1966)).

The derivatives of the spherical Bessel and Hankel functions are represented in terms of recursion relationships (*Morse* (1948)),

$$j_n'(kr) = \frac{\partial j_n(kr)}{\partial(kr)} = \frac{n}{(kr)} j_n(kr) - j_{n+1}(kr) \tag{A.2}$$

$$j_n''(kr) = \frac{\partial^2 j_n(kr)}{\partial(kr)^2} = \frac{((n-1)n - (kr)^2) j_n(kr) + 2kr j_{n+1}(kr)}{(kr)^2}. \tag{A.3}$$

The Legendre polynomial, $P_n(cos\theta)$, describes the angular dependence of scatter (*Boas* (1966)). Figure A.3 show the angular dependence of the Legendre polynomial. Note that

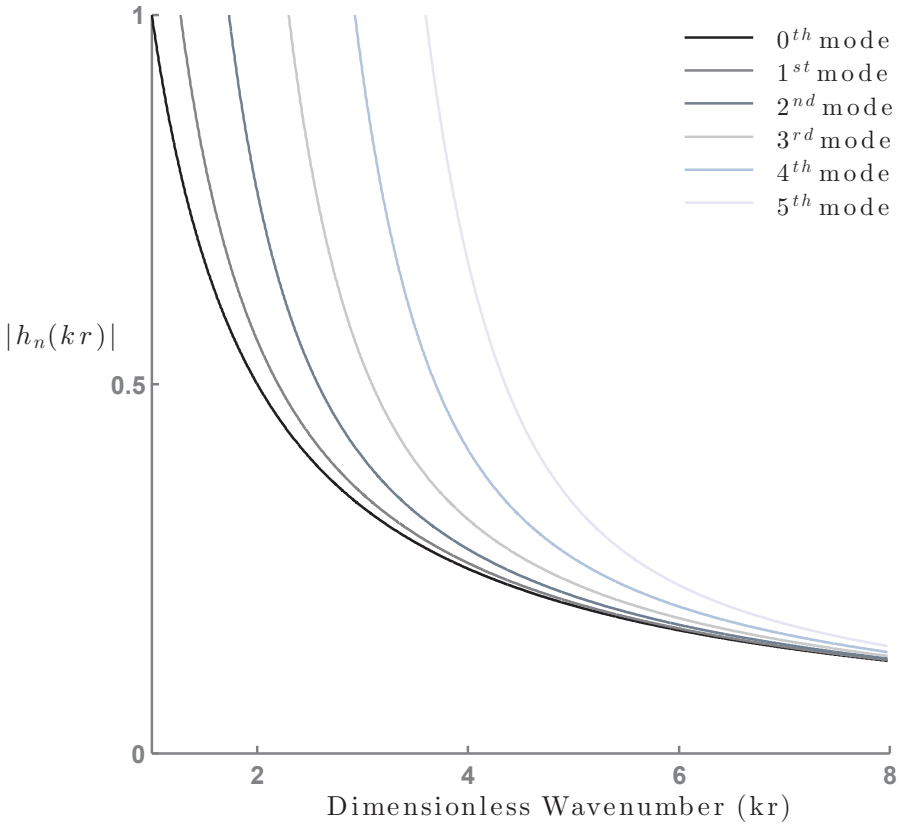

Figure A.2: First five modes of the spherical Hankel function with respect to the dimensionless wavenumber (kr).

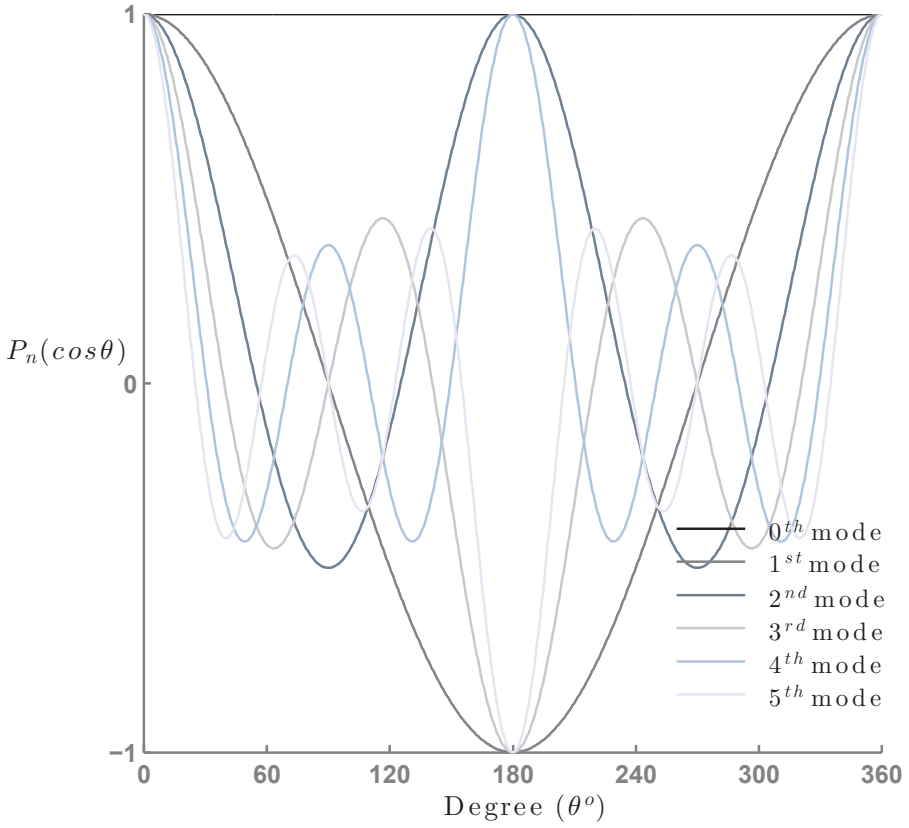

Figure A.3: First five modes of the Legendre Polynomial with respect to the angle between the incident and observed wave, where $0°$ is the direction of incidence and $180°$ refers to backscattering

for the case of backscattering ($\theta = 180^{\circ}$), the Legendre polynomial indicates that even and odd modes are in quadrature (separated by a 90° phase), where $P_n(cos(180^{\circ})) = (-1)^n$.

APPENDIX B

SCATTERING COEFFICIENTS

B.1 Case I: Solid Sphere in a Fluid Medium

The coefficients from *Gaunard and Uberall* (1983) in Equation 2.23 and 2.24 were used to predict the amplitude of a compressional wave scattered from a solid sphere in a fluid medium.

$$
\begin{aligned}
d_n^{(10)}(\omega) &= -(\frac{\rho_1}{\rho_2})(k_{s2}r)^2 j_n(k_{l1}r) \\
d_n^{(20)}(\omega) &= (k_{l1}r) j_n'(k_{l1}r) \\
d_n^{(30)}(\omega) &= 0 \\
d_n^{(11)}(\omega) &= (\frac{\rho_1}{\rho_2})((k_{s2}r)^2) h_n(k_{l1}r) \\
d_n^{(12)}(\omega) &= (2n(n+1) - (k_{s2}r)^2) j(k_{l2}r) - 4k_{l2}r j'(k_{l2}r) \\
d_n^{(13)}(\omega) &= (2n(n+1)(k_{s2}r j_n'(k_{s2}r) - j_n(k_{s2}r)) \\
d_n^{(21)}(\omega) &= -k_{l1}r(h_n'(k_{l1}r)) \\
d_n^{(22)}(\omega) &= k_{l2}r j_n'(k_{l2}r) \\
d_n^{(23)}(\omega) &= n(n+1) j_n(k_{s2}r) \\
d_n^{(31)}(\omega) &= 0 \\
d_n^{(32)}(\omega) &= 2j_n(k_{l2}r) - k_{l2}r j_n'(k_{l2}r) \\
d_n^{(33)}(\omega) &= 2k_{s2}r j_n'(k_{s2}r) + ((k_{s2}r)^2 - 2n(n+1) + 2) j_n(k_{s2}r)
\end{aligned}
\tag{B.1}
$$

B.2 Case II: Solid Sphere in a Solid Medium

The coefficients from *Flax and Uberall* (1980) in Equation 2.26 and 2.27 were used to predict the amplitude of a compressional wave scattered from a solid sphere in a solid medium.

$$
\begin{aligned}
b_n^{(11)}(\omega) &= -(\frac{\rho_1}{\rho_2})((\lambda_1 h_n(k_{l1}r) - \frac{2\mu_1 h_n''(k_{l1}r))}{\lambda_1 + 2\mu_1}) \\
b_n^{(12)}(\omega) &= 2(\frac{\rho_1}{\rho_2})(n(n+1))(k_{s1}r)^{-2}((k_{s1}rh_n'(k_{s1}r)) - h_n(k_{s1}r)) \\
b_n^{(13)}(\omega) &= \lambda_2 j_n(k_{l2}r) - \frac{2\mu_2 j_n''(k_{l2}r)}{\lambda_2 + 2\mu_2} \\
b_n^{(14)}(\omega) &= -2n(n+1)(k_{s2}r)^{-2}(k_{s2}rj_n'(k_{s2}r) - j_n(k_{s2}r)) \\
b_n^{(10)}(\omega) &= (\frac{\rho_1}{\rho_2})((\lambda_1 j_n(k_{l1}r) - \frac{2\mu_1 j_n''(k_{l1}r))}{\lambda_1 + 2\mu_1)} \\
b_n^{(21)}(\omega) &= -h_n(k_{l1}r) \\
b_n^{(22)}(\omega) &= -(h_n(k_{s1}r) + (k_{s1}rh_n'(k_{s1}r)) \\
b_n^{(23)}(\omega) &= j_n(k_{l2}r) \\
b_n^{(24)}(\omega) &= j_n(k_{s2}r) + (k_{s2}rj_n'(k_{s2}r)) \\
b_n^{(20)}(\omega) &= j_n(k_{l1}r) \\
b_n^{(31)}(\omega) &= -2((k_{l1}rh_n'(k_{l1}r)) - h_n(k_{l1}r)); \\
b_n^{(32)}(\omega) &= ((k_{s1}r)^2 h_n''(k_{s1}r)) + ((n+2)(n-1)h_n(k_{s1}r)) \\
b_n^{(33)}(\omega) &= (\frac{2\mu_2}{\mu_1})(k_{l2}rj_n'(k_{l2}r) - j_n(k_{l2}r)) \\
b_n^{(34)}(\omega) &= (\frac{2\mu_2}{\mu_1})(((k_{s2}r)^2 j_n''(k_{s2}r)) + ((n+2)(n-1)h_n(k_{s2}r))) \\
b_n^{(30)}(\omega) &= 2(k_{l1}rj_n'(k_{l1}r) - j_n(k_{l1}r)) \\
b_n^{(41)}(\omega) &= -k_{l1}rh_n'(k_{l1}r) \\
b_n^{(42)}(\omega) &= -(n(n+1))h_n(k_{s1}r) \\
b_n^{(43)}(\omega) &= k_{l2}rj_n'(k_{l2}r) \\
b_n^{(44)}(\omega) &= (n(n+1))j_n(k_{s2}r) \\
b_n^{(40)}(\omega) &= k_{l1}rj_n'(k_{l1}r)
\end{aligned}
\tag{B.2}
$$

B.3 Case III: Fluid Sphere in a Solid Medium

The coefficients from *Gaunard and Uberall* (1978) in Equation 2.29 and 2.30 were used to predict the amplitude of a compressional wave scattered from a fluid sphere in a solid medium.

$$
\begin{aligned}
c_n^{(11)}(\omega) &= k_{l1} r j_n'(k_{l1} r) \\
c_n^{(12)}(\omega) &= (n(n+1)) h_n(k_{s1} r) \\
c_n^{(13)}(\omega) &= -k_{l2} r j_n'(k_{l2} r) \\
c_n^{(21)}(\omega) &= (2n(n+1) - (k_{s1} r)^2) h_n(k_{l1} r) - 4 k_{l1} r h_n'(k_{l1} r) \\
c_n^{(22)}(\omega) &= (2n(n+1) k_{s1} r h_n'(k_{s1} r)) - h_n(k_{s1} r) \\
c_n^{(23)}(\omega) &= \frac{\rho_1}{\rho_2} (k_{s1} r)^2 j_n(k_{l2} r) \\
c_n^{(31)}(\omega) &= k_{l1} r h_n'(k_{l1} r) - h_n(k_{l1} r) \\
c_n^{(32)}(\omega) &= (n(n+1) - 1 - \frac{k_{s1} r^2}{2}) h_n(k_{s1} r) - k_{s1} r h_n'(k_{s1} r) \\
c_n^{(33)}(\omega) &= 0; \\
c_n^{(10)}(\omega) &= -k_{l1} r j_n'(k_{l1} r) \\
c_n^{(20)}(\omega) &= ((k_{s1} r)^2 - 2n(n+1)) j_n(k_{l1} r) + 4 k_{l1} r j_n'(k_{l1} r) \\
c_n^{(30)}(\omega) &= j_n(k_{l1} r) + k_{l1} r j_n'(k_{l1} r)
\end{aligned}
\tag{B.3}
$$

APPENDIX C

AQUATRON TANK WATER PROPERTIES

Temperature and salinity measurements in the Tower Tank are shown in Figure C.1. These measurements were made on August 6th, 2014, by Adam Comeau using a Sea-Bird Electronics Glider Payload CTD. The temperature in the tank fluctuates between 14°C and 18°C, while the salinity remains constant around 31.5 PSU. CTD measurements are not available for other dates that experiments were conducted, however, an average surface temperature of 24°C was measured on October 22nd, 2012.

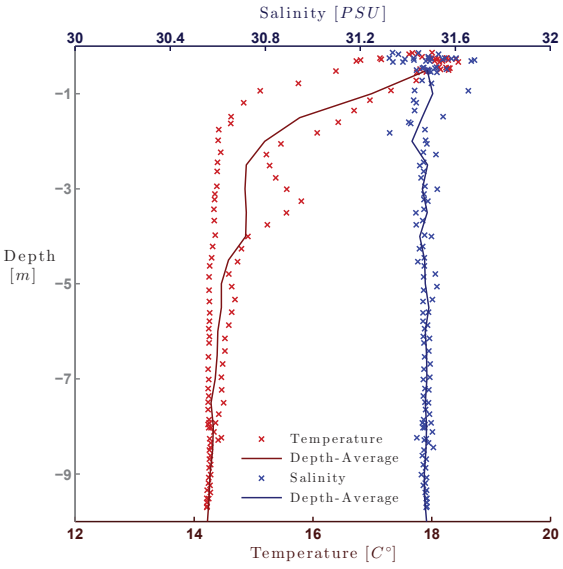

Figure C.1: Temperature and salinity profiles collected in the Aquatron Tower Tank. The crosses represent observations collected with a CTD by Adam Coumeau on August 6th, 2014. The solid lines are represent averages over half a meter depth.

Water density and soundspeed are calculated from temperature and salinity measurements, using the method of *Millero et al.* (2008) and *Mackenzie* (1981), respectively, and presented in Figure C.2.

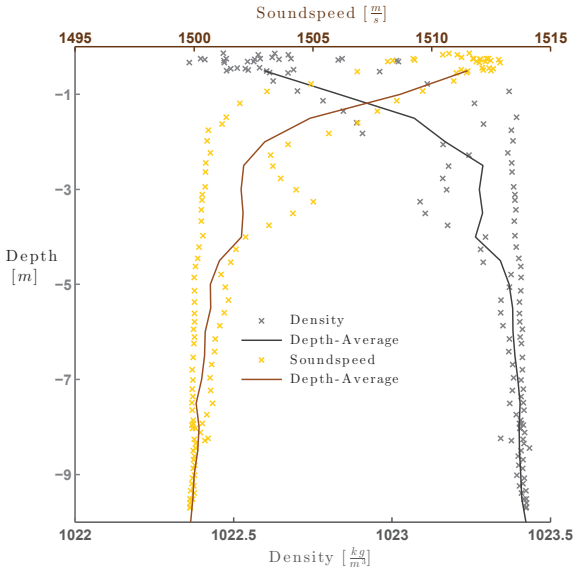

Figure C.2: Density and soundpseed profiles are calculated from temperature and salinity measurements from Figure C.1. The crosses represent discrete samples and the solid lines are represent averages over half a meter depth.

The attenuation of sound in water is due to absorption of acoustic energy into heat and is a function of water temperature, depth in the tank and frequency of the acoustic pulse. The frequency dependent attenuation coefficient, $\alpha(\omega)$, is used to account for attenuation of the acoustic pulse as it propagates down the beam. *Ainslie and McColm* (1998) approximate the attenuation coefficient as,

$$\alpha(\omega) = 4.9 \times 10^{-7}(\omega^2)\, e^{-T/2+R/17} \tag{C.1}$$

where T is the water temperature and R is the depth in the tank (*Ainslie and McColm* (1998)). The attenuation in the Tower Tank, in Figure C.3, ranges between 2-6.5 dB/km, where higher frequencies experience more attenuation.

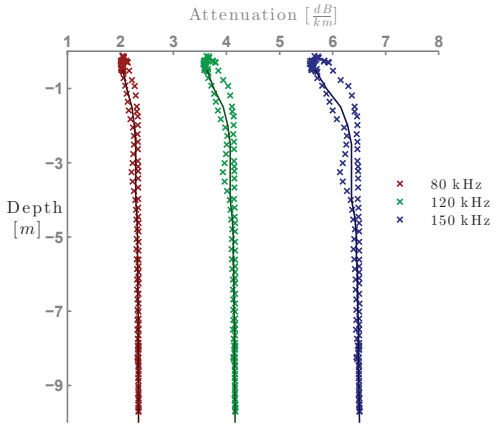

Figure C.3: Frequency dependent sound attenuation in the Aquatron Tower Tank is calculated from CTD measurements, in Figure C.1. The attenuation coefficient is calculated using the *Ainslie and McColm* (1998) equation.

A sample of the average background noise level in tank is provided in Figure C.4 calculated from a portion of the pulse compressed signal without scattering from targets. The noise level in the tank is higher in the low frequency range of the echosounder system, between 90-110 kHz.

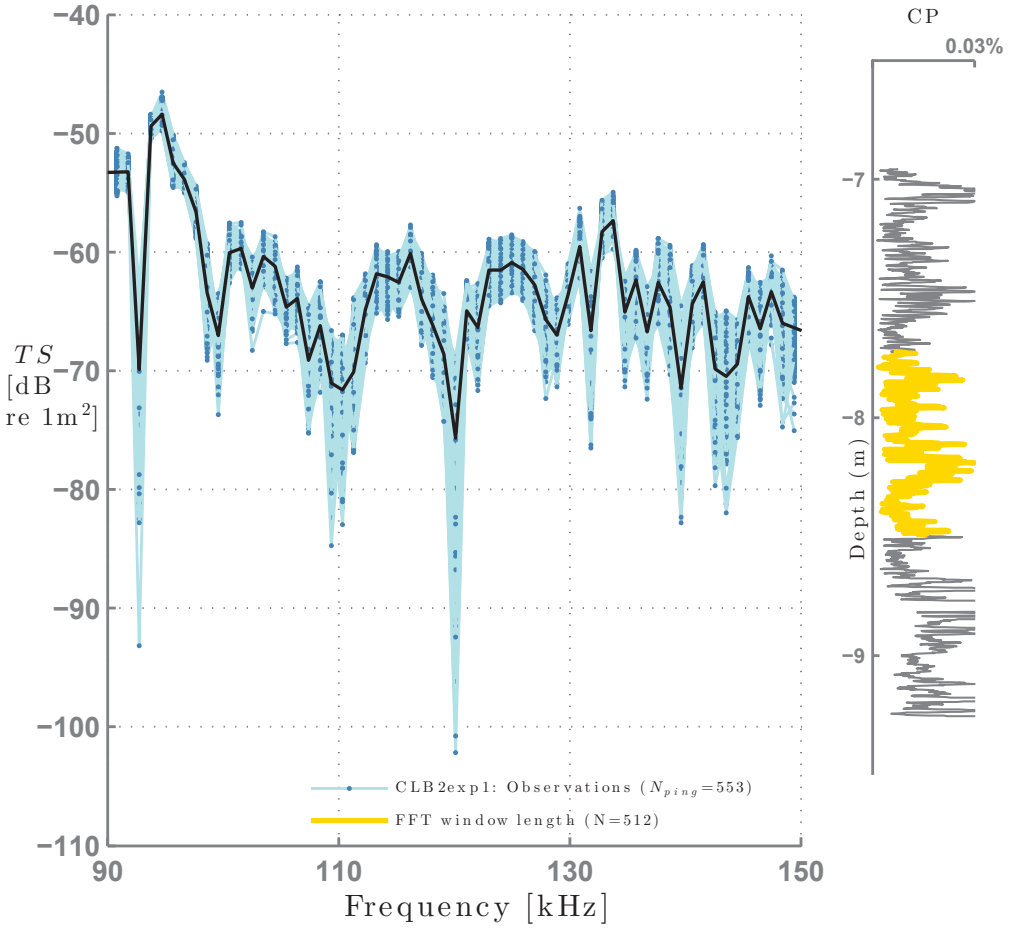

Figure C.4: Mean background noise level in the Aquaton Tower Tank on August 7th, 2014 [CLB1exp1] (solid black line), calculated from an ensemble of pings (shown in blue). Right panel: The CP envelope shows the background noise level relative to the transmit pulse, with the size of the FFT window shown in gold.

BIBLIOGRAPHY

Abeele, K. V. D., R. Briers, and O. Leroy, Inhomogeneous plane-wave scattering and mode stimulation on periodic rough surfaces, *Journal of the Acoustical Society of America*, *99(5)*, 2883–2897, 1996.

Abramowitz, M., and I. Stegun, *Handbook of mathematical functions with formulas, graphs and mathematical tables*, 1st ed., National Bureau of Standards, Applied Mathematics, 1964.

Ainslie, M. A., and J. G. McColm, A simplified formula for viscous and chemical absorption in sea water, *Journal of the Acoustical Society of America*, *103(3)*, 1671–1672, 1998.

Aki, K., and P. G. Richards, *Quantitative Seismology*, University Science Books, 1980.

Anderson, D., Use of long period surface waves for determination of elastic and petrological properties of ice masses, in *Ice and Snow: Properties, Processes and Applications*, MIT Press, 1963.

Anderson, D. L., Elastic wave propagation in layered anisotropic media, *Journal of Geophysical Research*, *66(9)*, 2953–2963, 1961.

Anderson, V. C., Sound scattering from a fluid sphere, *Journal of Acoustical Society of America*, *22 (4)*, 426–431, 1950.

Anstee, S., Use of spherical objects as calibrated minehunting sonar targets, in *Technical Report DSTO-TN-0425*, Defense Science and Technology, Maritime Operations Division, 2002.

Bassett, C., A. C. Lavery, T. Maksym, and J. Wilkinson, Laboratory measurements of high-frequency, acoustic broadband backscattering from sea ice and crude oil, *Journal of the Acoustical Society of America*, *137(1)*, EL32–EL38, 2015.

Bin, L., Z. Zhe-Min, and C. Jian-Chung, Propagation of acoustic wave in viscoelastic medium permeated with air bubbles, *Chinese Physics*, *31 (3)*, 412–421, 2006.

Biot, M., Mechanics of deformation and acoustic propagation in porous media, *Journal of Applied Physics*, *33(4)*, 1482–1489, 1962.

Black, C., *Geometry and Composition of Ice Banks in a Macrotidal Channel*, M.Sc Thesis, Dalhousie University, 2013.

Boas, M. L., *Mathematical Methods in the Physical Sciences*, 3rd ed., Wiley, 1966.

Brekhovskikh, L. M., and Y. Lysanov, *Fundamentals of Ocean Acoustics*, 1st ed., Springer, 1982.

Brown, J., and D. Brown, Reverberation under arctic sea ice, *Journal of the Acoustical Society of America*, *40(2)*, 399–404, 1966.

Chamuel, J. R., Arctic acoustics ultrasonic modeling studies, in *Technical Report JRC-10-90*, Sonoquest Advanced Ultrasonics Research, 1990.

Chan, O., F. Chen, C. Chow, and I. Ward, The elastic constants of extruded polypropylene and polyethylene terephthalate, *Journal of Applied Physics*, *11*, 617–629, 1978.

Chivers, R. C., and L. W. Anson, Calculations of the backscattering (and radiation force) functions of spherical targets for use in ultrasonic beam assessment, *Journal of the Acoustical Society of America*, *20*, 25–34, 1982.

Chu, D., and T. K. Stanton, Application of pulse compression techniques to broadband acoustic scattering by live individual zooplankton, *Journal of the Acoustical Society of America*, *104(1)*, 39–55, 1998.

Crary, A., Seismic studies on fletcher's ice island, *Journal of Geophysical Research*, *35(2)*, 293–300, 1954.

Desplanque, C., and D. J. Mossman, A review of ice and tide observations in the Bay of Fundy, *Journal of Atlantic Geology*, *34*, 195–209, 1998.

Dragonette, L. R., S. Numrich, and L. J. Frank, Calibration technique for acoustic scattering measurements, *Journal of the Acoustical Society of America*, *69(4)*, 1186–1189, 1981.

Dugan, J., W. DiMarco, W. Martin, and W. Tucket, Low frequency surface motion of arctic pack ice, *Journal of Geophysical Research*, *97(C4)*, 5381–5388, 1992.

Dyer, I., Fracture of sea ice, *Journal of the Acoustical Society of America*, *94*, 1759, 1993.

Eicken, H., R. Gradinger, A. Gaylord, A. Mahoney, I.Rigor, and H.Melling, Sediment transport by sea ice in the chukchi and beaufort seas: Increasing importance due to changing ice conditions?, *Deep Sea Research II*, *52(24)*, 3281–3302, 2005.

Etter, P., *Underwater Acoustic Modeling and Simulation*, 4th ed., CRC Press, 2013.

Ewing, M., A. Crary, and A. Thorne, Propagation of elastic waves in ice. part i, *Journal of the Applied Physics*, *5*, 165–168, 1934.

Faran, J. J., Sound scattering by solid cylinders and spheres, *Journal of the Acoustical Society of America*, *27 (9)*, 405–418, 1951.

Farmer, D. M., and Y. Xie, Acoustic and seismic measurement of ice processes, *Journal of the Acoustical Society of America*, *97*, 3335, 1995.

Farmer, D. M., G. B. Deane, and S. Vagle, The influence of bubble clouds on acoustic propagation in the surf zone, *IEEE Journal of Oceanic Engineering*, *26(1)*, 113–124, 2001.

Flax, L., and H. Uberall, Resonant scattering of elastic waves from spherical solid inclusions, *Journal of the Acoustical Society of America*, *67 (5)*, 1432–1442, 1980.

Foote, K. G., Importance of the swimbladder in acoustic scattering by fish: A comparision of gadoid and mackerel target strengths, *Journal of the Acoustical Society of America*, *67(1)*, 2084, 1980.

Fricke, J. R., Acoustic scattering from elemental arctic ice features: Numerial modeling results, *Journal of the Acoustical Society of America*, *93(4)*, 1784–1796, 1993.

Frost, G. L., Inventing schemes and strategies: The making and selling of the fessenden oscillator, *Technology and Culture*, *42(3)*, 462–488, 2001.

Garrison, G., R. Francois, and T. Wen, Acoustic reflections from arctic ice at 15-300 khz, *Journal of the Acoustical Society of America*, *90(2)*, 973–984, 1991.

Gaunard, G., and H. Uberall, Theory of resonant scattering from spherical cavitites in elastic and viscoelastic media, *Journal of the Acoustical Society of America*, *63 (6)*, 1699–1712, 1978.

Gaunard, G., and H. Uberall, Rst analysis of monostatic and bistatic acoustic echoes from an elastic sphere, *Journal of the Acoustical Society of America*, *73 (1)*, 1–12, 1983.

Gaunard, G., and M. Werby, Resonance response of submerged, acoustically excited thick and thin shells, *Journal of the Acoustical Society of America*, *77 (6)*, 2081–2093, 1985.

Gaunard, G., and M. Werby, Lamb and creeping waves around submerged spherical shells resonantly excited by sound scattering, *Journal of the Acoustical Society of America*, *82 (6)*, 2021–2033, 1987.

Gaunard, G., and M. Werby, Sound scattering by resonantly excited, fluid-loaded, elastic spherical shells, *Journal of the Acoustical Society of America*, *90 (5)*, 2536 –2550, 1991.

Gerlich, D., and G. Kennedy, The elastic modulii and their pressure derivatives for tungsten carbide with different amounts of cobalt binder, *Journal of Applied Physics*, *50(5)*, 3331–3333, 1979.

Goodman, J., *Introduction to Fourier Optics*, 2nd ed., McGraw-Hill, 1996.

Graff, K. F., *Wave motion in elastic solids*, Courier Dover Publications, 1975.

Greenhill, A., Wave motion in hydrodynamics, *American Journal of Mathematics*, *9(1)*, 62–96, 1886.

Hampton, L. D., and C. M. McKinney, Experimental study of the scattering of acoustic energy from solid metal spheres in water, *Journal of the Acoustical Society of America*, *33 (5)*, 664–673, 1961.

Hickling, R., Analysis of echoes from a solid elastic sphere in water, *Journal of the Acoustical Society of America*, *34 (10)*, 1582–1592, 1962.

Hind, H. Y., The ice phenomena and the tides of the Bay of Fundy, considered in connection with the construction of the baie verte canal, *The Canadian Monthly and National Review*, *8(3)*, 189–203, 1875.

Hunkins, K., Seismic studies of sea ice, *Journal of Geophysical Research*, *65(10)*, 3459–3472, 1960.

Jezek, K. C., Acoustic waves incident on a seawater/sea ice interface, in *Technical Report AD-A213 085*, US Army Corps of Engineers, 1985.

Jezek, K. C., T. K. Stanton, A. J. Gow, and M. A. Lange, Influence of environmental conditions on acoustical properties of sea ice, *Journal of the Acoustical Society of America*, *88*, 1903, 1990.

Karsten, R., A. Swan, and J. Culina, Assessment of arrays of in-stream tidal turbines in the Bay of Fundy, *Phil. Trans. R. Soc. A*, *371*, 2012.

Kinsler, L. E., A. R. Frey, A. B. Coppens, and J. V. Sanders, *Fundamentals of Acoustics*, 4th ed., John Wiley and Sons, Inc, 1972.

Klauder, J. R., A. C. Price, S. Darlington, and W. J. Albersheim, The theory and design of chirp radars, *Bell System Technical Journal*, *39*, 745–808, 1960.

Kutschale, H., Arctic hydroacoustics, *Arctic*, *22(3)*, 246–264, 1969.

Laible, H. A., *Wave scattering from cylindrical fluid inclusions in an elastic medium and determination of effective medium properties*, M.Sc Thesis, Massachusetts Institute of Technology, 1995.

Laible, H. A., and S. D. Rajan, Temporal evolution of under ice reflectivity, *Journal of the Acoustical Society of America*, *99(2)*, 851–865, 1996.

Langhorne, P., and T. Haskell, Acoustic emission during fatigue experiments on first year sea ice, *Cold Regions Science and Technology*, *24*, 237–250, 1996.

Langleben, M., Reflection of sound at the water-sea ice interface, *Journal of Geophysical Research*, *75(27)*, 5243–5246, 1970.

Lavery, A. C., P. H. Wiebe, T. K. Stanton, G. L. Lawson, M. C. Benfield, and N. Copley, Determining dominant scatterers of sound in mixed zooplankton populations, *Journal of the Acoustical Society of America*, *122*, 3304, 2007.

Love, R. H., Resonant acoustic scattering by swimbladder-bearing fish, *Journal of the Acoustical Society of America*, *64(1)*, 571, 1978.

Mackenzie, K., Nine-term equation for the sound speed in the oceans, *Journal of the Acoustical Society of America*, *70(3)*, 807–812, 1981.

Maksimov, A. O., Acoustic manifestation of bubbles frozen in an ice sheet, *Acoustical Physics*, *57(3)*, 391–400, 2011.

Mandal, B., Reflection and transmission properties of elastic waves on a plane interface for general anisotropic media, *Journal of the Acoustical Society of America*, *90(2)*, 1106–1118, 1991.

Mayer, W. G., Determination of transverse wave velocity in transition layer of sea ice from reflection of water borne sound, *Journal of Geophysical Research*, *79(6)*, 5243–5246, 1974.

Mayer, W. G., M. Behravesh, and T. J.Plona, Determination of sonic velocities from reflectivity losses at sea ice/water boundaries, *Journal of the Acoustical Society of America*, *57(1)*, 39–46, 1975.

McCammon, D. F., and S. T. McDaniel, The influence of the physical properties of ice on reflectivity, *Journal of the Acoustical Society of America*, *77*, 449, 1985.

McPhee, M. G., J. H. Morison, and F. Nilsen, Revisiting heat and salt exchange at the ice-ocean interface: Ocean flux and modeling considerations, *Journal of Geophysical Research*, *113 (1)*, 6014–6025, 2008.

Medwin, H., and C. S. Clay, *Fundamentals of Acoustical Oceanography*, Academic Press, 1998.

Mellen, R., and H. Marsh, Underwater sound in the arctic ocean, in *Technical Report AD718140*, US Navy Underwater Sound Laboratory, 1965.

Miller, B. E., and H. Schmidt, Observation and inversion of seismo-acoustic waves in a complex arctic ice environment, *Journal of the Acoustical Society of America*, *89(4)*, 1668–1685, 1991.

Millero, F. J., R. Feistel, D. G. Wright, and T. J. McDougall, The composition of standard seawater and the definition of the reference-composition salinity scale, *Deep Sea Research I*, *55(1)*, 50–72, 2008.

Milne, A., Underwater backscattering strengths of arctic pack ice, *Journal of the Acoustical Society of America*, *36*, 1551–1556, 1964.

Milne, A., Thermal tension cracking in sea ice: A source of underwater noise, *Journal of Geophysical Research*, *77*, 2177–2192, 1972.

Morse, P. M., *Vibration and Sound*, 2nd ed., McGraw-Hill, 1948.

Morse, P. M., and K. U. Ingard, *Theoretical Acoustics*, 1st ed., McGraw-Hill, 1968.

Mourad, P. D., and K. L. Williams, Nearnormal incidence scattering from rough, finite surfaces: Kirchhoff theory and data comparison for arctic sea ice, *Journal of the Acoustical Society of America*, *94(2)*, 1584, 1993.

Mow, C. C., and T. H. Pao, The diffraction of elastic waves and dynamics stress concentrations, in *Technical Report R-482-PR*, United States Air Force: Project Rand, 1971.

Notz, D., J. S. Wettlaufer, and M. Worster, A non-destructive method for measuring the salinity and solid fraction of growing sea ice in situ, *Journal of Glaciology*, *51(172)*, 159–166, 2005.

Nurnberg, D., I. Wollenburg, D. Dethleff, H.Eicken, H.Kassens, T.Letzig, E.Reimnitz, and J.Thiede, Sediments in arctic sea ice: Implications for entrainment, transport and release, *Marine Geology*, *119*, 185–214, 1994.

Oliver, J., A. Crary, and R. Cotell, Elastic waves in arctic pack ice, *Journal of Geophysical Research*, *35(2)*, 6643–6648, 1954.

Press, F., and M. Ewing, Propagation of elastic waves in a floating ice sheet, *Journal of Geophysical Research*, *32(5)*, 673–678, 1951.

Press, F., M. Ewing, A. Cray, S. Katz, and J. Oliver, Air-coupled flexural waves on floating ice, in *Technical Report AD638146*, Air Force Cambridge Research Laboratories, 1950.

Rajan, S. D., G. V. Fisk, J. A. Doutt, and C. J. Sellers, Determination of compressional wave and shear wave speed profiles in sea ice by crosshole tomography-theory and experiment, *Journal of the Acoustical Society of America*, *93(2)*, 721–738, 1992.

Reeder, D. B., *Acoustic Scattering by Axisymmetric Finite length Bodies with Application to Fish: Measurement and Modeling*, Ph.D Disseration, MIT/WHOI, 2002.

Roberts, P. D., and J. S. Jaffe, Classification of live, untethered zooplankton from observations of multiple-angle acoustic scatter, *Journal of the Acoustical Society of America*, *124(2)*, 796–802, 2008.

Robins, A. J., Plane-wave reflection from a solid layer with nonuniform density, sound-speed and shear speed, *Journal of the Acoustical Society of America*, *103(3)*, 1337–1345, 1998.

Ross, T., J. E. Keister, and A. Lara-Lopez, On the use of high-frequency broadband sonar to classify biological scattering layers from a cabled observatory in saanich inlet, british columbia, *Methods in Oceanography*, *5*, 19–38, 2013.

Rothlisberger, H., Seismic exploration in cold regions, in *Technical Report AD0752111*, USA Cold Regions Research and Engineering Laboratory, 1972.

Sammelmann, G. S., Biot-stoll model of the high-frequency reflection coefficient of sea ice, *Journal of the Acoustical Society of America*, *94(1)*, 371–385, 1993.

Sanders, R. E., Marine ice and other issues during harvest of tidal electricity from nova scotia's minas passage in 2011, *Journal of Ocean Technology*, *6(1)*, 33–56, 2011.

Sanders, R. E., and E. Baddour, Documenting Ice in the Bay of Fundy, Canada, in *Contractor Report CR-2006-01*, National Research Council of Canada, Institute for Ocean Technology, 2006.

Sanders, R. E., and E. Baddour, Engineering Issues in the Harvest of Tidal Electricity in the Bay of Fundy, Canada, in *Marine Renewable Energy*, Engineering Committee on Oceanic Resources Symposium 2008, 2008.

Sanderson, B. G., and A. M. Redden, Perspective on the risk that sediment-laden ice poses to in-stream tidal turbines in Minas Passage, Bay of Fundy, *International Journal of Marine Energy*, *10*, 1710–1712, 2015.

Sanderson, B. G., A. M. Redden, and J. E. Broome, Sediment-laden ice measurements and observations, and implications for potential interactions of ice and large woody debris with tidal turbines in minas passage, in *Publication No. 109 of the Acadia Centre for Estuarine Research*, 2012.

Sessarego, J. P., J. Sageloli, R. Guillermin, and H. Uberall, Scattering by an elastic sphere embedded in an elastic isotropic medium, *Journal of the Acoustical Society of America*, *104 (5)*, 2836–2844, 1998.

Sharma, M., Wave propagation in a general anisotropic poroelastic medium: Biots theories and homogenisation theory, *Journal of Earth System Science*, *116(4)*, 357–367, 2007.

Simmonds, J., and D. MacLennan, *Fisheries Acoustics*, 2nd ed., Blackwell Science, 2005.

Skyllingstad, E. D., C. A. Paulson, W. S. Pegau, M. G. McPhee, and T. Stanton, Effects of keels on ice bottom turbulence exchange, *Journal of Geophysical Research*, *108(12)*, 3372–3388, 2003.

Squire, V., J. Dugen, P. Wadhams, P.Rottier, and A. Liu, Ocean waves and sea ice, *Annual Review of Fluid Mechanics*, *27*, 115–168, 1995.

Stanton, T., K. Jezek, and A. Gow, Acoustical reflection and scattering from the underside of laboratory grown sea ice: Measurements and predictions, *Journal of the Acoustical Society of America*, *80*, 1486, 1986.

Stanton, T. K., and D. Chu, Calibration of broadband active acoustic systems using a single standard spherical target, *Journal of the Acoustical Society of America*, *124*, 128–136, 2008.

Stanton, T. K., D. Chu, and P. Wiebe, Sound scattering by several zooplankton groups ii: scattering models, *Journal of the Acoustical Society of America*, *103*, 236–253, 1998.

Stanton, T. K., D. Chu, and P. H. Wiebe, Ray solutions to sound scattering by complex bodies: Application to zooplankton, in *New Perspectives on Problems in Classical and Quantum Physics. Part II.*, Gordon and Breach Science Publishers, Amsterdam, 2000.

Stein, P. J., Interpretation of a few ice event transients, *Journal of the Acoustical Society of America*, *83(2)*, 617–622, 1988.

Stein, P. J., S. E. Euerle, and J. C. Parinella, Inversion of pack ice elastic wave data to obtain ice physical properties, *Journal of Geophysical Research*, *103(C10)*, 6643–6648, 1998.

Timco, G., and W. Weeks, A review of the engineering properties of sea ice, *Cold Regions Science and Technology*, *60*, 107–129, 2010.

Trowse, G., *On the Melt Rate of Submerged Sediment Laden Ice*, M.Sc Thesis, Dalhousie University, 2013.

Wadley, H., C. Scruby, and G. Shrimpton, Quantitative acoustic emission source characterization during low temperature cleavage and intergranular fracture, *Acta Metallurgica*, *29*, 399–414, 1981.

Weber, J., Ice floes in collision, *Journal of Glaciology*, *20(82)*, 135–139, 1978.

Weeks, W., and A. Assur, Mechanical properties of sea ice, in *Technical Report AD662716*, Cold Regions Research and Engineering Laboratory, 1967.

Wen, T., G. Garrison, R. Francois, R. Stein, and W. Felton, Sound speed, reflectivity, and absorption measurements in arctic ice in 1988, 1991.

Weng, X., and C. Yew, The leaky rayleigh wave and scholte wave at the interface between water and porous sea ice, *Journal of the Acoustical Society of America*, *87(6)*, 2481–2488, 1990.

Williams, K., and R. Francois, Sea ice elastic moduli: Determination of biot parameters using infield velocity measurements, *Journal of the Acoustical Society of America*, *91*, 2627, 1992.

Williams, R., and E. Robinson, Flexural waves in the ross ice shelf, *Journal of Geophysical Research*, *86(C7)*, 6643–6648, 1981.

Winebrenner, D. P., Acoustic backscattering from sea ice at 10-100 khz, in *Technical Report APL-UW TR 9017*, Applied Physics Laboratory, University of Washington, 1991.

Wong, G., and T. Embleton, The variation of the speed of sound in air with humidity and temperature, *Journal of the Acoustical Society of America*, *77(5)*, 1710–1712, 1985.

Xie, Y., and D. M. Farmer, Seismic-acoustic sensing of sea ice wave mechanical properties, *Journal of Geophysical Research*, *99(C4)*, 7771–7786, 1994.

Yew, C., and X. Weng, A study of reflection and refraction of waves at the interface of water and porous sea ice, *Journal of the Acoustical Society of America*, *82(1)*, 342–353, 1987.

Ying, C., and R. Truell, Scattering of a plane longitudinal wave by a spherical obstable in a isotropically elastic solid, *Journal of Applied Physics*, *27 (9)*, 1086–1097, 1956.

Zakarauskas, P., Detection and localization of nondeterministic transients in time series and application to ice-cracking sound, *Journal of Digital Signal Processing*, *3*, 36–45, 1993.